1-1-2013

Ultrawideband (UWB) and Reconfigurable Antennas - New Concepts For Conformal Load Bearing Antenna Structures (CLAS)

Nicholas Bishop
University of South Carolina

ULTRAWIDEBAND (UWB) AND RECONFIGURABLE ANTENNAS – NEW CONCEPTS FOR CONFORMAL LOAD BEARING ANTENNA STRUCTURES (CLAS)

by

Nicholas Bishop

Bachelor of Engineering
University of South Carolina, 2011

Submitted in Partial Fulfillment of the Requirements

For the Degree of Master of Science in the

Department of Electrical Engineering

College of Engineering and Computing

University of South Carolina

2013

Accepted by:

Mohammod Ali, Major Professor

Grigory Simin, Committee Member

Lacy Ford, Vice Provost and Dean of Graduate Studies

ACKNOWLEDGEMENTS

Please let me express my deepest appreciations to Dr. Mohammod Ali who is my advisor and mentor during my Master of Science study at University of South Carolina. I will cherish and honor all of what Dr. Ali has done for me throughout my student career.

I also would like to thank William Baron, James Tuss, David Zeppettella, and Jason Miller at the Air Force Research Laboratory located in Dayton Ohio for their mentorship and financial support of my Master's studies.

Finally, I would like to acknowledge my wonderful wife Lian and lovely daughter Emi. Their love and support gave me the ambition and will power to finish my Masters program and provide a better life for us all.

ABSTRACT

Conformal antennas have been increasingly playing an important role in a vast number wireless of communication applications. More specifically, Conformal Load Bearing Antenna Structures (CLAS) have drawn a great deal of interest among researchers and engineers because of their advantages of multiple functionality, e.g. antenna and structure both. The objectives of this thesis are to investigate and design innovative conformal Ultrawideband (UWB) endfire antenna arrays and reconfigurable aperture coupled pixel patch antennas both of which are good candidates for CLAS.

First, a broadband VHF-UHF end-fire Yagi-Uda array is proposed for possible air vehicle integration and operation within the 240-465 MHz frequency band. The array consists of a driven dipole, a reflecting dipole, and three directing dipoles. The broadband impedance, pattern, and gain responses are obtained by adding two parasitic metal strips adjacent to a fat driven strip dipole. The array has a peak gain greater than 7 dBi and Forward to Backward ratio (F/B) greater than 13 dB throughout most of the operating frequency band.

Second, a novel size reduced bi-layer UWB Log Periodic Dipole Array (LPDA) is proposed for operation in the 350-750 MHz UHF frequency band. The LPDA's overall size is reduced by using printed double meander-line elements on two separate dielectric surfaces. The array proposed in this work is fed using a coaxial cable and a conducting

tube. The effects of the diameter of each on the VSWR bandwidth of the array are thoroughly investigated. Simulations are also conducted considering dielectric support members between the layers and their effect on the antenna performance is studied. Finally, an array is fabricated and measured for VSWR, pattern, and gain all of which show satisfactory performance, e.g. 350-750 MHz operation bandwidth with good pattern coverage and peak gain greater than 7 dBi at most frequencies.

Finally, an aperture coupled reconfigurable pixel patch antenna is proposed that can be reconfigured in three frequencies with the help of low loss MEMs switches. Starting from the basic idea of a probe fed pixel patch controlled using MEMs switches investigations on an aperture coupled reconfigurable pixel patch are presented. The effects of substrate thickness, dielectric constant and loss tangent, bias networks, bias pads and vias are investigated and their effects on the performance of the reconfigurable antenna are evaluated. The proposed work shows that with an array of 5 mm by 5 mm pixels controlled by MEMs switches a patch can be reconfigured for operation at three frequencies with peak gain in the vicinity of 8 dBi. It is expected that the pixel patch concept can be further generalized to encompass a wide frequency range of reconfiguration providing more than an octave of bandwidth.

TABLE OF CONTENTS

LIST OF TABLES

LIST OF FIGURES

CHAPTER 1

INTRODUCTION

As improvements in the communication and navigation systems of air and land vehicles are made, new approaches to implement such systems are developed. The use of Multifunctional Antenna Structure (MAS) technology is one such way to take a new approach of implementation. Multifunctional Antenna Structures have the potential to radically alter structural design, whether it is for air or land vehicles that they are integrated in. MAS technology could allow a vehicle's RF communication system (receiving and transmitting wireless data) to adapt to more environmental situations and improve their operational capabilities. In aircrafts, MAS implementation can reduce the weight, drag, number of antennas. They can also improve the damage resistance of antenna apertures, and enhance the antenna radiation properties [1]. One type of the MAS concept that has had extensive research and development in the recent years is the Conformal Load Bearing Antenna Structures (CLAS) concept.

A conformal antenna is an antenna that conforms to something; in our case, it conforms to a prescribed shape. The shape can be some part of an airplane, high-speed train, or other vehicle. The purpose is to build the antenna so that it becomes integrated with the structure and consequently reduce weight, drag, and visibility to the human eye; for instance, in an urban environment. A major drawback to a conformal load bearing antenna

compared to its non-integrated counterparts is its complexity. The design, manufacture, technical support of CLAS will be more complex and intensive [2].

The main benefit of CLAS in air-vehicles is that they can replace many existing antennas, such as blades, wires, and dish that protrude from the aircraft. By using CLAS, reduces drag weight, and the volume of antennas needed to support all the transmitting and receiving functions of the existing antennas [1].

Clearly replacing externally mounted antennas with antennas that are flush to the Outer Mold Line (OML) will reduce drag. Many aircrafts can have up to a 100 of externally mounted antennas. Some antenna structures, such as reflecting dishes or planar arrays, are usually housed in radomes. While the radome does protect the antennas from the airstream and reduces the drag, the shape of the vehicle can depart significantly from the aerodynamic [2].

1.1 THESIS OBJECTIVE

While many types of antennas can be integrated into the CLAS concept ultrawideband (UWB) and reconfigurable antennas are of particular interest. Ultrawideband directional antennas with endfire beam, high gain, and large Forward to Backward (F/B) ratio are extremely sought after for many communication and radar applications. Moreover, if innovative size reduced UWB endfire antennas or antenna arrays can be developed for suitable integration into structural platforms that will be greatly advantageous.

The first objective of this thesis is to study and design innovative, size reduced UWB endfire antenna arrays. To that end, a Yagi-Uda array and a Log-Periodic Dipole

Array (LPDA) are investigated and designed. The Yagi-Uda array is very attractive due to its simplistic feeding technique. Broadband operational capabilities are achieved by employing the open sleeve dipole concept introduced in [3]-[4]. The novel LPDA introduced in this thesis consists of a bi-layer concept that meets realistic structural integration requirements. Aperture size reduction is achieved by using double meander-line elements proposed in [5]-[7].

The second objective of the thesis is to explore an innovative concept of a pixelated microstrip patch antenna concept. The proposed reconfigurable antenna has a broadside radiation pattern that can be reconfigured to operate at three different frequencies in the 1 to 1.5 GHz frequency range. The futuristic idea is to use the pixel structure proposed to be used as a single element in an array or to even have the capabilities to activate and deactivate switches to construct a vast number of different radiating apertures. The design process is complemented together with parametric studies to provide a better understanding of the antenna performance. Also, relevant simulations and their results are shown to take into consideration of the parasitic effects of the biasing network needed to activate the MEMs switches.

1.2 THESIS OUTLINE

This thesis is organized in four Chapters. In Chapter 2, a conformal broadband VHF-UHF Yagi-Uda end-fire array is proposed. In Chapter 3, a size reduced bi-layer Log Periodic Dipole Array (LPDA) is proposed for possible air-vehicle integration.

In Chapter 4, a reconfigurable aperture coupled pixel patch antenna structure using MEMs switches is proposed.

Finally, the conclusion and discussion on future work is presented in the last Chapter.

CHAPTER 2

A BROADBAND VHF-UHF YAGI UDA END-FIRE ARRAY

Planar low-profile high-gain end-fire array antennas are greatly desired for many commercial and military applications. Generally broad VSWR, pattern, and gain bandwidths are also required at the same time. While log-periodic dipole array (LPDA) or log-periodic slot array antennas (LPSA) have been widely used in the past the simplicity of a Yagi-Uda array has made it always attractive primarily because of the fact that only one element needs to be excited while all the other elements are parasitic. This ensures shorter cable length, less volume, and reduced weight all of which are critical for many applications. In the literature there are ample examples of LPDAs [8]-[9] and LPSAs. Similarly there are examples of Yagi-Uda arrays in many forms, eg. wire, printed, active, reconfigurable etc. [10]-[11]. In contrast, the objective of our work was to design a broadband VHF-UHF Yagi-Uda end-fire array with high gain (greater than 7 dBi across the band) and high Front to Back ratio (F/B) for possible air-vehicle integration. The broad VSWR, pattern, and gain bandwidths were obtained by employing the open sleeve dipole concept [3]-[4]. We also require that the 3 dBi gain beamwidth in both the vertical and horizontal planes are at least 60 degrees.

2.1 PRELIMINARY RESULTS AND PROPOSED ANTENNA GEOMETRY

In the beginning, a 7-element Yagi-Uda array was designed for operation in the 400-500 MHz frequency band. The number of elements was chosen to ensure high enough gain yet not to make the array size very large. The geometry of this array is shown in Figure 2.1. The array elements were printed on a 0.4 mm thick FR4 substrate. There was a 0.5 mm thick FR4 radome cover on the array elements as well. The total size of the array was 830 by 340 mm

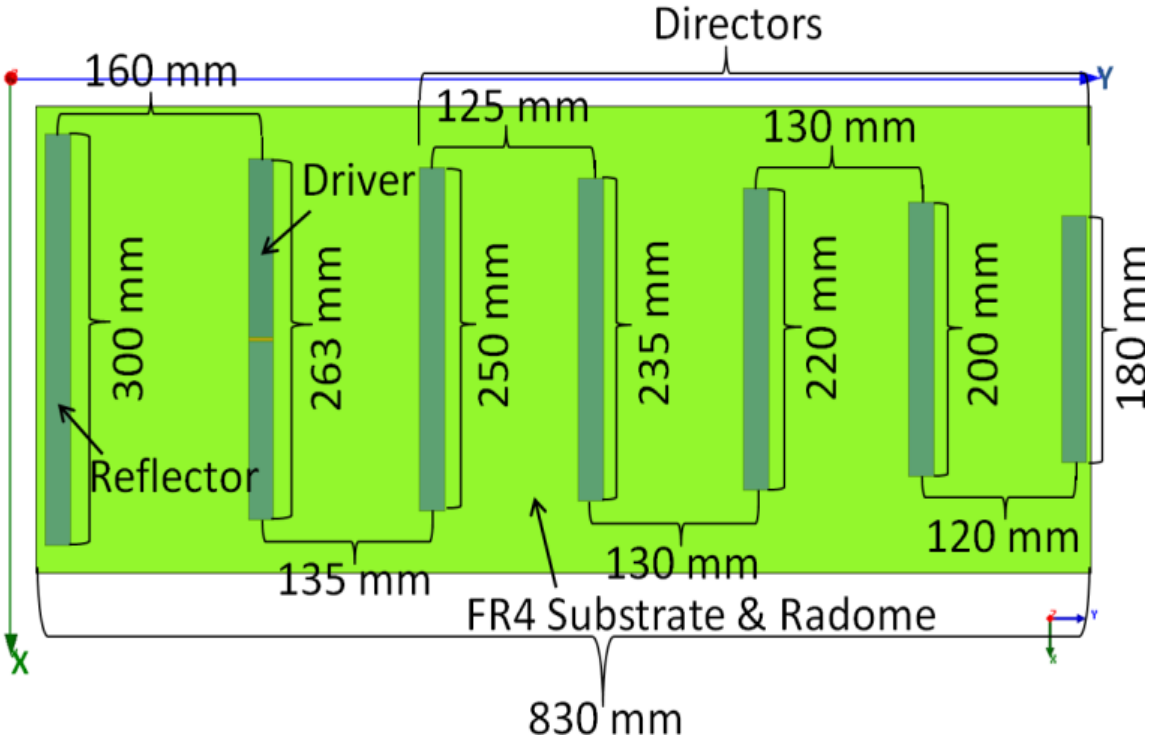

Figure 2.1 First UHF Yagi-Uda array configuration; array elements are on a 0.4 mm thick FR4 substrate and are also covered by a 0.5mm thick FR4 radome.

Array input and radiation characteristics were simulated using Ansys HFSS. Simulated VSWR data shown in Figure 2.2 show that the array operates from 440-484 MHz within 2:1 VSWR and thus has a very narrow bandwidth, approximately 9.5%. Elevation plane (phi=90 degree) patterns and azimuth plane (Theta=90 degree) patterns (Figure 2.3) show that the array gain at 440 and 462 MHz are 9.2 and 9.21 dBi respectively.

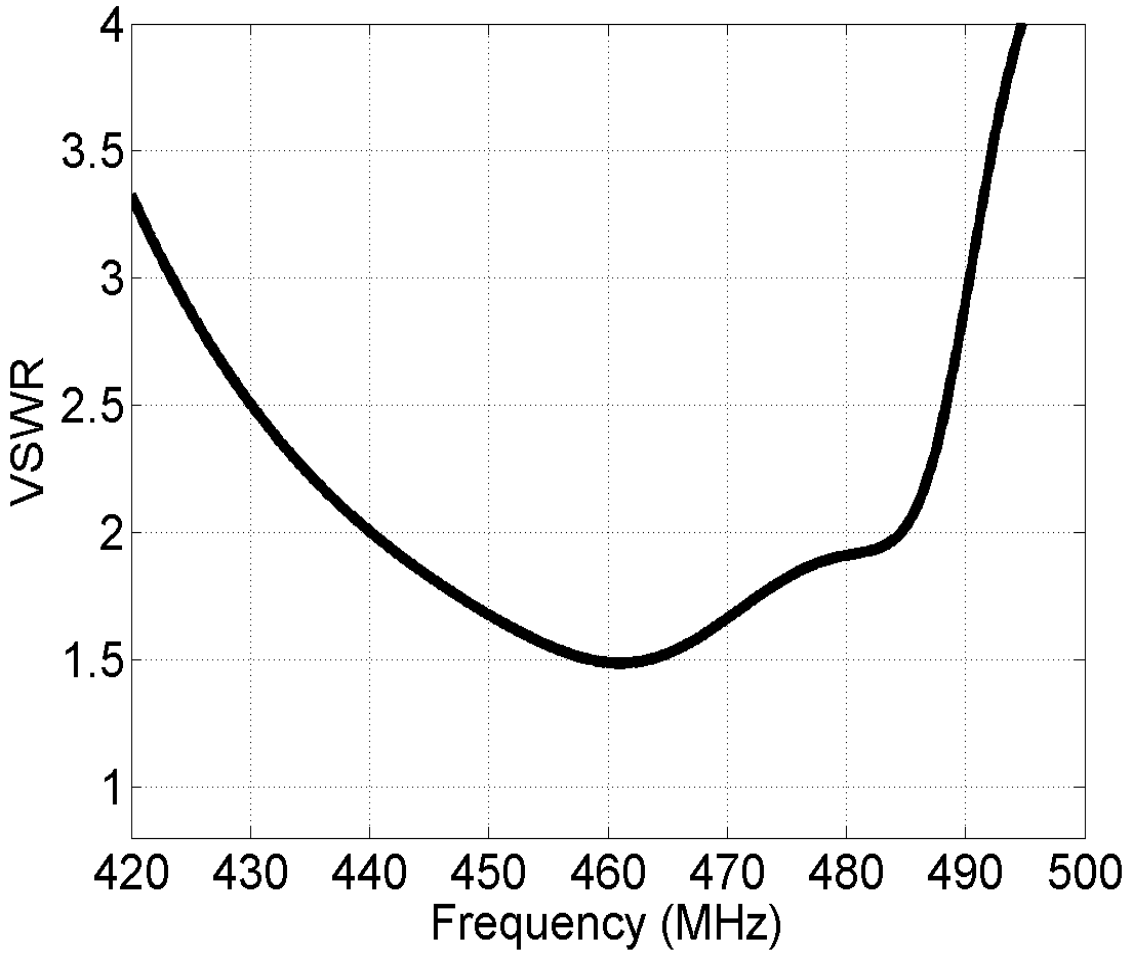

Figure 2.2 HFSS simulated VSWR characteristics of the Yagi-Uda array of Figure 2.1

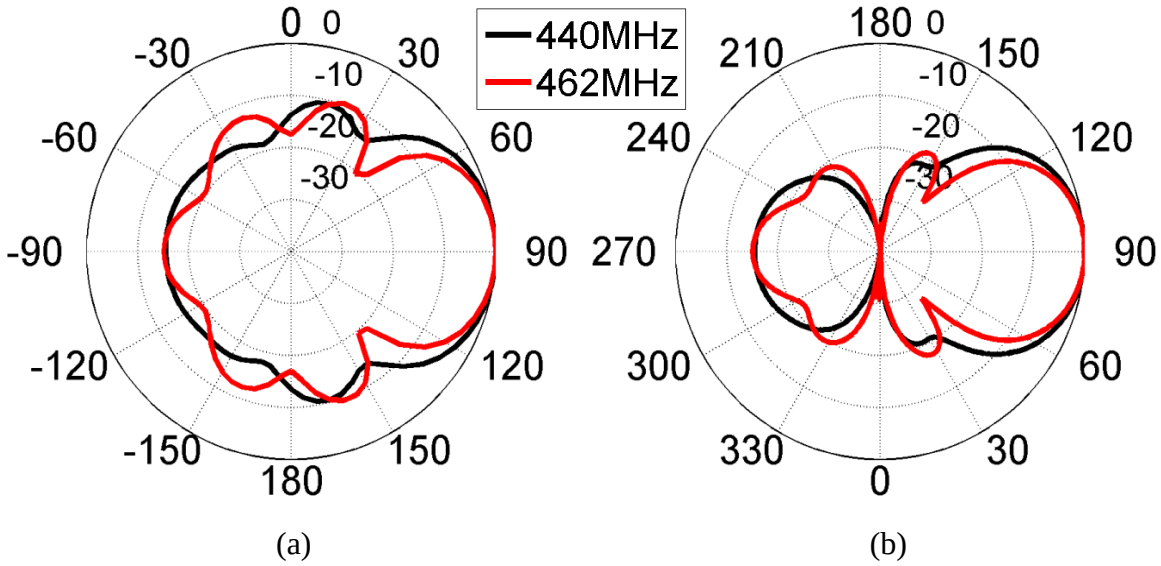

(a) (b)

Figure 2.3 Radiation patterns of array shown in Figure 2.1 in the (a) elevation plane and (b) azimuth plane

Since the array operating frequency was too high and also since the array bandwidth is very narrow further investigations were geared towards making the array broadband. Instead of a slender strip dipole a fat strip dipole was considered. Furthermore, following the works of King [3] on broadband open-sleeve dipoles a number of parasitic metal sleeves were added next to the driven dipole.

A parametric study was conducted to determine the sizes of the driven element and the parasitic metal strips and the spacing in between them. Details of the fat driven dipole and the parasitic metal strips are shown in Figure 2.4, which is a cross-sectional diagram showing the three-dimensional representation of the driven element. Where D = 30mm, SL = 250mm , S = 5mm and L = 516 mm. The elements and parasitic sleeves are all represented as thin copper traces with an H = << λ/50. Figure 2.5 and Figure 2.6 shows two Yagi-UDA arrays that use the driven element described above. Figure 2.5 has

a large plane reflector in the XZ plane. Figure 2.6 array has a flat "dipole" reflector in the XY plane.

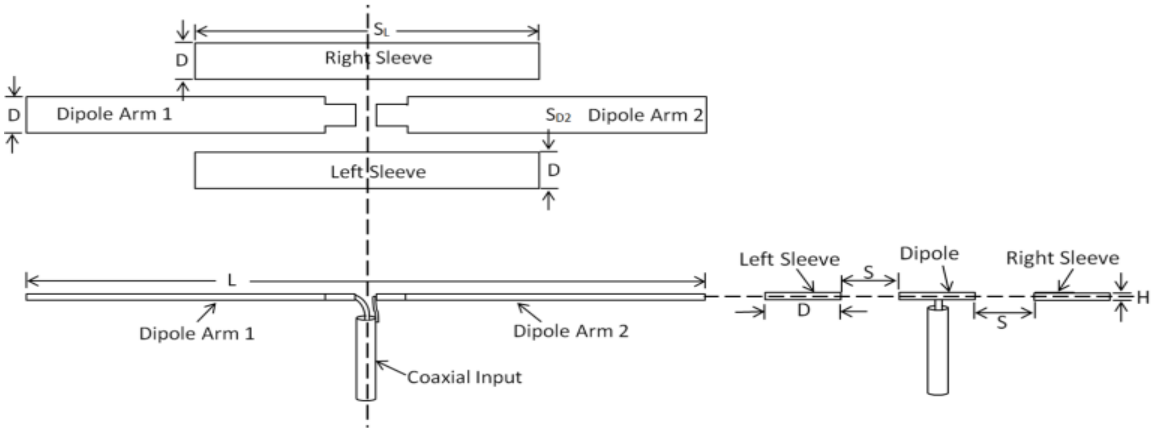

Figure 2.4 Driven wideband dipole with parasitic sleeves cross-sectional diagram

The arrays are approximately 725 mm long. The widest part of the array is the length of the reflector and both the large plane and dipole reflector are 946 mm long. The large plane reflector has a height in the XZ plane of 430 mm. The separation between the reflectors and the driven element is 230 mm. The separation between the first director and the driven element, the second director from the first and the third director from the second is 160mm. All the elements in the array have the same width of 30mm.

A third array is proposed where the array shown in Figure 2.5 has a sub and superstrate along the elements of the array, each 0.508mm thick. Roger 4003 was used to represent the sub and superstrate.

2.2 SIMULATION RESULTS

Simulated VSWR response of the three proposed arrays versus frequency is shown in Figure 2.8. The black curve shows the frequency response of the array with a large

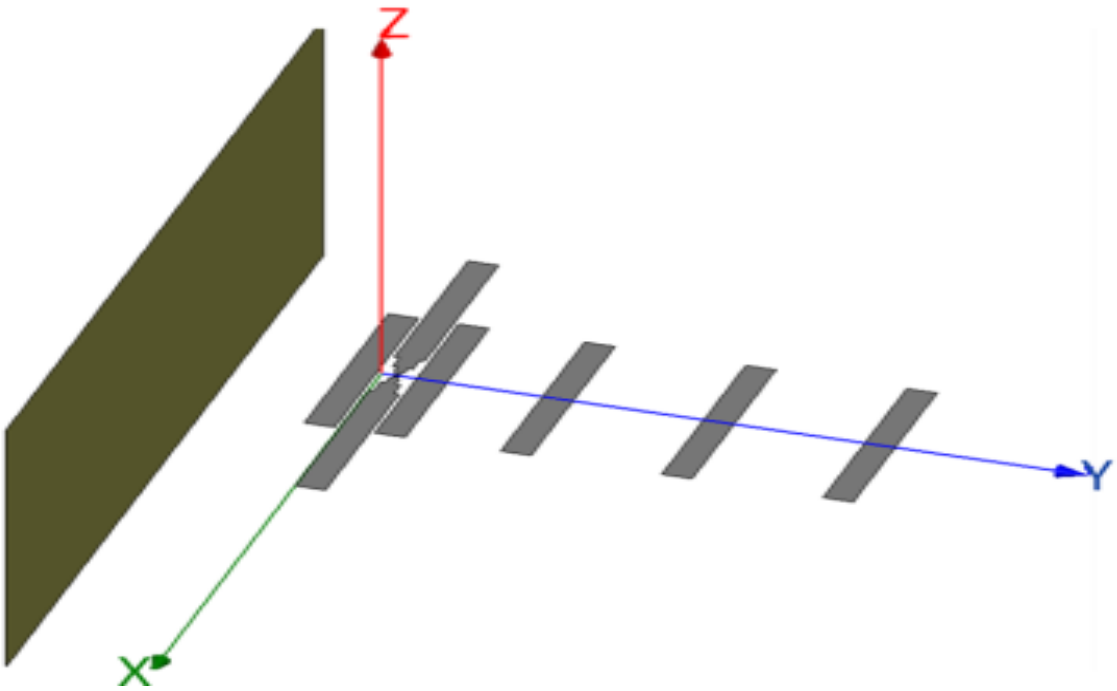

Figure 2.5 UHF Yagi-UDA array with large planer reflector

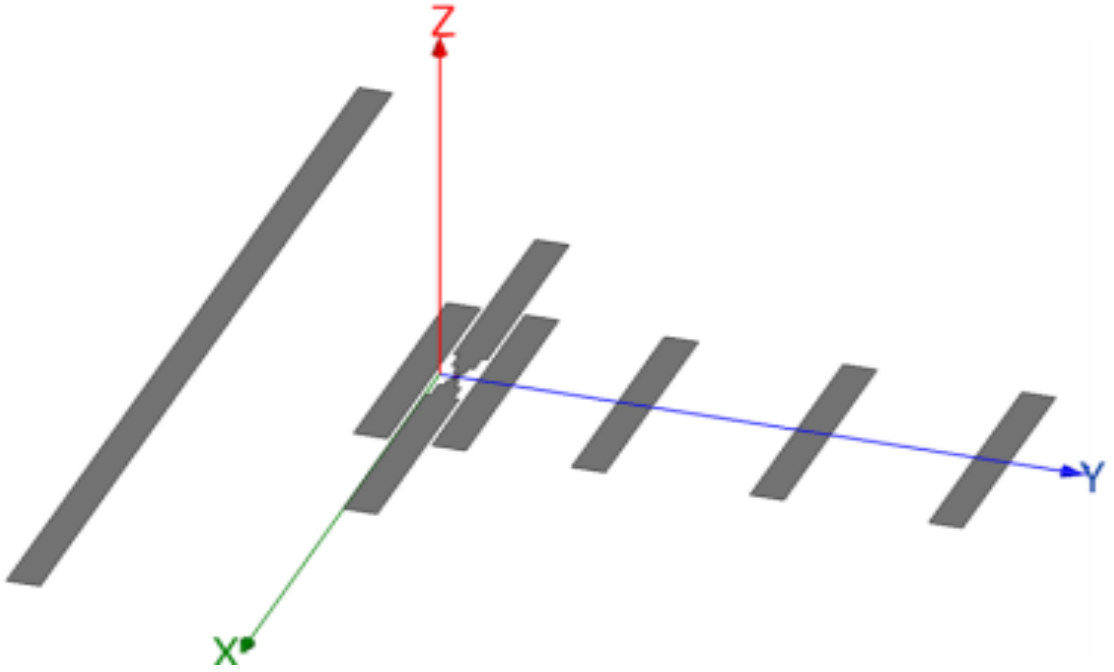

Figure 2.6 UHF Yagi-UDA array with dipole reflector

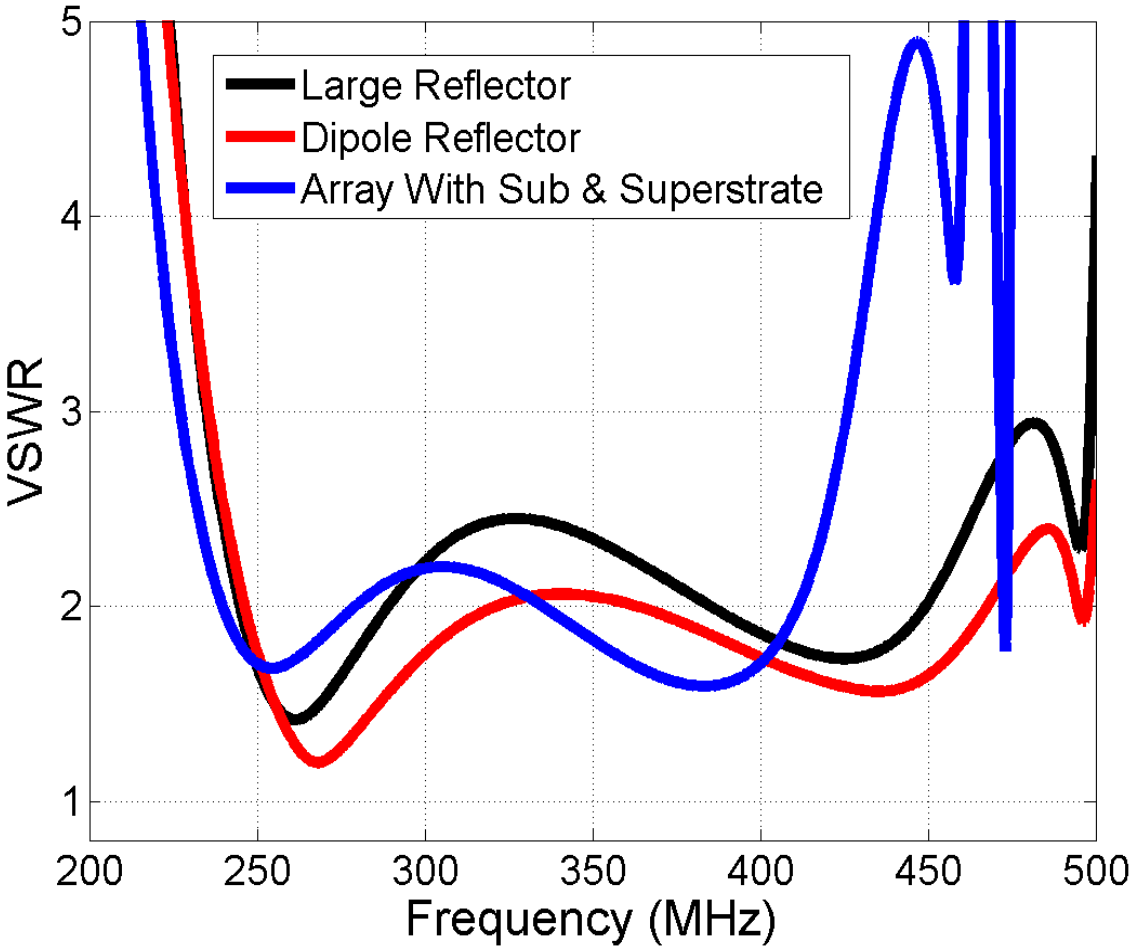

Figure 2.7 HFSS simulated VSWR characteristics of the three proposed Yagi-Uda arrays

planer reflector in the XZ plane, the red curve represents the array with a dipole reflector in the XY plane, and the blue curve shows the response of the array that contains the large planer reflector with a 0.508mm thick sub and superstrate both at which is normalized to a 75Ω input impedance.

Clearly the array with the dipole reflector in the XY plane has an increased operating frequency band that extends from 240 to 500 MHz within 2.5:1 VSWR. However we will show later that the radiation gain and pattern is not optimal with the dipole reflector. The array with the large reflector operates from 240 to 465 MHz and the

same array with a 0.508mm sub and superstrate operates from 232 to 420.5 MHz both within the 2.5:1 VSWR.The operational frequency bandwidth shown by the VSWR for the array with the large reflector, dipole reflector, and with the dielectric material are 63.8%, 70.2%, 57.7% respectfully. However even though the array with the dipole reflector has a larger operational bandwidth within the VSWR specifications, the gain and front to back ratio is unacceptably worse than the array with the large planer reflector.

Simulated elevation plane (phi=90^o) and azimuth plane (theta=90^o) realized gain patterns of the proposed Yagi-Uda arrays are shown in Figure 2.8, Figure 2.9, and Figure 4.10. Patterns computed at 240, 352.5, and 465 MHz are shown for the array containing the large plane and dipole reflector. Clearly both the arrays have a well-defined beam in both the elevation and azimuth plane.

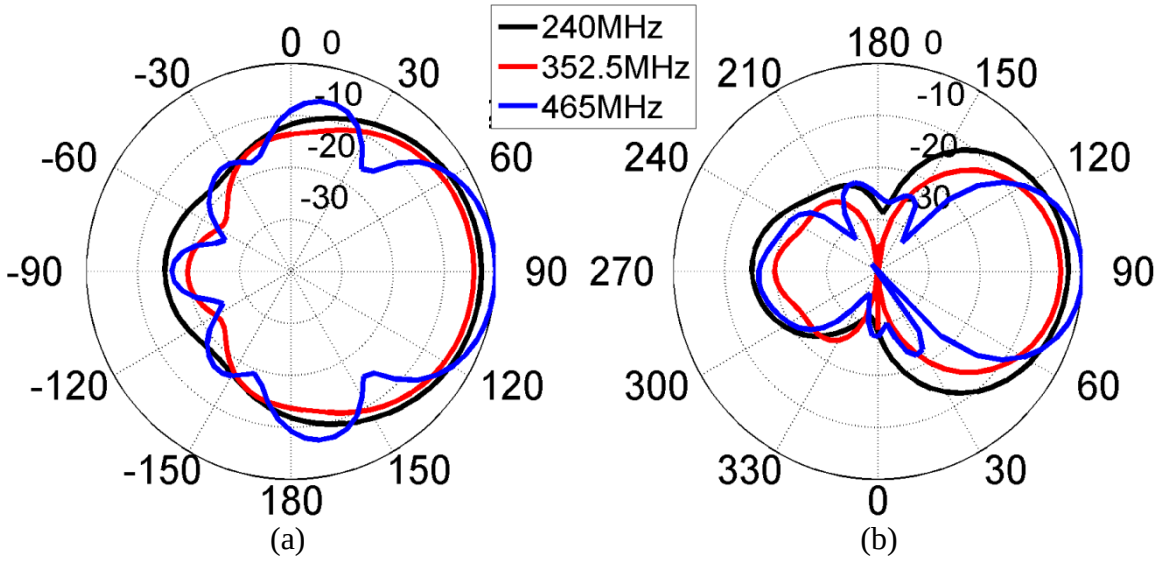

Figure 2.8 Radiation patterns of array shown in Figure 2.5 in the (a) elevation plane and (b) azimuth plane

However if you compare Figure 2.8 and Figure 2.9, the array with the plane reflector in the XZ plane have a better front to back ratio. A front to back ratio comparison of all there arrays is shown in later.

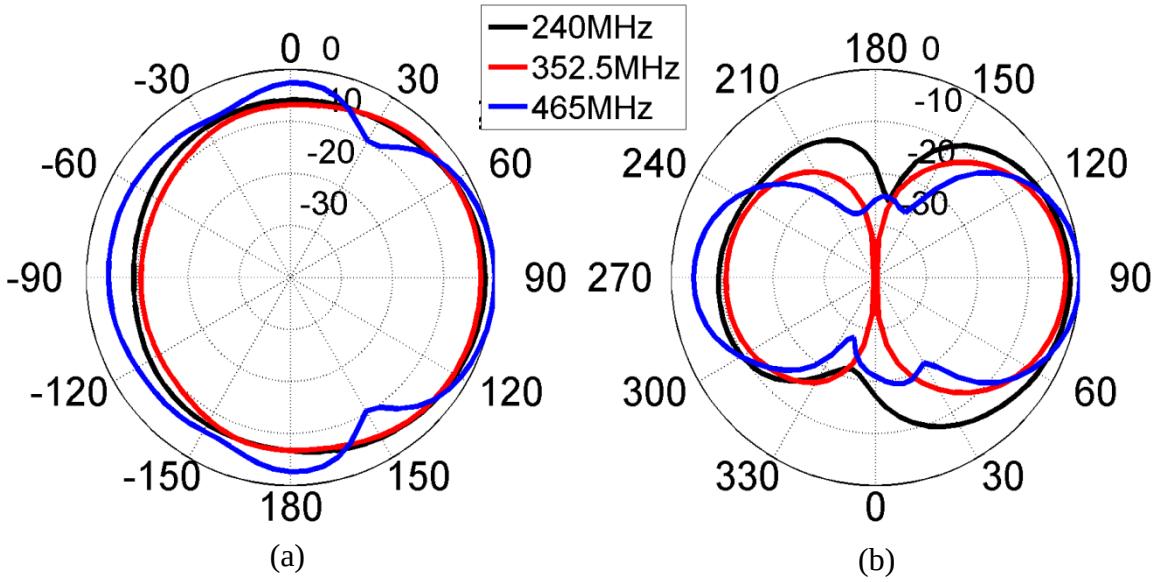

(a) (b)

Figure 2.9 Radiation patterns of array shown in Figure 2.6 in the (a) elevation plane and (b) azimuth plane

The peak forward gains of the arrays are compared in Figure 2.11. As you can see in Figure 2.11, the array with the large reflector has a much greater gain throughout the bandwidth which leads for the reason of using that array to apply the sub and superstrate. The radiation patterns of the array containing the sub and superstrate is shown in Figure 2.10 at 232, 326, and 420.5 MHz. The 3 dB beamwidths of the array with the large planer reflector in the elevation plane at 240, 352.5, and 465 MHz are 94, 94 and 56 degrees respectively. The 3 dB beamwidths in the azimuth plane at 240, 352.5, and 465 MHz are 70, 58 and 42 degrees respectively. Similarly the 3 dB beamwidths for the array with the dipole reflector (Figure 2.6) in the elevation plane at the same frequencies are 110, 140, and 72 degrees respectively. The 3 dB beamwidths in the azimuth plane are 72, 60 and 48

degrees respectively. The 3 dB beamwidths of the array with the sub and superstrate in the elevation plane at 232, 326, and 420.5 MHz are 130, 100 and 64 degrees respectively. The 3 dB beamwidths in the azimuth plane at 232, 326, and 420.5 MHz are 134, 60 and 48 degrees respectively. The 3 dB beamwidth is shown to be larger in the elevation plane with the array that has the dipole reflector and the beamwidth in the azimuth plane is closely comparable for both of the arrays. When the sub and superstrate is add to the array containing the large plane reflector, the beamwidth in both the elevation and azimuth plane increases.

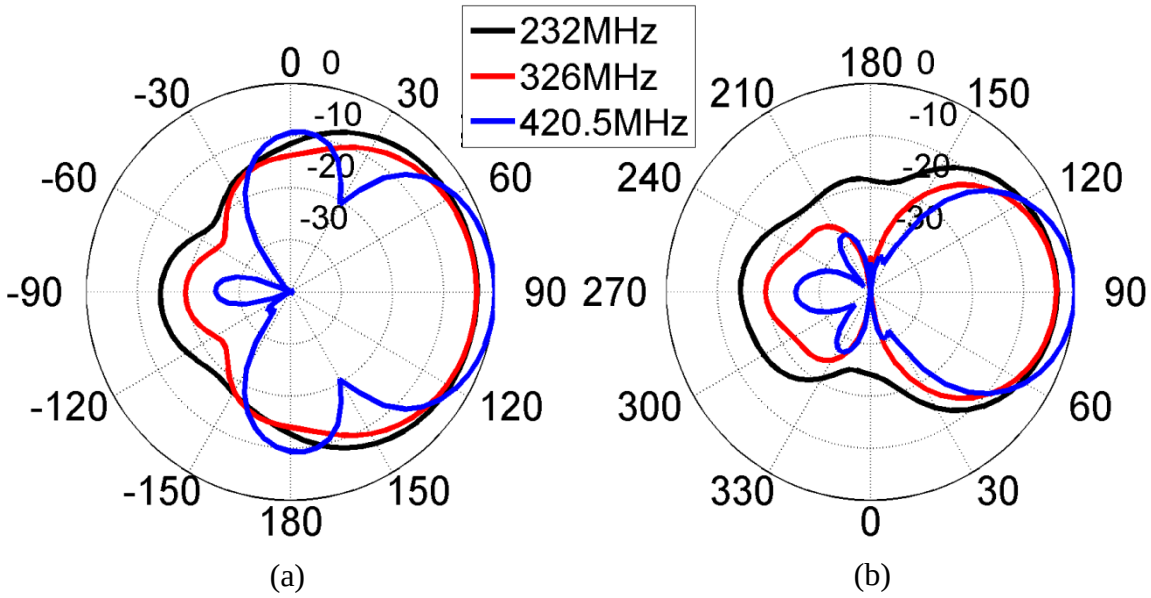

(a) (b)

Figure 2.10 Radiation patterns of array with sub and superstrate in the (a) elevation plane and (b) azimuth

Figure 2.11 and Figure 2.12 compares the max forward gain and F/B ratio for all three arrays from 230 to 465 MHz. Even though the array with the dielectric material does not operate after 420.5MHz, this frequency span was chosen for comparison reasons. The array with the dipole reflector only reaches a peak gain of 7 dBi after 430 MHz. The array with the large plane reflector has a gain greater than 7 dBi throughout most of the bandwidth. The only frequency at which the gain is below 7 dBi is from 310 to 340 MHz.

The green line shows the same array with a sub and superstrate which also has a gain above 7dBi throughout most of the frequency bandwidth. The only frequency at which this array has a gain below 7 dBi is from 270 to 310 MHz and after 460 MHz. The array with a dipole reflector maintains an F/B ration below 12 dB. The large reflector array in air and with dielectric material both maintain a front to back ratio greater than 12 dB throughout the bandwidth.

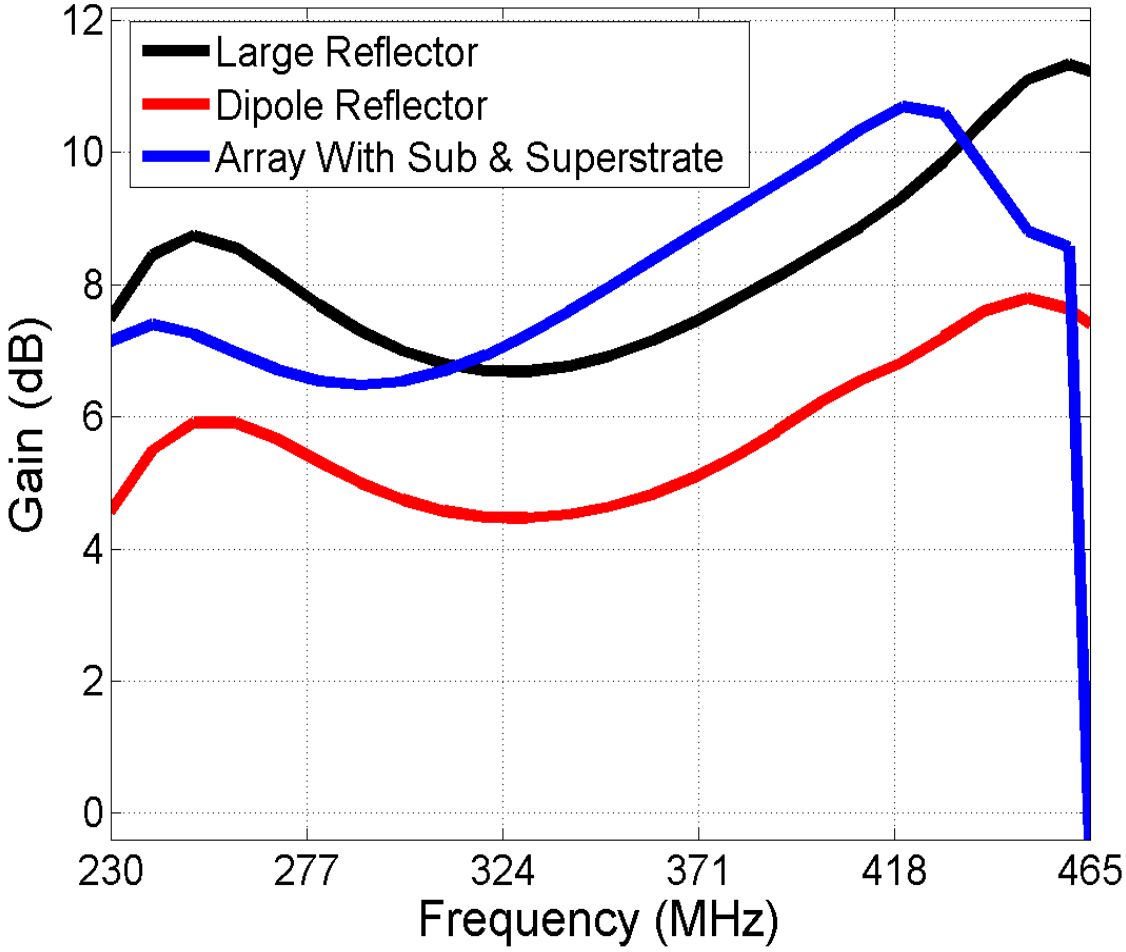

Figure 2.11 Max forward gain of the proposed Yagi-UDA arrays

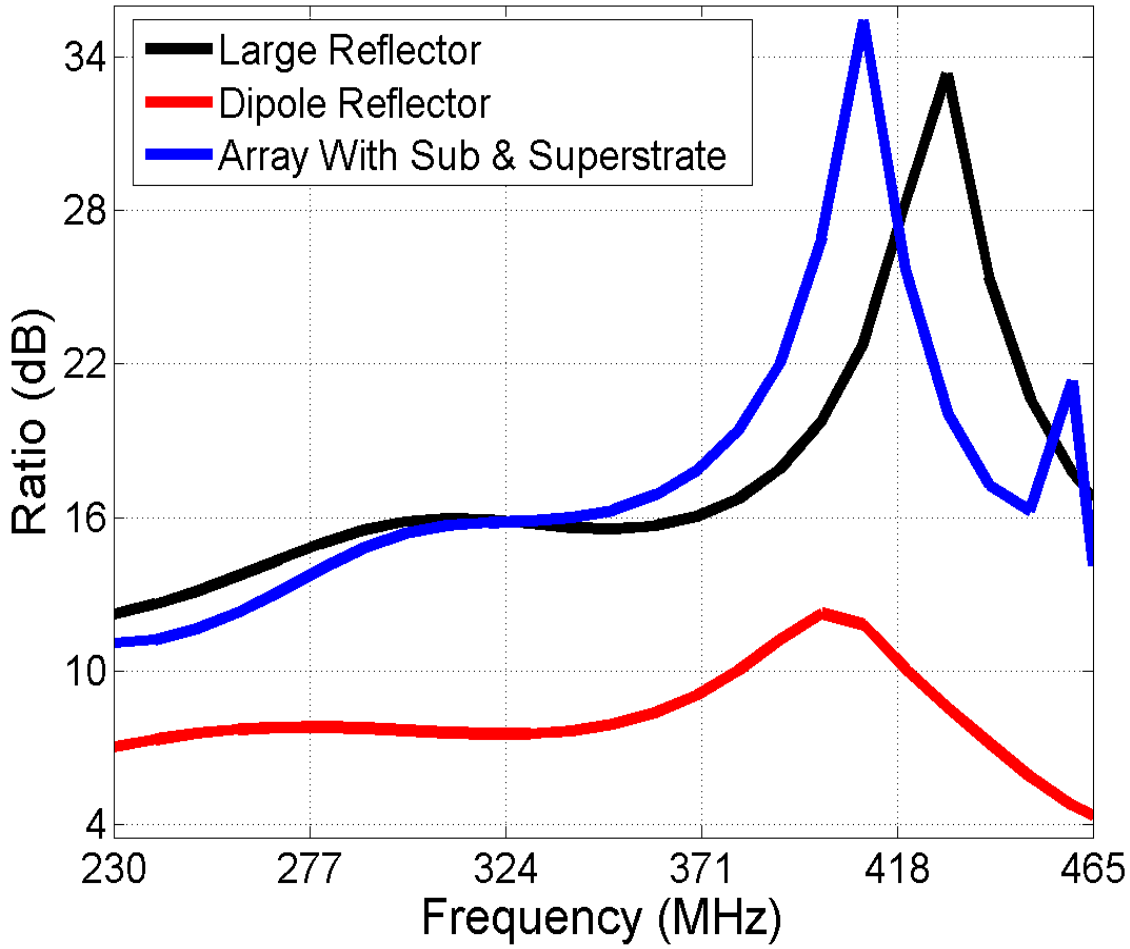

Figure 2.12 Front to back ratio of the proposed Yagi-UDA arrays

CHAPTER 3

A BROADBAND HIGH-GAIN BI-LAYER LPDA FOR UHF APPLICATIONS

The study of Log Periodic Dipole Antennas (LPDAs) dates back many decades [12]-[38]. LPDAs have been studied and designed for operation in free-space [12]-[15] as well as in printed configurations [16]-[19].The works in [18]-[19] propose a new technique to design and build stripline fed LPDAs in the microwave frequency band. These designs consider low dielectric constant materials and thin (few mm) printed embodiments. A printed meander dipole LPDA was proposed in [20] for operation from around 2-4.5 GHz. The peak array gain achieved was 7.5 dBi. Approximately 12% size reduced (Log Periodic Koch Dipole Arrays) LKPDAs were proposed in [21]. These microstrip LKPDAs operate from 2-3.2 GHz.

An LPDA design for ultrawideband pulse radiation has been proposed in [22]-[23]. More recently a microstrip-fed band notched UWB LPDA was proposed in [24] for operation in the 4-10 GHz frequency range. The array peak gain was in the vicinity of 5 dBi.

It is apparent that many design examples of microstrip or stripline fed LPDAs exist for frequencies 1 GHz or higher. Similarly relatively low-gain (4dBi) UHF LPDAs also exist that consist of two very closely spaced dipole layers fed using a coaxial line. Yet for many airborne, space, and ground vehicle applications structural integration of broadband

LPDAs require that the radiating layers be substantially spaced apart, be high gain (preferably 7 dBi or higher) and broadband (one octave or wider). Moreover, the presence and effect of dielectric or conductive materials nearby should also be accounted for in the design. This is the focus of this chapter.

We present the study and design of a broadband size-reduced LPDA for operation in the 350-750 MHz UHF frequency band. Unlike conventional LPDAs the proposed structure consists of a novel bi-layer geometry where the printed dipole elements are disposed of on two separate dielectric surfaces. These dielectric surfaces even when separated by substantial distances can support a broadband radiating aperture. To reduce the aperture width double meander-line elements are adapted from [5]-[7] because of their advantage in miniaturization as well as bandwidth. The aperture proposed in this work is fed using a coaxial cable and a conducting tube. The effects of the diameter of each on the VSWR bandwidth of the array are thoroughly investigated. Finally, an aperture is fabricated and measured for VSWR, pattern, and gain all of which show satisfactory performance.

3.1 APERTURE GEOMETRY

The geometry of the double meander element used as the building block of this LPDA is shown in Figure 3.1. The length of each horizontal element is e_1 while the length of each vertical element is e_2. The trace width of the conductor that makes the double meander is defined as T_n. The resonant dimensions of a double meander element were approximately determined following the guidelines found in [5]-[7]. For example, consider the frequency of 350 MHz a resonant straight conductor dipole will be about

420 mm long if made using narrow width conducting strips in air. Whereas a double meander element was found to be 300 mm long and 30 mm wide. Thus about 30% shortening in length was achieved with the help of 30 mm expansion in the lateral direction.

The proposed UHF LPDA array structure is illustrated in Figure 3.2. The length and width of the total array aperture are AL and $2L_1$ respectively. The two substrates containing the printed dipole elements are separated by a distance H which may contain a dielectric medium with dielectric constant, ε_{r1}. Each substrate is t mm thick and has a dielectric constant of $\varepsilon_{r2.}$

The dotted outlines in Figure 3.1 show the space within which each dipole half element is located. The dotted outlined element arm represents the bottom layer of the array. The dipole half arms on the top layer are connected with the outer conductor of the feeding 50 Ω coaxial cable while the dipole half arms on the bottom layer are connected to a hollow conducting tube. The conducting tube is in turn connected to the inner conductor of the coaxial cable at the tapered edge of the aperture. Since the inner conductor of the coax is made of a solid conductor it increases the weight of the overall structure. Furthermore, it is preferable to have thin, flexible, lightweight cables for size, routing, and weight advantage. Thus cases consisting of thin cable and fat conducting tube are also investigated as will be reported later on in the paper.

The inter-element spacing's and the subsequent dipole lengths of the LPDA were generally determined using the well-known log-periodic equations: (5-1) – (5-2)

Initially a single meander line dipole antenna was simulated in isolation in air to determine the resonant dimensions of the longest element. These dimensions were determined considering a good impedance match and radiation properties.

$$\tau = \frac{L_n}{L_{n-1}} \qquad 5\text{-}1$$

$$\sigma = \frac{D_{n-1}}{2L_{n-1}} \qquad 5\text{-}2$$

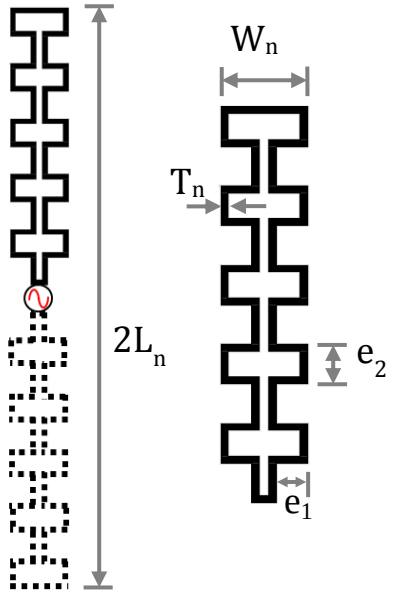

Figure 3.1 The meander line dipole element and its parameters

Subsequently investigations on UHF LPDAs were carried out in steps. The first LPDA designed consisted of two meander line LPDA layers separated by a distance of *H*=10 mm. Air was the medium filling the space in between the bi-layers. This was a starting design and the geometrical dimensions and parameters of the LPDA are listed in Table 3.1. The element dimensions were based off the log periodic equations and the

Carrel curves [12]-[13]. For a design gain of 9 dBi τ=0.917 and σ=0.169. All antenna traces and feeding cable plus tube were modeled using copper as the conductor.

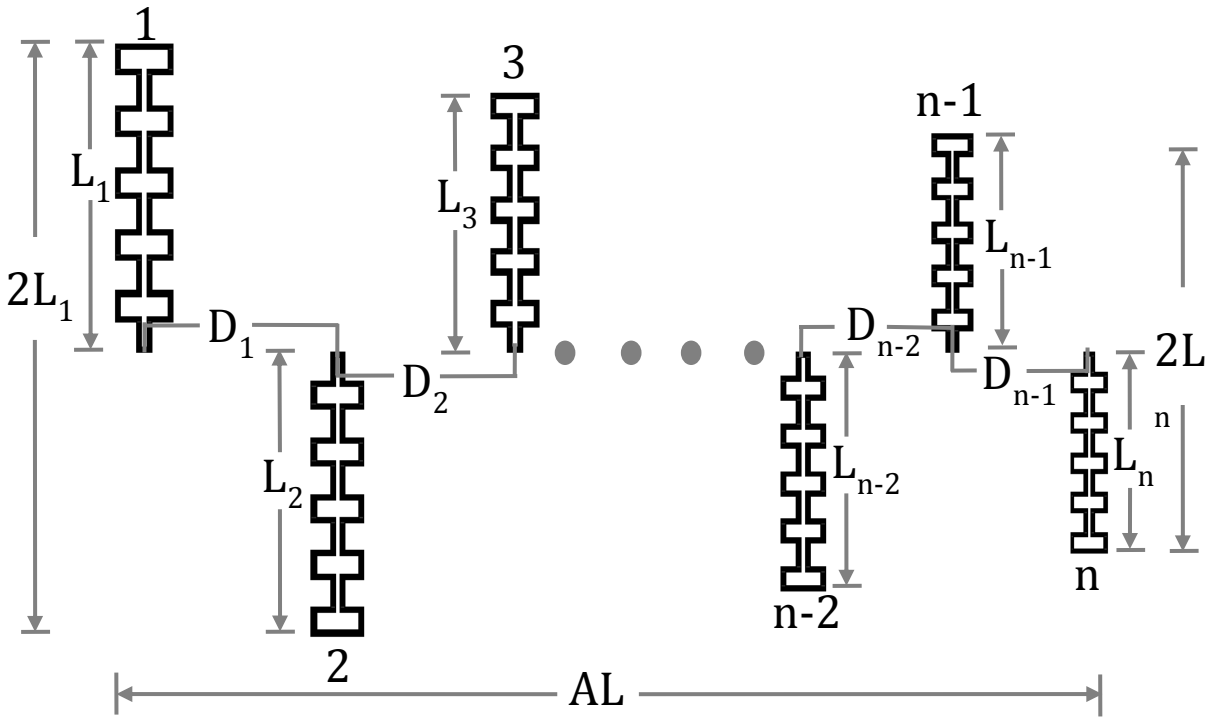

Figure 3.2 The proposed meander line LPDA and its parameters. Only one layer is shown. The other layer is a copy and 180 degree reflection of the one shown here.

3.2 SIMULATION RESULTS

The feeding arrangement of the LPDA in HFSS is depicted in Figure 3.3(a). The parameters of the coaxial cable and the conducting tube are also defined. The coax and tube have the same outer and inner diameter defined as *a* and *c*. The center conductor of the coax has a diameter of *b*. The dielectric constant is ε_r . The total distance between the two layers is *H*. At the onset of the cable a lumped gap source was used as the excitation. As can be seen in Figure 3.3(a) the lumped gap source is a rectangle that connects the center conductor to a conductive plate that is shorted to the outer conductor of the coax. Simulated VSWR results for this LPDA are shown in Figure 3.3(c).

Table 3.1 Geometrical dimensions of the meander line LPDA in air.

Element #, n	**1**	**2**	**3**	**4**	**5**	**6**	**7**	**8**	**9**	**10**	**11**	**12**
Length, L_n (mm)	300.0	275.1	252.3	231.3	212.1	194.5	178.4	163.6	150.0	137.5	126.1	115.7
Width, W_n (mm)	30.0	27.5	25.2	23.1	21.2	19.5	17.8	16.4	15.0	13.8	12.6	11.6
Trace Width, T_n (mm)	3.0	2.8	2.5	2.3	2.1	1.9	1.8	1.6	1.5	1.4	1.3	1.2
Distance, D_n (mm)	101.4	93.0	85.3	78.2	71.7	65.7	60.3	55.3	50.7	46.5	42.6	N/A
e_1 (mm)	10.5	9.6	8.8	8.1	7.4	6.8	6.2	5.7	5.2	4.8	4.4	4.0
e_2 (mm)	15.0	13.8	12.6	11.6	10.6	9.7	8.9	8.2	7.5	6.9	6.3	5.8

Clearly the array operates from 350-750 MHz within a VSWR of 2:1. The radiation patterns in both the azimuth and elevation planes were found to be directional with F/B ranging from 27.3-13.2 dB and peak realized gain was from 9.0-7.8 dBi.

To investigate the feasibility of adding dielectric materials two other LPDA cases were also studied. One was when the space in between the two LPDA layers were filled using a 10 mm thick FR4 dielectric slab for which areas where the coax and the tube were located FR4 materials were removed in HFSS. The other model consisted of each LPDA layer being supported by a 1.58 mm thick FR4 substrate. Thus the space in between the layers was empty. The first case with 10 mm thick FR4 is an extreme case but gives some insight as to what can be expected if the whole space is filled with a dielectric material while the second case is clearly relevant for future fabrication.

The results obtained from these models are compared in

Figure 3.5. The baseline LPDA results in air are also plotted for comparison. The black trace represents the VSWR of the LPDA in Air. The red trace represents the results of the LPDA on 1.58 mm thick FR4. For this case also H=10 mm. Finally, the blue trace represents the results of the LPDA with a 10mm thick FR4 dielectric slab in between the layers. Clearly having a thick dielectric slab in between the layers significantly detunes the array and is thus not acceptable for the premises of this work. But as expected the LPDA in air and the one on 1.58 mm thick FR4 perform much better (both satisfy the 350-750 MHz bandwidth requirements).

For effective structural integration it is generally necessary to place the bi-layers of the LPDA sufficiently separated from each other.

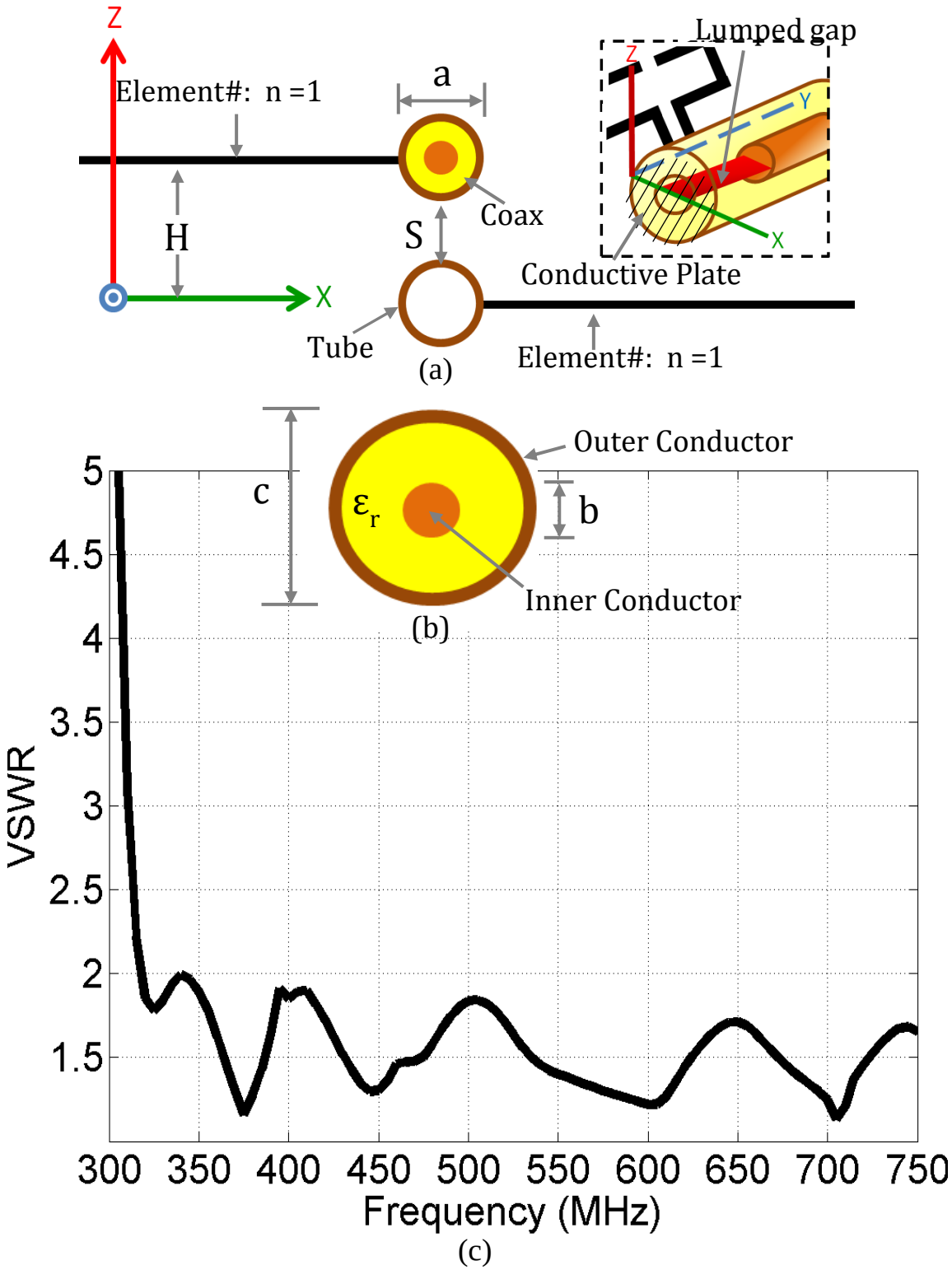

Figure 3.3 (a) Feed coax and antenna trace location, HFSS feeding, (b) coax dimensions, and (c) simulated VSWR data of the UHF LPDA in air; H=10 mm, a=7.5 mm, S=2.5 mm, b=2 mm, c=6.7 mm, εr=2.2 mm, and tanδ=0.001.

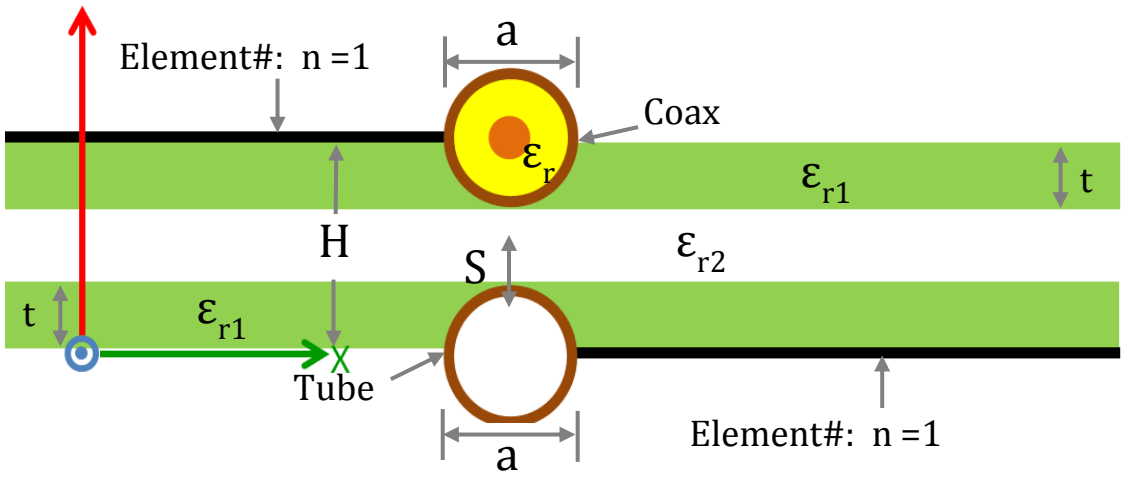

Figure 3.4 The UHF LPDA supported by various dielectric materials.

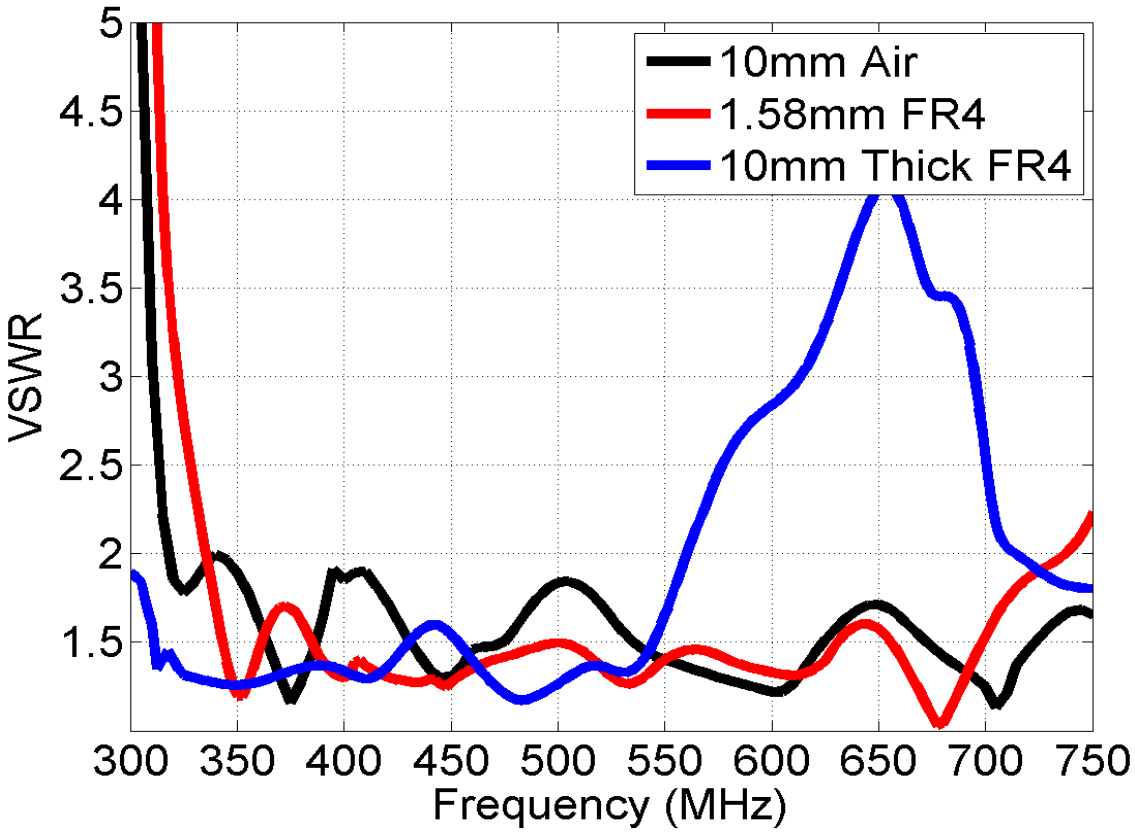

Figure 3.5 Simulated VSWR comparison between three LPDA cases: black line - the baseline design in air ((thus both εr1 and εr2 is air, H=10 mm) red line - layers on t=1.58 mm thick FR4 (thus εr1 is FR4 but εr2 is air, H=10 mm); blue line - Layers separated by a 10 mm thick FR4 dielectric slab (thus both εr1 and εr2 are FR4, H=10 mm). For all cases cable parameters are: a=7.5 mm, b=2 mm, S=2.5 mm, c=6.7 mm, εr=2.2, and tanδ=0.001.

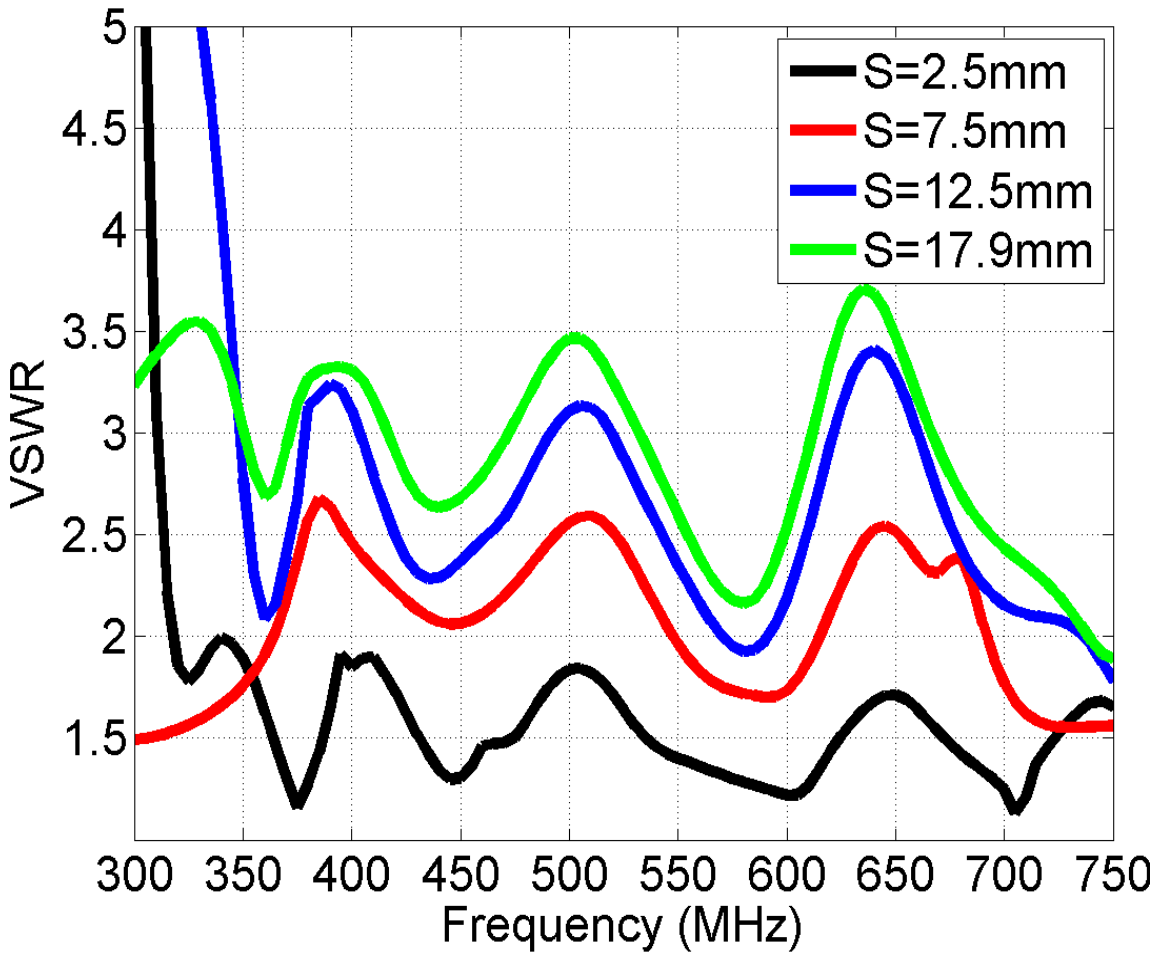

Figure 3.6 The effect of the separation, S between the two layer LPDA. For all cases cable parameters are: a=7.5 mm, b=2 mm, c=6.7 mm, εr=2.2, and tanδ=0.001.

This spacing may range from 12.5 mm to 40 mm. To understand the effect of this increased spacing on the array VSWR parametric simulations were conducted (see Figure 3.6). Since the outer diameter, *a* of the feed coax and the tube were both 7.5 mm S=2.5, 7.5, 12.5, and 17.9 shown in Figure 3.6 means that the two layers are separated by a distance of H=10, 15, 20, and 25.4 mm. There is no dielectric material present to support or cover the array. As apparent, any major increase in the spacing, S between the coax and the tube degrades the VSWR significantly. This is because the characteristic impedance of the balanced transmission line formed by the outer conductor of the coax

and the tube increases with increasing S and hence presents a worse impedance match for the array.

To circumvent this problem we decided to use the feeding scheme shown in Figure 3.7. If the coax and the tube are arranged as shown with respect to the antenna elements then the distance between the elements could be increased while keeping the distance between the coax and tube outer surfaces to a minimum.

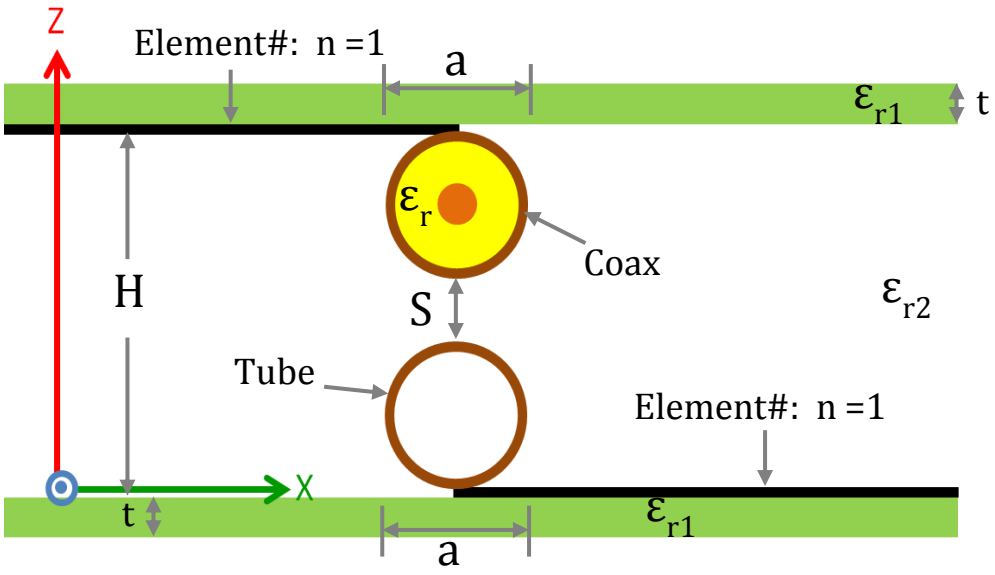

Figure 3.7 New feeding arrangements for the UHF bi-layer LPDA, which allows increased separation between the two layers.

Simulated VSWR data versus frequency for the new feeding arrangement are shown in

Figure 3.8. For the new arrangement the separation obtained is 25.4 mm or 1 inch while for the previous arrangement it was 10 mm. Note that the coax and tube diameters also increased for the new arrangement. As apparent the VSWR data for the new arrangement show satisfactory performance which is in direct contrast with the data presented in Figure 3.8

Computed peak realized gain data of the two UHF LPDAs are listed in Table 3.2. It is evident that either approach gives about similar gain except at the lowest frequency, 350 MHz where the baseline design gives higher gain.

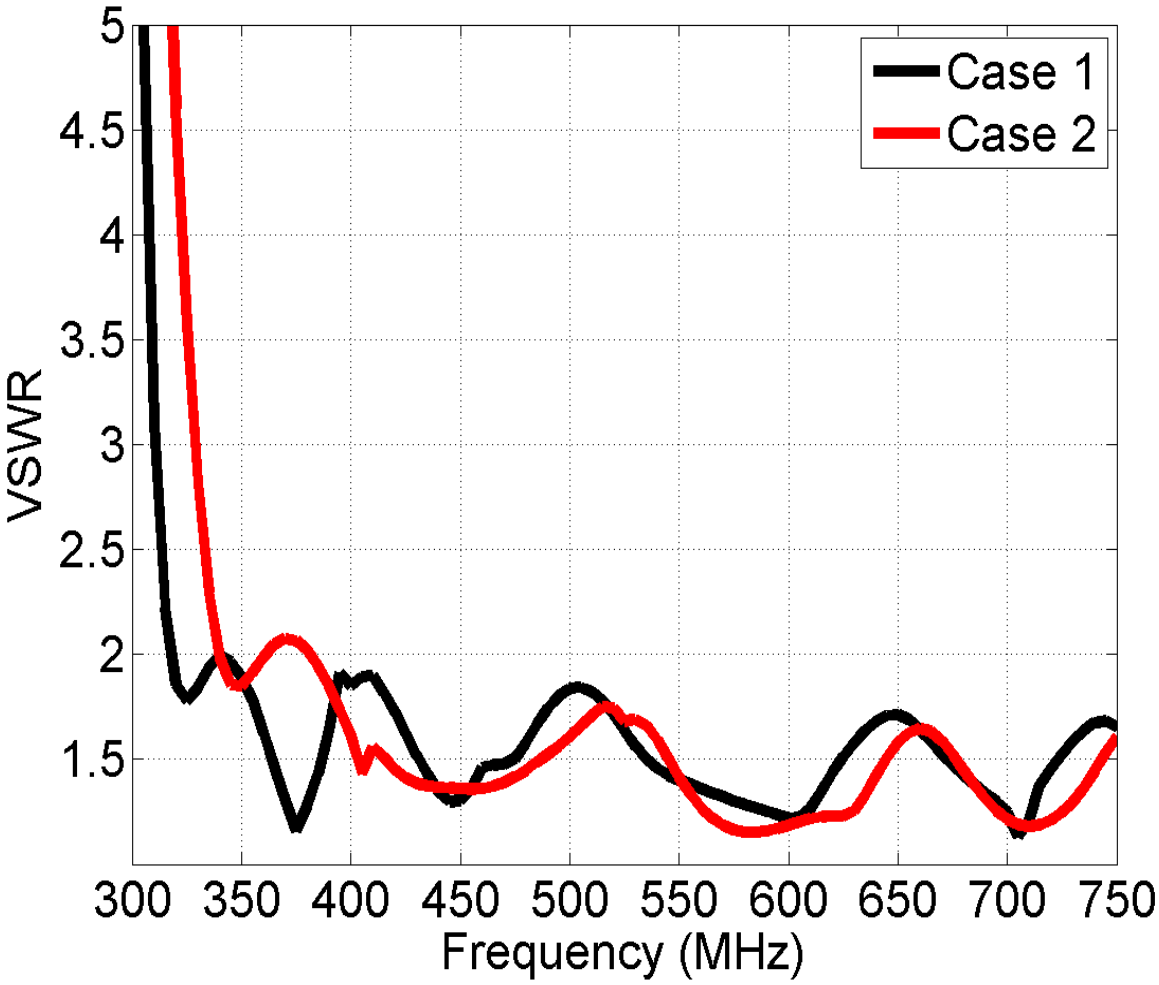

Figure 3.8 Simulated VSWR results of the LPDA considering two cases: black trace representing the Baseline LPDA (cable parameters are: a=7.5 mm, b=2 mm, εr=2.2, c=6.7 mm; H = 10mm; S = 2.5mm) and the red trace represent the new LPDA feed arrangement (cable parameters are: a=11 mm, b=3 mm, εr=2.2, c=10.4 mm; H = 25.4mm; S = 3.4mm). In both cases εr1=1.0 and thus no dielectric substrate present.

Table 3.2 Computed peak realized gain (dBi) of the UHF LPDA. In both cases ε_{r1}=1.0 and thus no dielectric substrate present.

Frequency (MHz)	350	400	450	500	550	600	650	700	750
Case 1: H = 10 mm, S=2.5 mm, Gain (dBi)	9.0	8.1	8.3	8.5	9.0	8.6	7.8	8.0	8.1
Case 2: H=25.4 mm, S=3.4 mm, Gain (dBi)	6.3	8.1	8.9	8.8	9.1	8.7	7.3	7.5	7.3

Table 3.3 Computed Forward to Backward ratios (F/B) of the UHF LPDA. In both cases ε_{r1}=1.0 and thus no dielectric substrate present.

Frequency (MHz)	350	400	450	500	550	600	650	700	750
Case 1: H = 10 mm, S=2.5 mm, Gain (dBi)	13.3	25.4	16.4	25.0	27.3	20.2	24.0	21.0	17.9
Case 2:H=25.4 mm, S=3.4 mm, Gain (dBi)	8.0*	17.5	19.4	15.8	20.3	17.9	15.8	15.3	18.0

Computed Forward to Backward ratios (F/B) of the UHF LPDA representing the two cases shown in

Figure 3.8 are listed in

Table 3.3. It is clear that the new feeding arrangement has low F/B throughout the frequency range. This is essentially because of the increased separation between the two arms of the same dipole which are at 25.4 mm distance as opposed to 10 mm distance before. Nevertheless, except for the lowest frequency the F/B is greater than 15 dB which is satisfactory for most applications.

Computed normalized radiation patterns in the elevation and azimuth planes for both cases are shown in Figure 3.9 and Figure 3.10. The patterns are directional, and symmetric. Within the frequency range of operation the half-power (3-dB) beamwidths for case 1 in the elevation plane ranges from 92 to 64 degrees while that in the azimuth

plane ranges from 64 to 38 degrees and for case 2 it ranges from 97 to 74 degrees and 64 to 54 degrees in the respected planes.

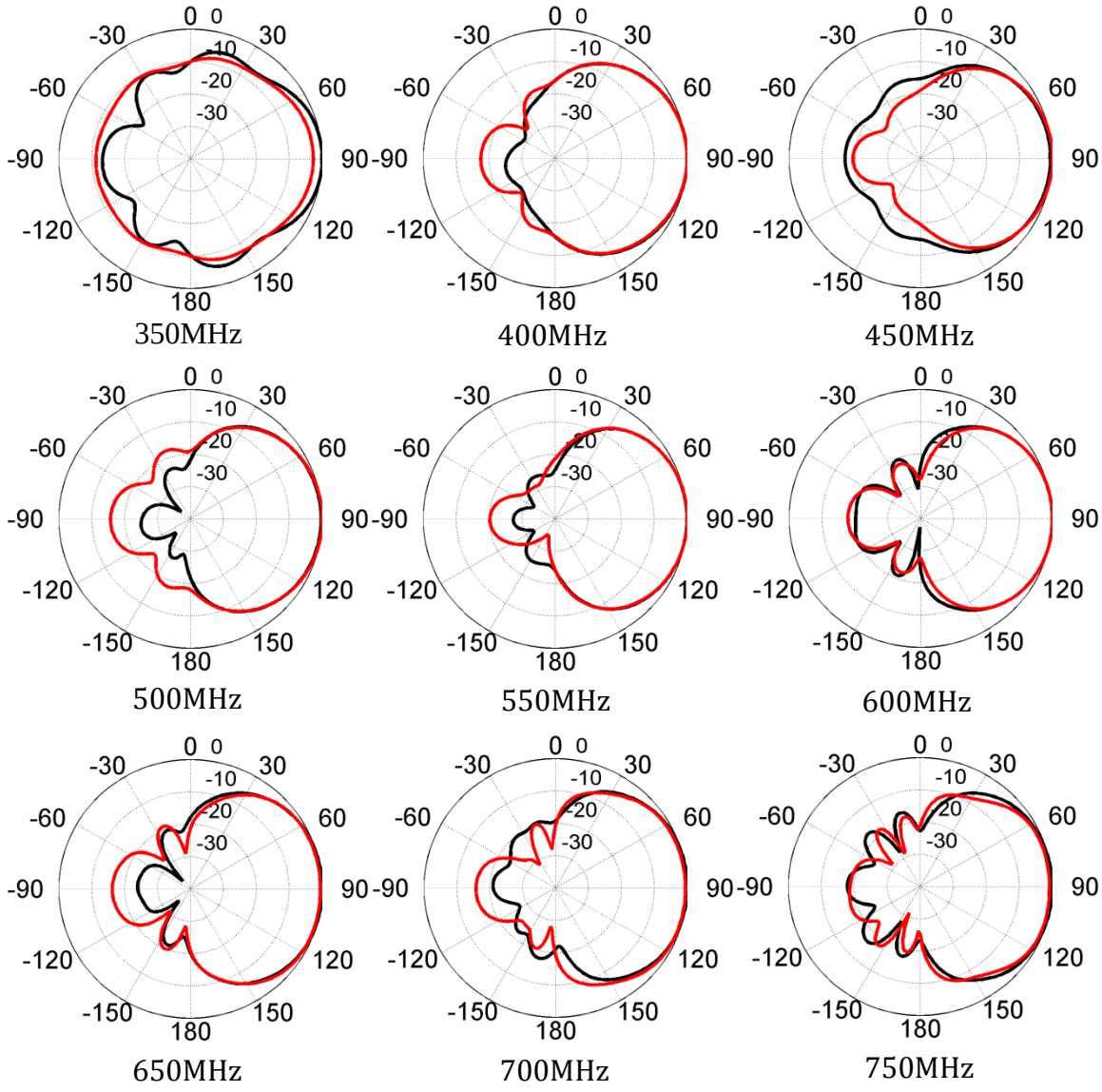

Figure 3.9 Computed normalized patterns of the UHF LPDA in the elevation plane (yz-plane or phi = 90o). Two cases: black trace representing Case 1 (Cable parameters: a=7.5 mm, b=2 mm, εr=2.2, c=6.7 mm; H = 10mm; S = 2.5mm) and the red trace representing Case 2 (Cable parameters: a=11 mm, b=3 mm, εr=2.2, c=10.4 mm; H = 25.4mm; S = 3.4mm). In both cases εr1=1.0 and thus no dielectric substrate present.

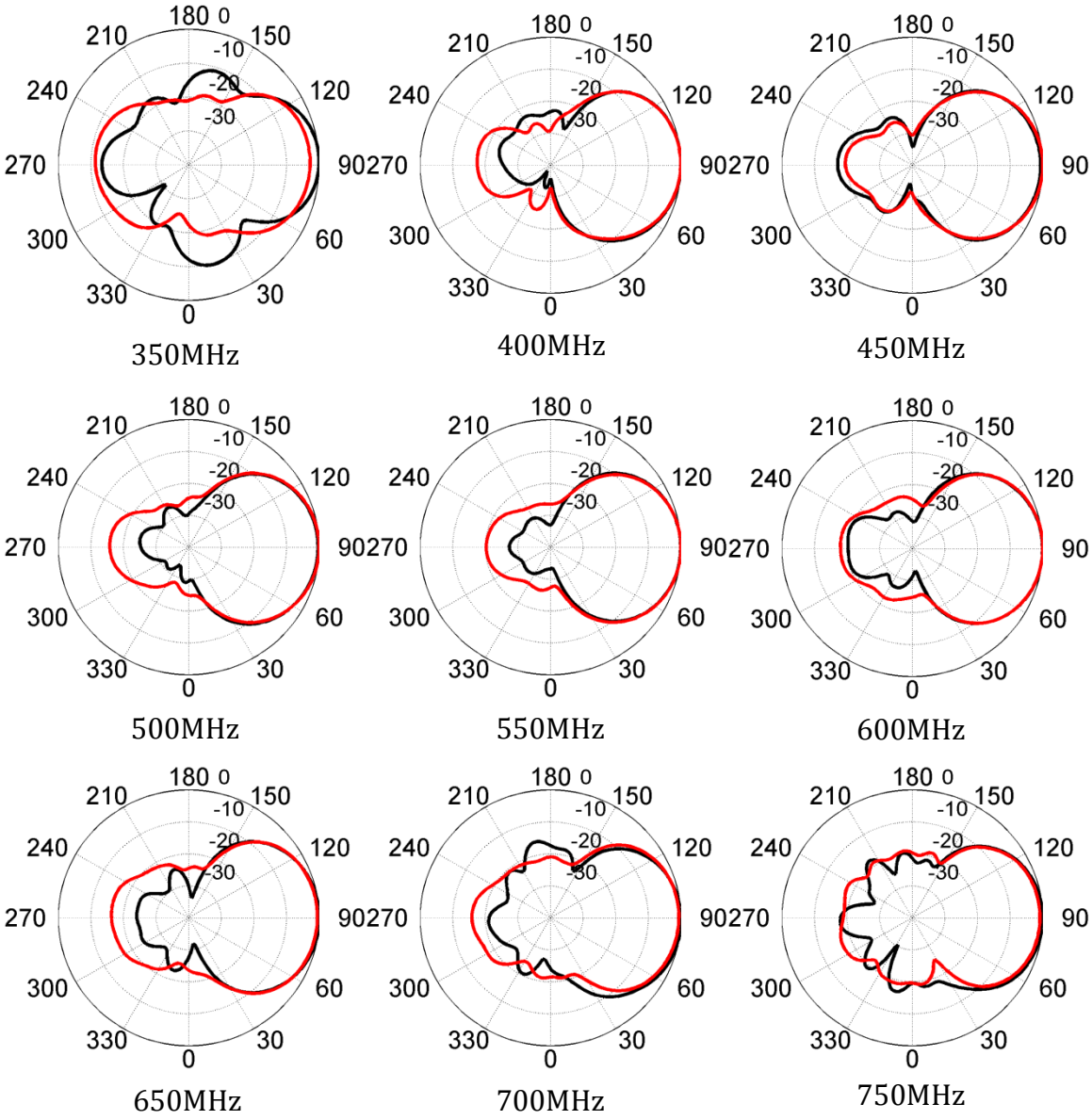

Figure 3.10 Computed normalized patterns of the UHF LPDA in the azimuth plane (xy-plane or theta = 90o). Two cases: black trace representing Case 1 (Cable parameters: a=7.5 mm, b=2 mm, εr=2.2, c=6.7 mm; H = 10mm; S = 2.5mm) and the red trace representing Case 2 (Cable parameters: a=11 mm, b=3 mm, εr=2.2, c=10.4 mm; H = 25.4mm; S = 3.4mm). In both cases εr1=1.0 and thus no dielectric substrate present.

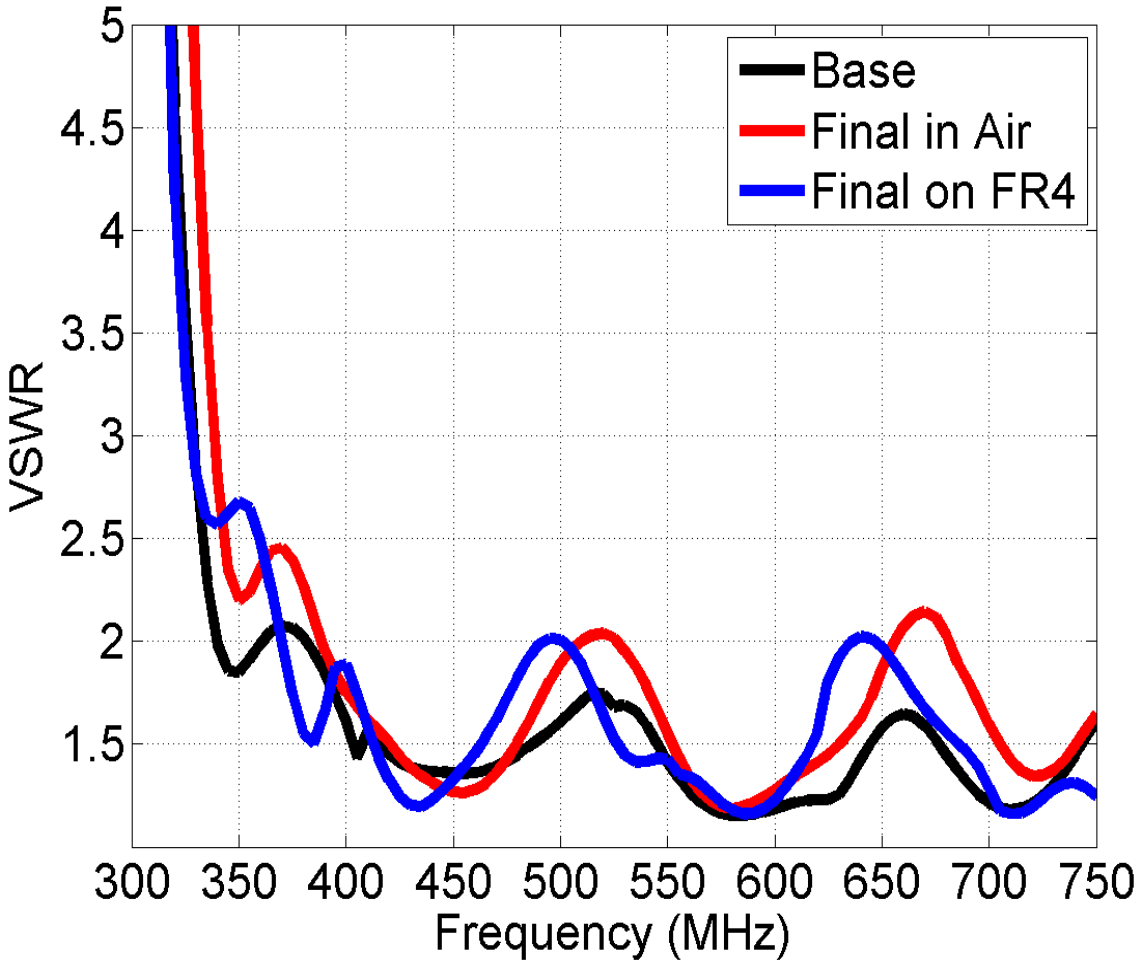

Figure 3.11 Simulated VSWR results of the LPDA considering three cases: black trace representing the Baseline LPDA (cable parameters: a=7.5 mm, b=2 mm, εr=2.2, c=6.7 mm; H = 10mm; S = 2.5mm), the red trace represent the adjusted LPDA to meet commercial manufacturing trace width limits and tolerances, and finally the blue trace represent the adjusted LPDA on thin 1.58 mm FR4 layers. In the latter two cases (a=11 mm, b=3 mm, εr=2.2, c=10.4 mm; H = 25.4mm; S = 3.4 mm).

Since the performance of the LPDA with the two layers being separated by a distance, H=25.4 mm was found to be satisfactory that design was considered for future fabrication and characterization. Further considerations were to explore the prospect of fabricating the array using a direct printing technique through a commercial manufacturer [39].

The commercial manufacturer spray prints antenna apertures and transmission lines using their proprietary techniques where they have specific dimensional limits and tolerances. Such as trace widths have to be within certain standard sizes or custom trace widths with small variations may become rather expensive. Based on those available trace width dimensions and the tolerances the UHF LPDA design was further adjusted to maintain performance in the 350-750 MHz frequency band. Those dimensions are only slightly different from the ones listed in Table 3.1 and hence are not listed here for the sake of brevity. Also since the array will be fabricated on dielectric substrate materials the effect of dielectrics was also investigated. These results are shown in Figure 3.11 which shows the VSWR data of the baseline design (original LPDA), adjusted LPDA to fit commercial manufacturing trace width limits and tolerances, and the final adjusted LPDA on thin FR substrate layers. For the latter two cases H=25.4 mm and S=3.4 mm while for the Baseline case H=10 mm and S=2.5 mm. It is clear that the final design with the adjusted dimensions and on FR4 operates satisfactorily within the 350-700 MHz bandwidth. The VSWR peaks are higher than the baseline design but are still satisfactory.

Table 3.4 Computed peak realized gain (dBi) and F/B (dB) of the final adjusted dimensions LPDA on thin FR4 layers.

Frequency (MHz)	350	400	450	500	550	600	650	700	750
Array realized gain (dBi) for final LPDA on FR4	6.2	7.8	9.0	8.4	8.7	8.6	7.0	7.8	7.1
Array F/B (dB) for final LPDA on FR4	5.3	12.2	18.3	19.1	19.1	17.7	15.2	11.2	15.6

Computed peak realized gain (dBi) and the F/B (dB) of the final LPDA with adjusted dimensions and on thin FR4 substrates are listed in Table 3.4. The gain varies between 6.2-9 dBi while the F/B varies between 5.3-19.1 dB.

3.3 EXPERIMENTAL FABRICATION AND CHARACTERIZATION

The proposed UHF LPDA was fabricated in-house at the University of South Carolina (USC) Microwave Engineering Laboratory (MEL) by photochemical etching. Since the complete array was about 3 ft long and 1 foot wide it was not possible to etch such a large aperture using our existing facilities. Instead for each layer 12 inch by 12 inch 1.58 mm thick FR4 substrates were used to build the whole array. The two layers were separated from each other using plastic screws that were placed away from the conducting elements of the array. The array was fed using a 11 mm diameter coaxial cable (LMR 600 cable from Times Microwaves) [40] and a conducting copper tube. The outer insulation of the LMR 600 cable was removed in order to connect the antenna elements to the outer shield of the coax. Photographs of the fabricated array are shown in Figure 3.12.

Measured VSWR results of the fabricated LPDA are plotted in Figure 3.13, which show that the array operates from 350-750 MHz. The VSWR shows a slightly higher peak between 450-500 MHz which is because of the difficulty in maintaining the S=3.4 mm distance between the outer surface of the coax and the tube that was maintained in the simulation models. It is expected that in practical manufacturing more precise distance control will be feasible either through better fixturing or through the use of constant thickness low dielectric constant insulating material. Array radiation patterns and gain were measured in a Satimo chamber at the Wireless Research Center of North Carolina (WRCNC) [40]. Measured realized gain results are shown in Figure 3.14. It is clear that for much of the frequency range the peak array gain is greater than 7 dBi. Only

within a narrow frequency range the array gain is near 6 dBi. The array gain bandwidth extends from 350-750 MHz.

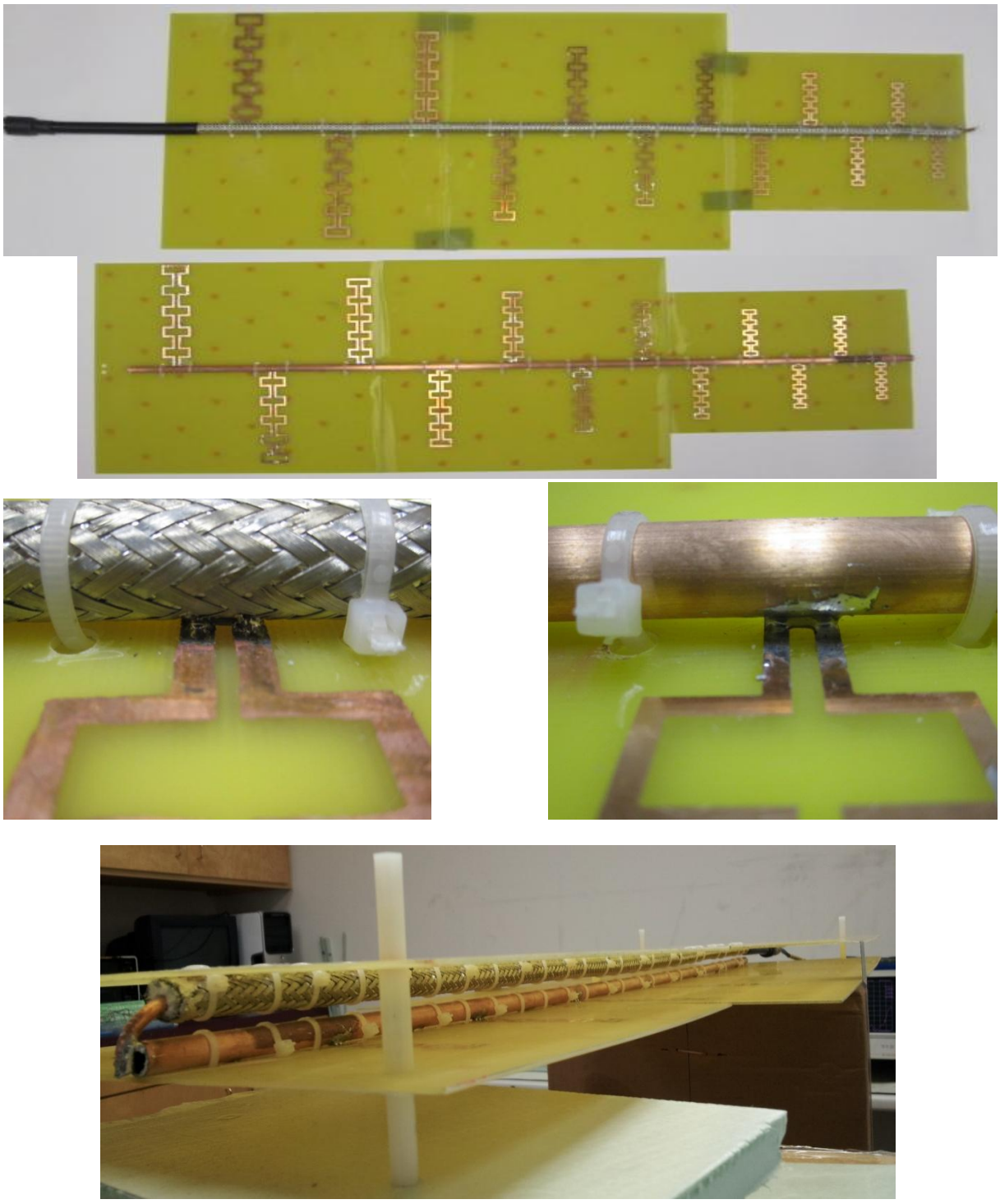

Figure 3.12 Photographs of the fabricated LPDA.

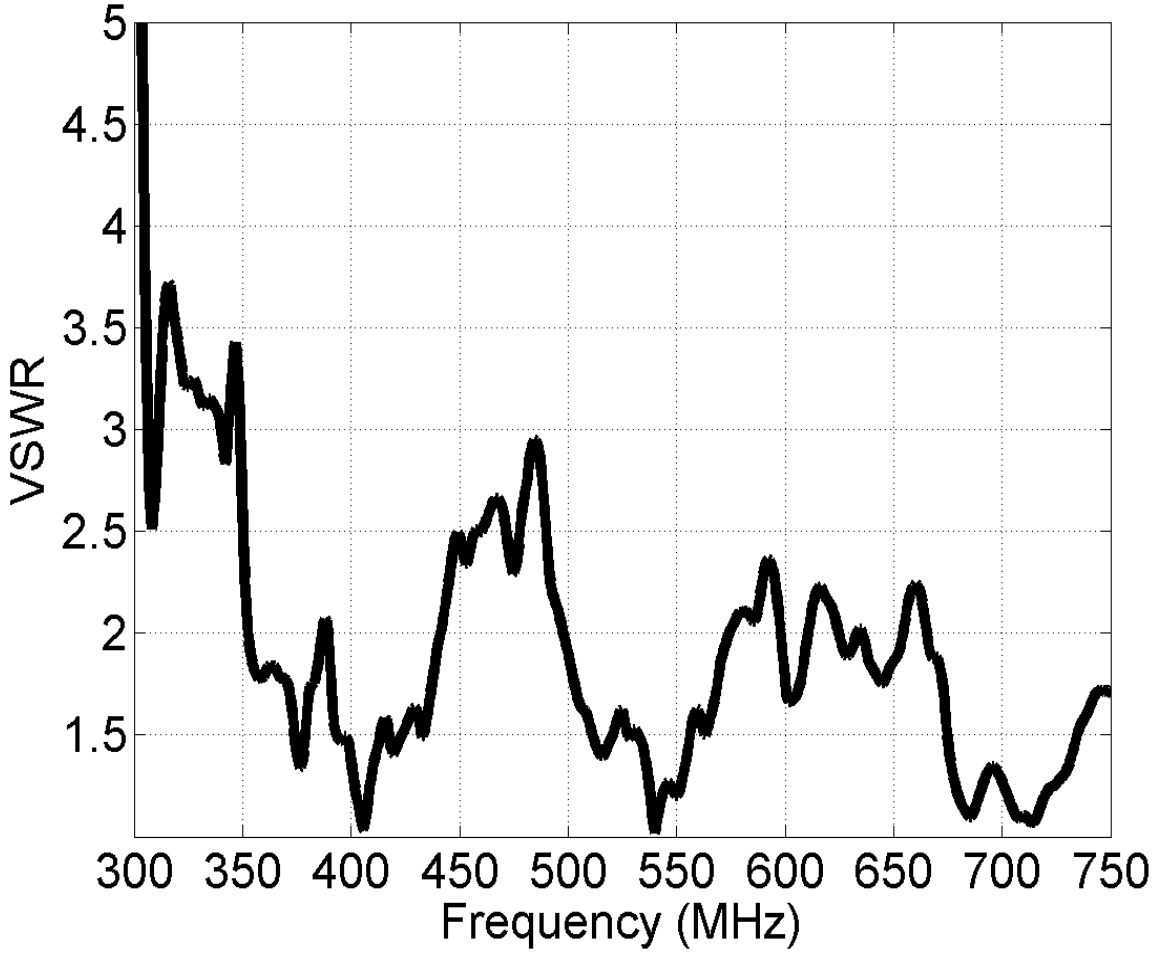

Figure 3.13 Measured VSWR of the UHF LPDA shown in Figure 3.12.

Measured normalized radiation patterns of the UHF LPDA shown in the photographs of Figure 3.12 are shown in Figure 3.15 and Figure 3.16. The elevation plane patterns show directional beams with Half-Power Beamwidths (HPBW) in the range of 114 to 72 degrees while the azimuth plane patterns show HPBWs in the range of 72 to 54 degrees. The F/B ratio ranges between 10-22 dB with an average F/B of 15 dB. Thus the experimental results clearly show a much higher F/B than the simulation results.

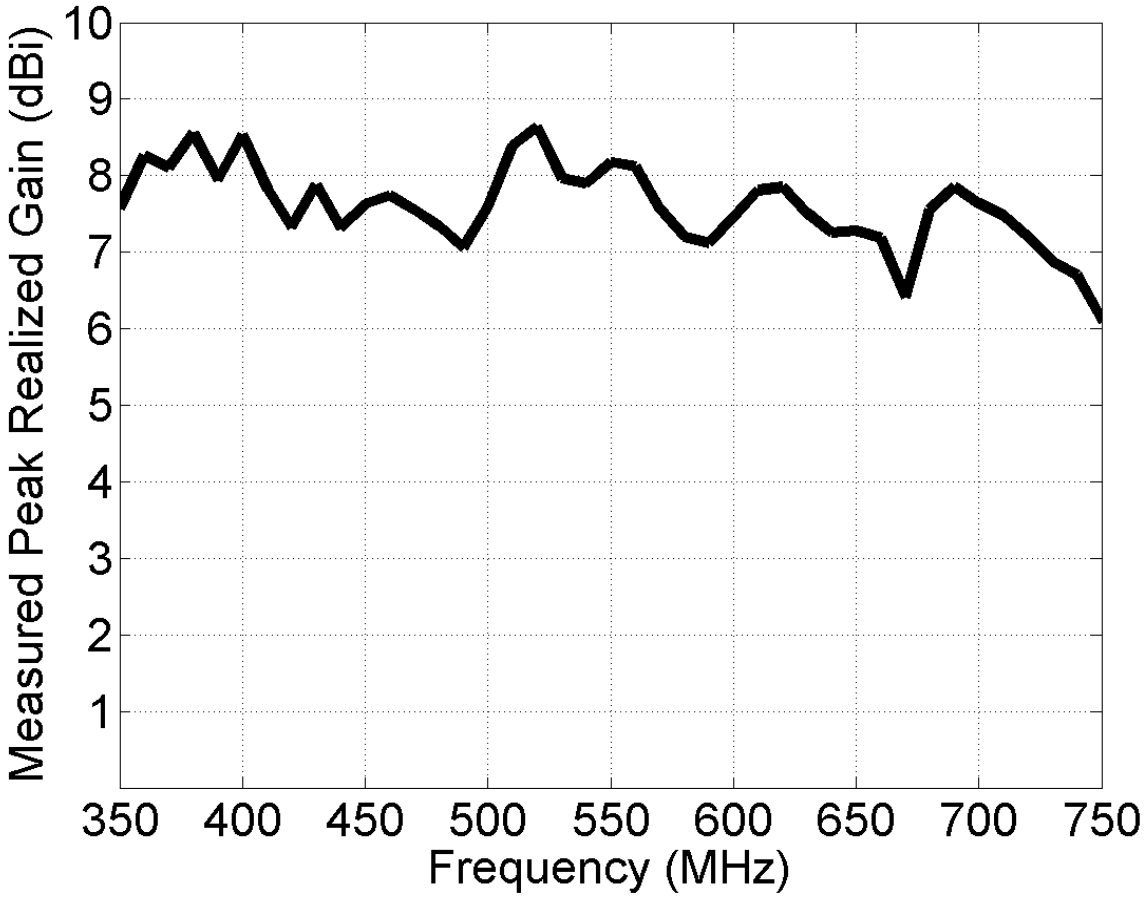

Figure 3.14 Measured peak realized gain of the UHF LPDA shown in Figure 3.13.

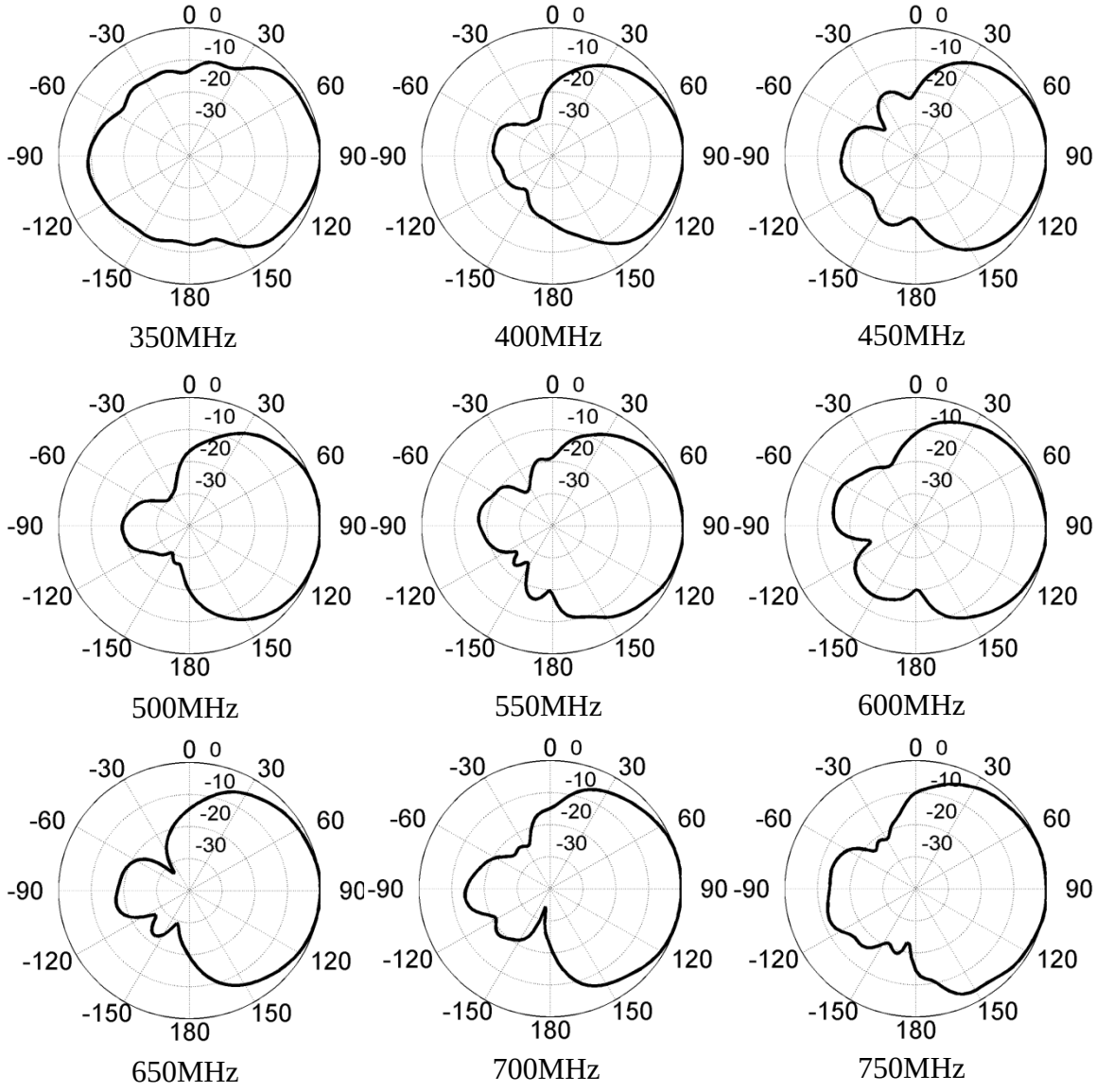

Figure 3.15 Measured normalized Elevation Plane (phi = 90^{o}) patterns of the UHF LPDA shown in Figure 3.12.

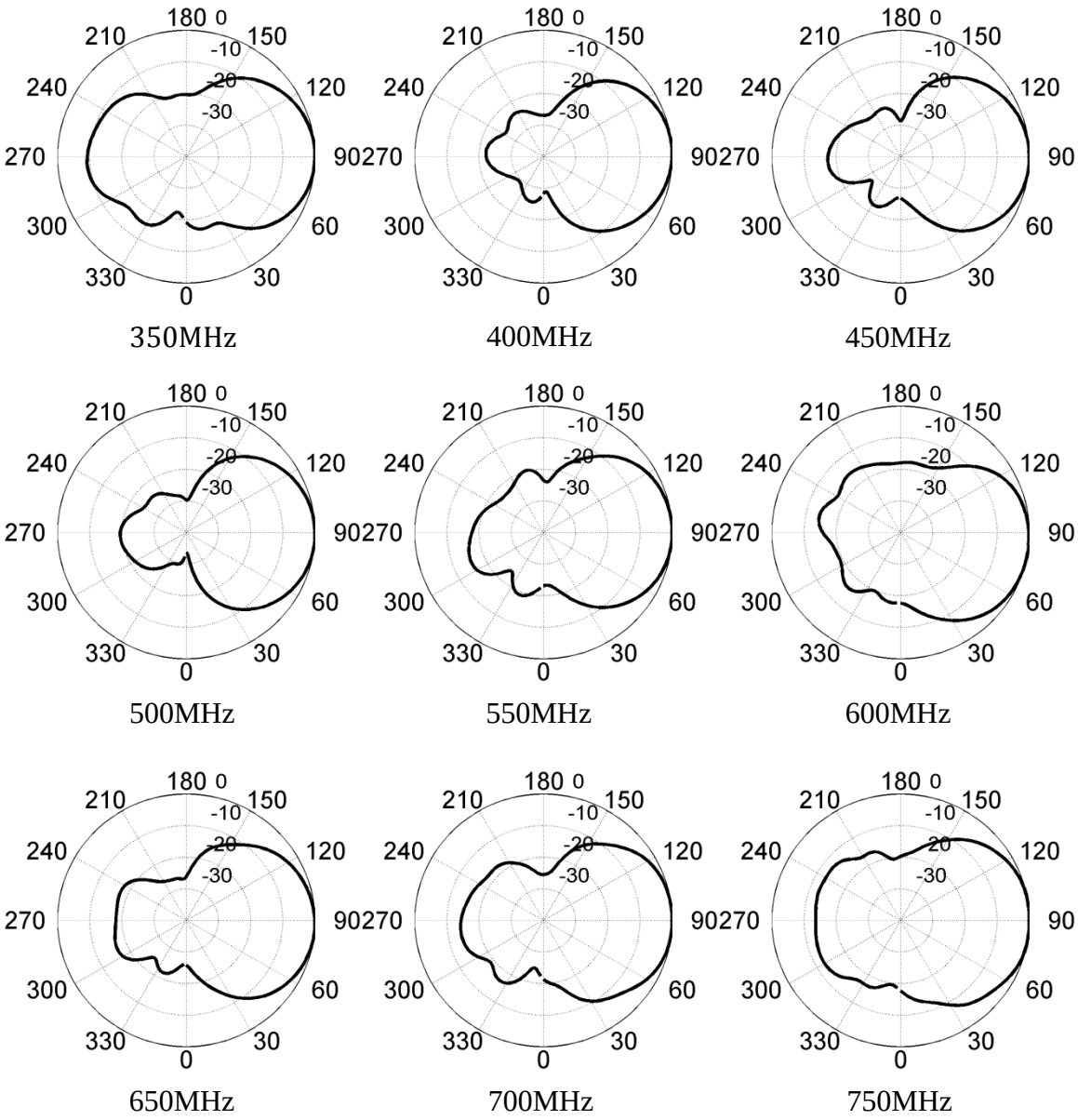

Figure 3.16 Measured normalized azimuth plane (theta = 90^{o}) patterns of the UHF LPDA shown in Figure 3.12.

3.4 EFFECTS OF DIELECTRIC SUPPORT MEMBER ON ARRAY PERFORMANCE

Further simulations of the array were performed considering the presence of a long 'Dielectric Support Member.' The location, geometry, and dimensions of the support member are shown in Figure 3.17. We needed to investigate what type of material will be the least bit intrusive in terms of antenna performance while providing mechanical support. The use of graphite was ruled out because it will almost certainly adversely affect the array performance. Thus the choice was to design the support member using one or more dielectric materials. Initial simulations were performed where the entire support member consisted of one type of material while later on two different materials were considered to model the support member.

The square cross section dielectric support member has a width, W_{sm} of 25.4mm and a wall thickness, T_{sm} of 6.4mm. The nearest side wall of the support member is D_{sm}=25.4mm from the feed center as shown in Figure 3.17. The parameters of the baseline LPDA design that was fabricated and tested before was used in these simulations. As seen in Figure 3.18 adding a glass support member significantly deteriorates the VSWR performance of the array but having a PTFE support member has less of a severe effects on the VSWR characteristics. Although the results shown in Figure 3.18 clearly indicate that the use of low dielectric constant material as the support member is preferable that may not be sufficient as a support member. Investigations were carried out to see if considering glass as the support member yet reducing the length, L was an option.

Figure 3.19 shows these results.

Clearly if L can be 10 inches or shorter then glass as a support member will result in acceptable performance. Obviously any reduction in the dielectric constant of the material of the support member will further aid the VSWR performance. Further simulations were performed considering FR4 as the dielectric support member and in the presence of a reinforcing graphite support member just behind the LPDA as shown in Figure 3.20.

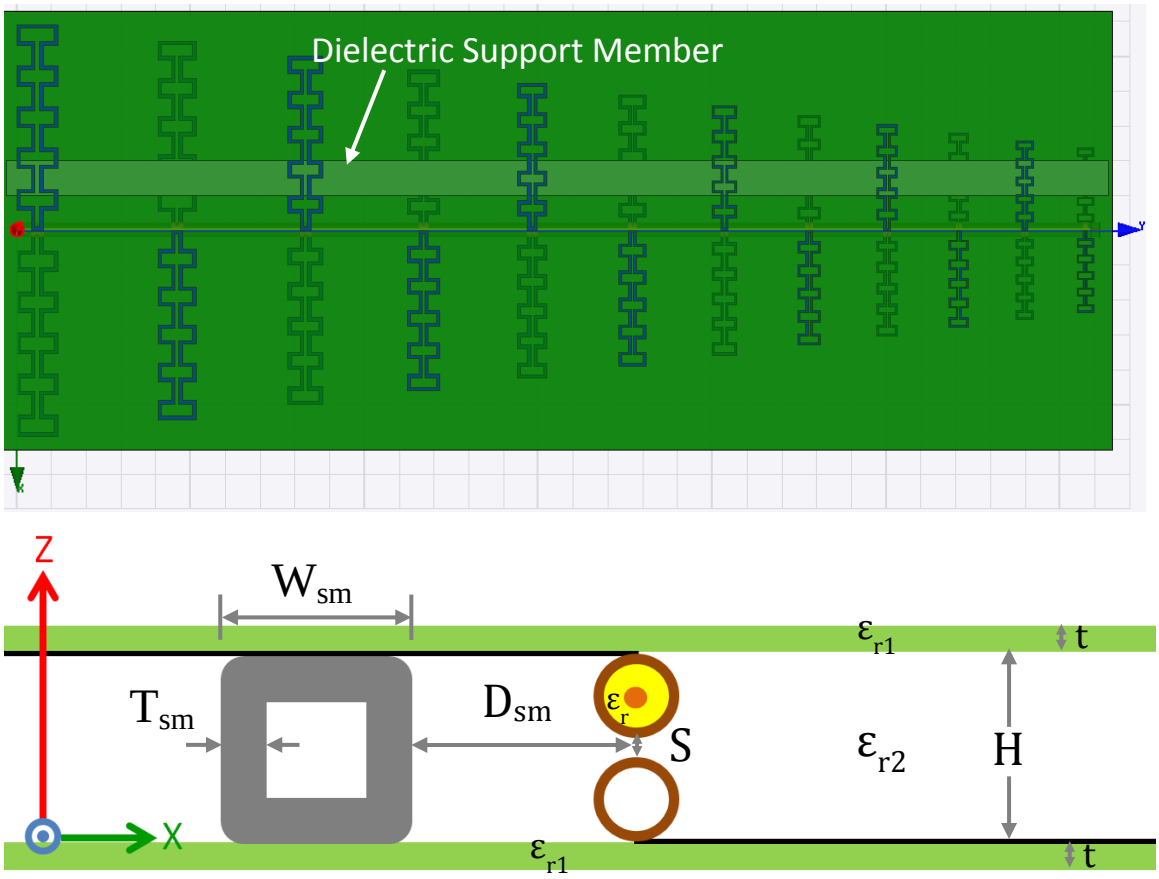

Figure 3.17 Array simulation model illustrating the presence of a 'Dielectric Support Member'; H=25.4 mm, S=3.4 mm, length of dielectric support member=31 inches

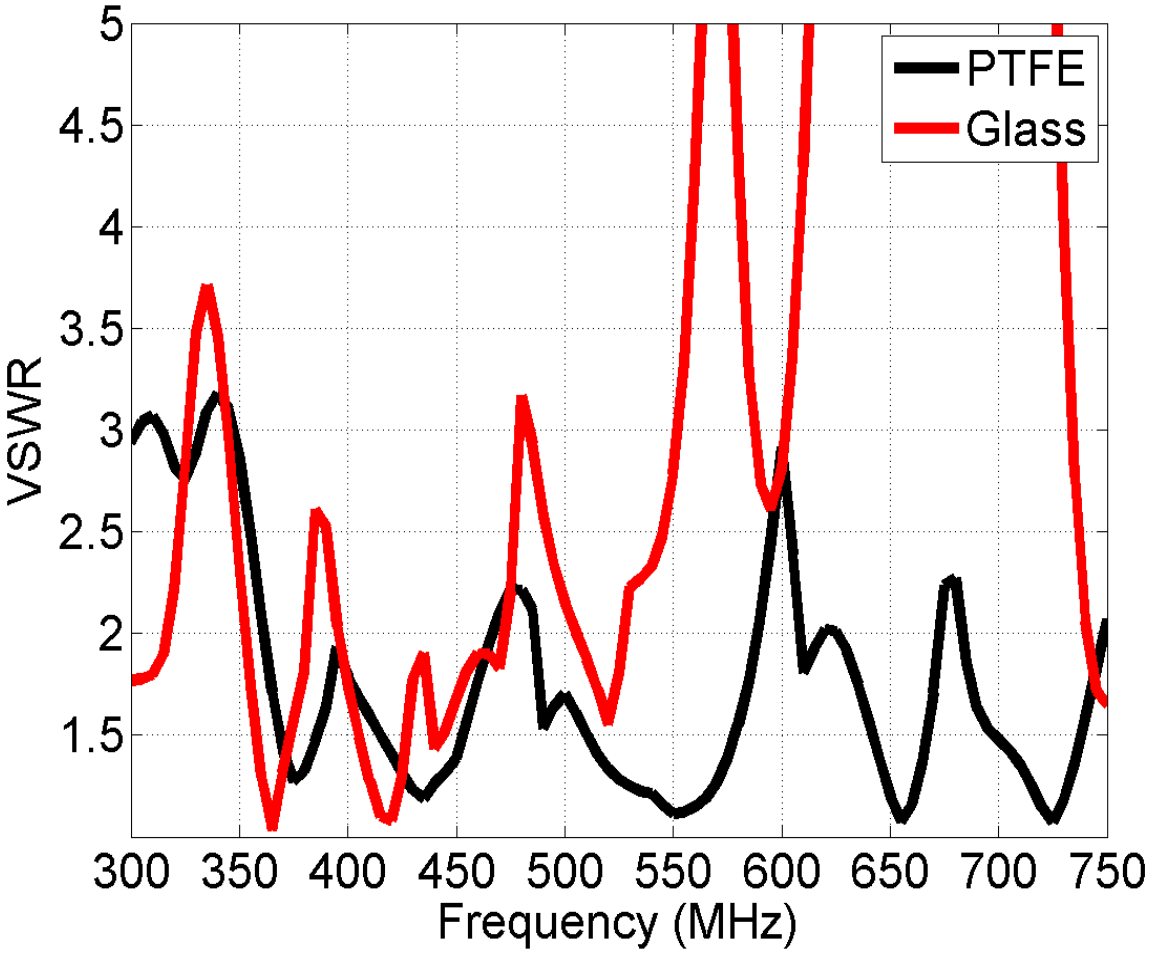

Figure 3.18 Simulated VSWR versus frequency characteristics of the array in the presence of the dielectric support member (31 inches long); PTFE (εr=2.2) and Glass (εr=5.5) were considered to be the material of choice.

The graphite support member is a solid structure with a width of 30.5mm, height of 25.4mm and a length of 254mm. The graphite support member is 59.5 mm from the center of the first element. Simulations were done to insure that the presence of a significantly large conductive material near the low frequency element would not cause low frequency distortion in the VSWR bandwidth. The results of the parametric simulation considering various lengths of the FR4 dielectric support member with the presence of the graphite support member are shown in

Figure 3.21.

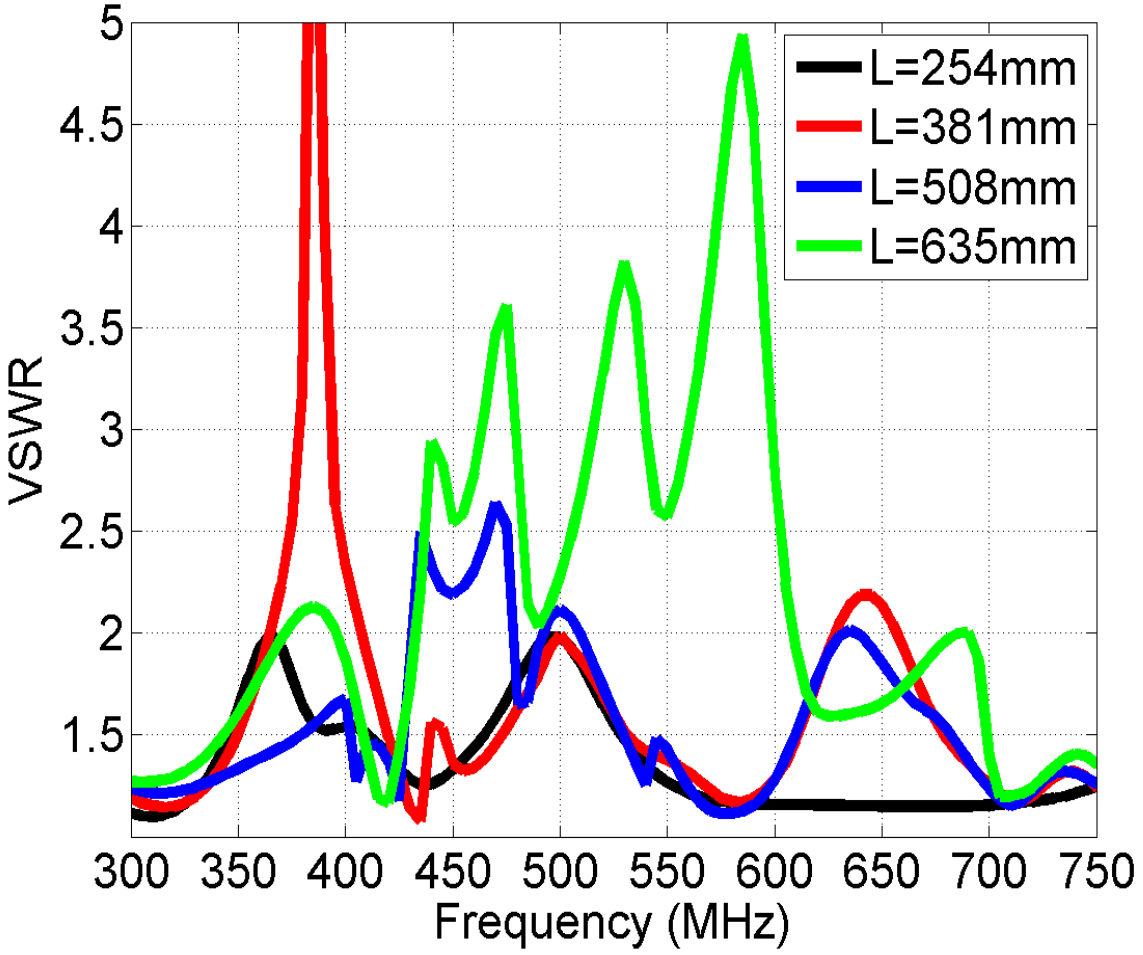

Figure 3.19 Simulated VSWR versus frequency characteristics of the array in the presence of the dielectric support member (Glass) with variable length.

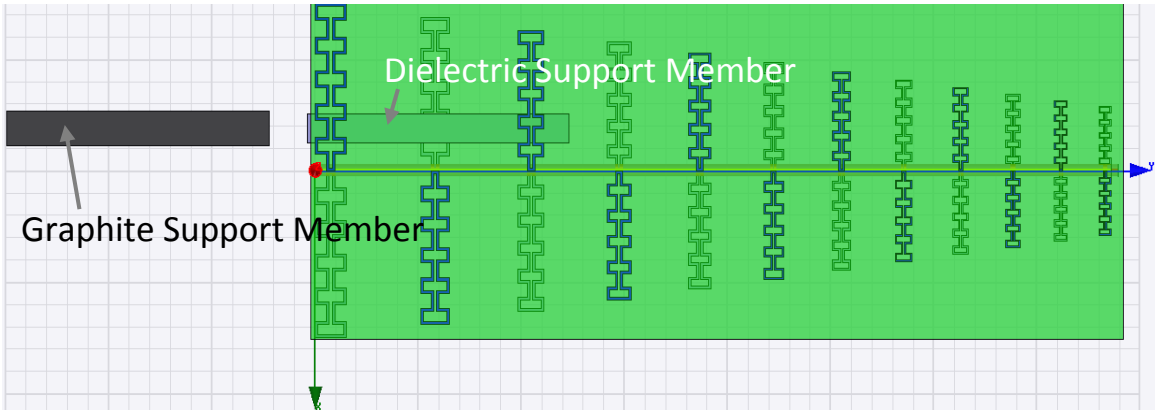

Figure 3.20 Simulation model showing the effect of various support members.

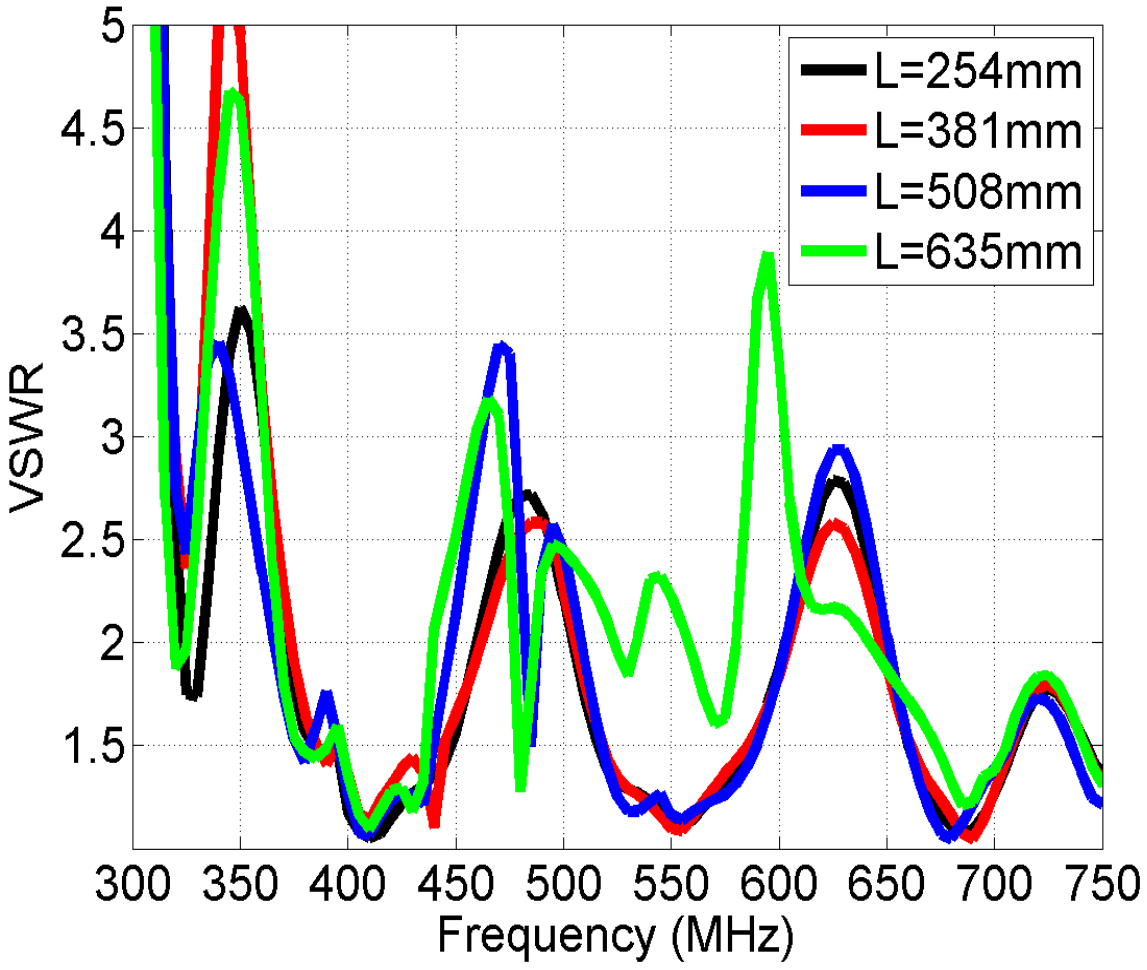

Figure 3.21 Simulated VSWR versus frequency results in the presence of 254mm long graphite and FR4 dielectric support members.

Although FR4 has a lower dielectric constant than glass, the presence of the graphite support member further deteriorates the VSWR performance. However, comparing the results between the 254mm long dielectric support member cases shown in Figure 3.19 and Figure 3.20 we observe that there is an increase in the VSWR below 325 MHz which is not in our desired frequency band but there is also an increase at 350, 475, and 625 MHz which is inside our desired frequency bandwidth. A VSWR

comparison of the baseline design and the LPDA with the 254mm long dielectric and graphite support member is shown in Figure 3.22**.**

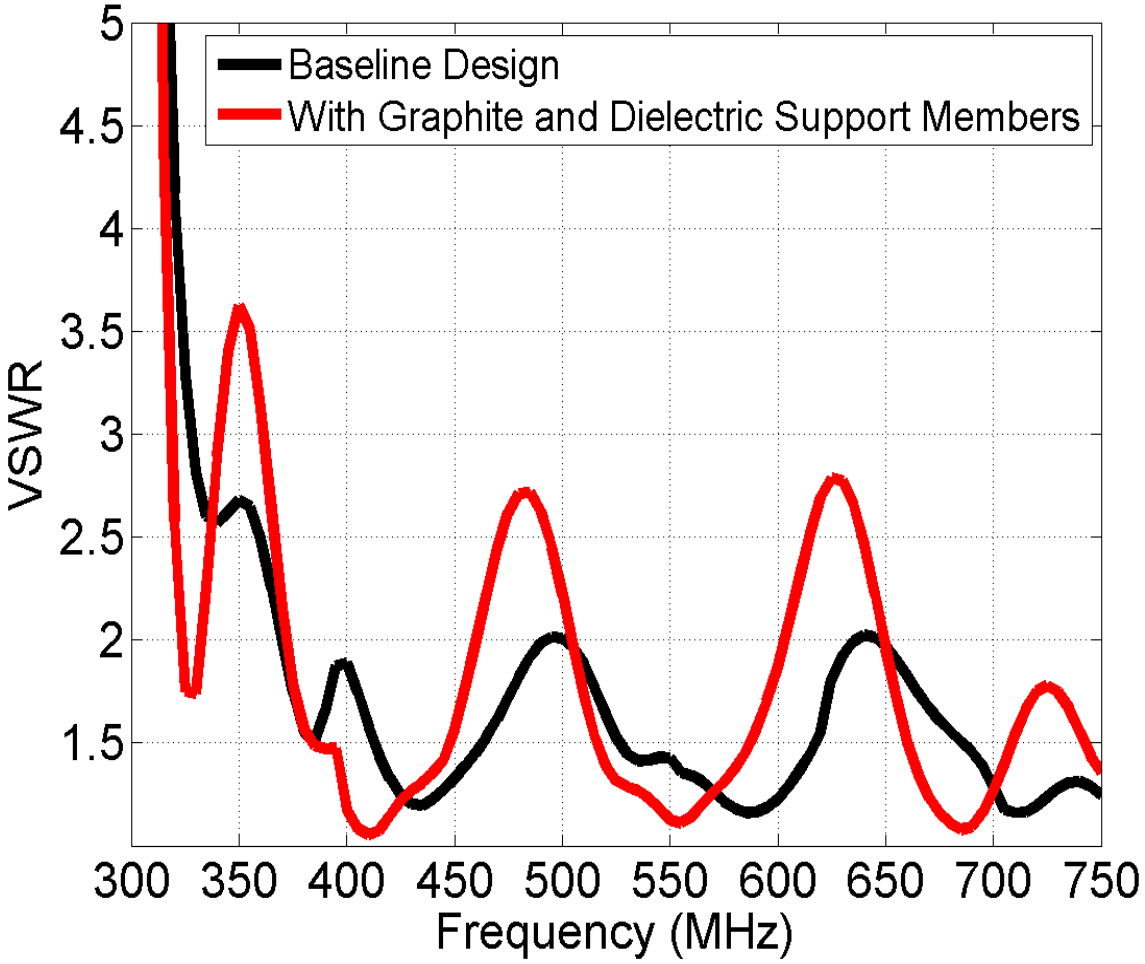

Figure 3.22 Comparison between the simulated VSWR versus frequency results in the presence of graphite and FR4 dielectric support members and those of the baseline design.

As can be seen in Figure 3.22 the baseline design has a VSWR of 2 or below throughout most of the bandwidth except around 350MHz, the LPDA with the graphite and dielectric support member has a VSWR of 2.7 or below except around 350MHz. Table 3.5 below compares the LPDA boresight total realized gains at 50MHz intervals.

Table 3.5 Comparison between the peak realized gain.

Frequency (MHz)	350	450	550	650	750
Realized Gain Baseline Design (dBi)	9.2	7.8	8.7	6.8	7.1
Realized gain with graphite and dielectric support members	7.7	8.1	8.5	7.3	7.1

3.5 Effects of Cable and Tube Asymmetry on Array Performance

Further simulations were performed considering a coaxial cable and a tube with different diameters. A smaller coax and a larger tube (made of thin walls) would reduce the total weight of the array because of the reduced diameter of the solid inner conductor of the coax. Such a case is illustrated Figure 3.23. There were no dielectric support members present and the antenna bi-layers were placed on thin FR4 substrates.

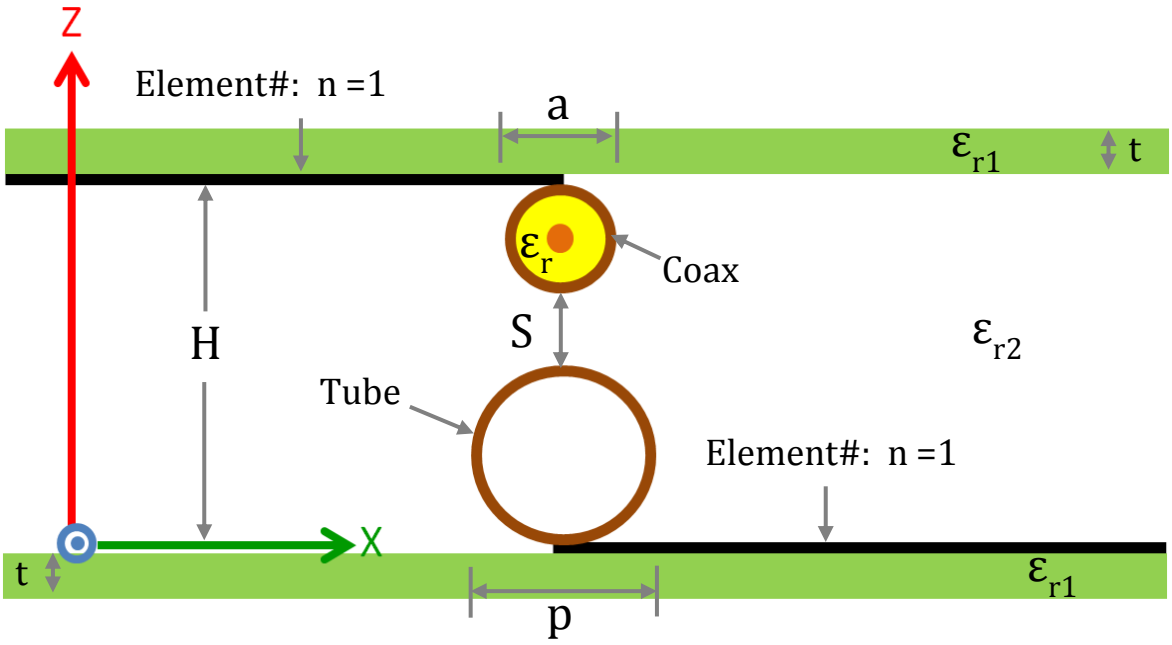

Figure 3.23 Asymmetric coax and conducting tube scenarios.

As seen the tube has an outer diameter of *p* while the coax has an outer diameter of *a*. A series of simulations was performed as function of a, p, and S where H was kept

constant. The various Test cases studied are listed in Table 3.6. The results of these simulations are shown in Figure 3.24. It is clear that for most cases the VSWR data are very poor except for Test 2. Test 1 has by far the worst VSWR which represents a very small diameter cable and a large diameter tube and thus a tube diameter to coax diameter ratio, R of 4.9. Tests 3 and 4 also result in high VSWR. Test 2 on the other hand (R=1.8)

Table 3.6 Coax and tube diameter variation study.

Cases	Tube outer dia, p (mm)	Coax Outer dia, a (mm)	Diameter ratio, R	Separation, S (mm)
Test 1	18.3	3.7	4.9	3.4
Test 2	14.4	8	1.8	3
Test3	17.2	5.7	3	2.5
Test4	16.95	5.45	3.1	3

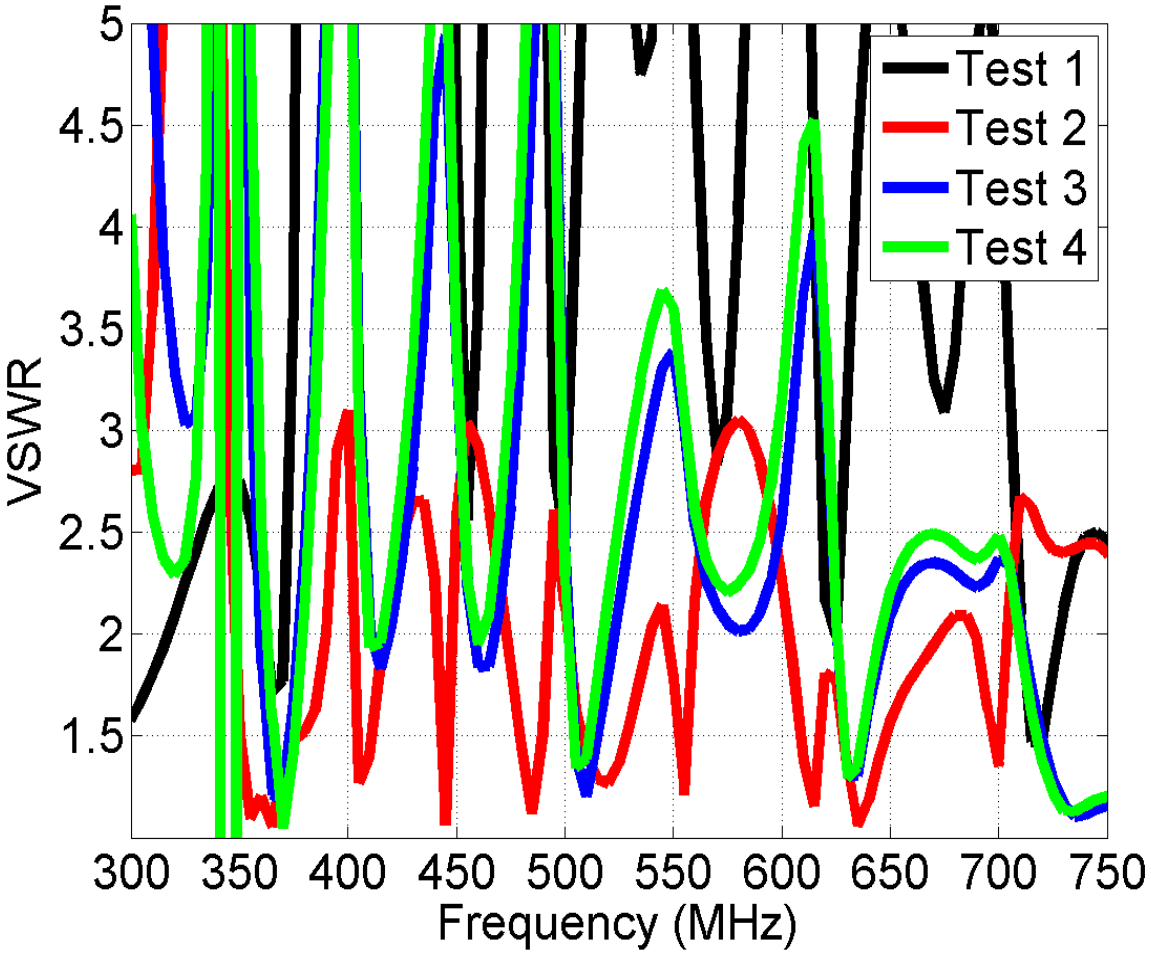

Figure 3.24 Simulated VSWR Vs frequency for various Test cases consisting of asymmetric cables and conducting tubes.

shows that the VSWR may be manageable by doing further tuning optimization. Based on these observations it was concluded that the highest asymmetry, R that can be tolerated is around 3 and the separation, S should be reduced as much as possible. Therefore, further simulations were focused on R<3 and S<4 mm.

The cases considered are listed in Table 3.7and the results are plotted in Figure 3.25. Comparison of the VSWR between all the cases listed in Table 3.7 and the baseline

results it is clear that Case 2 has reasonable performance. Further VSWR optimization should focus on reducing R below 2.5.

Table 3.7 Coax and tube diameter variation study. Case 1 is 'Test2' in Table 5.6.

Cases	Tube outer dia, p (mm)	Coax Outer dia, a (mm)	Diameter ratio, R	Separation, S (mm)
Baseline	11	11	1	3.4
Case 1	**14.4**	**8**	**1.8**	**3**
Case 2	18.2	6.7	2.7	0.5
Case 3	17.95	6.45	2.8	0.1

Finally, the computed realized gain data for a few selected cases studied before are listed in **Error! Reference source not found.**. As seen the realized gain data for the baseline array and the array with dielectric support members compare well. Gain is lower for the array with asymmetric cable and tube as can be seen in rows 4 and 5 of **Error! Reference source not found.**.

Table 3.8 Comparison between the peak realized gain.

Frequency (MHz)	350	450	550	650	750
Realized Gain Baseline Design (dBi)	9.2	7.8	8.7	6.8	7.1
Realized gain with graphite and dielectric support members	7.7	8.1	8.5	7.3	7.1
Test 2 defined in Table VI	--	5.0	6.9	7.4	5.8
Case 2 defined in Table VII	7.9	3.7	7.3	7.3	7.5

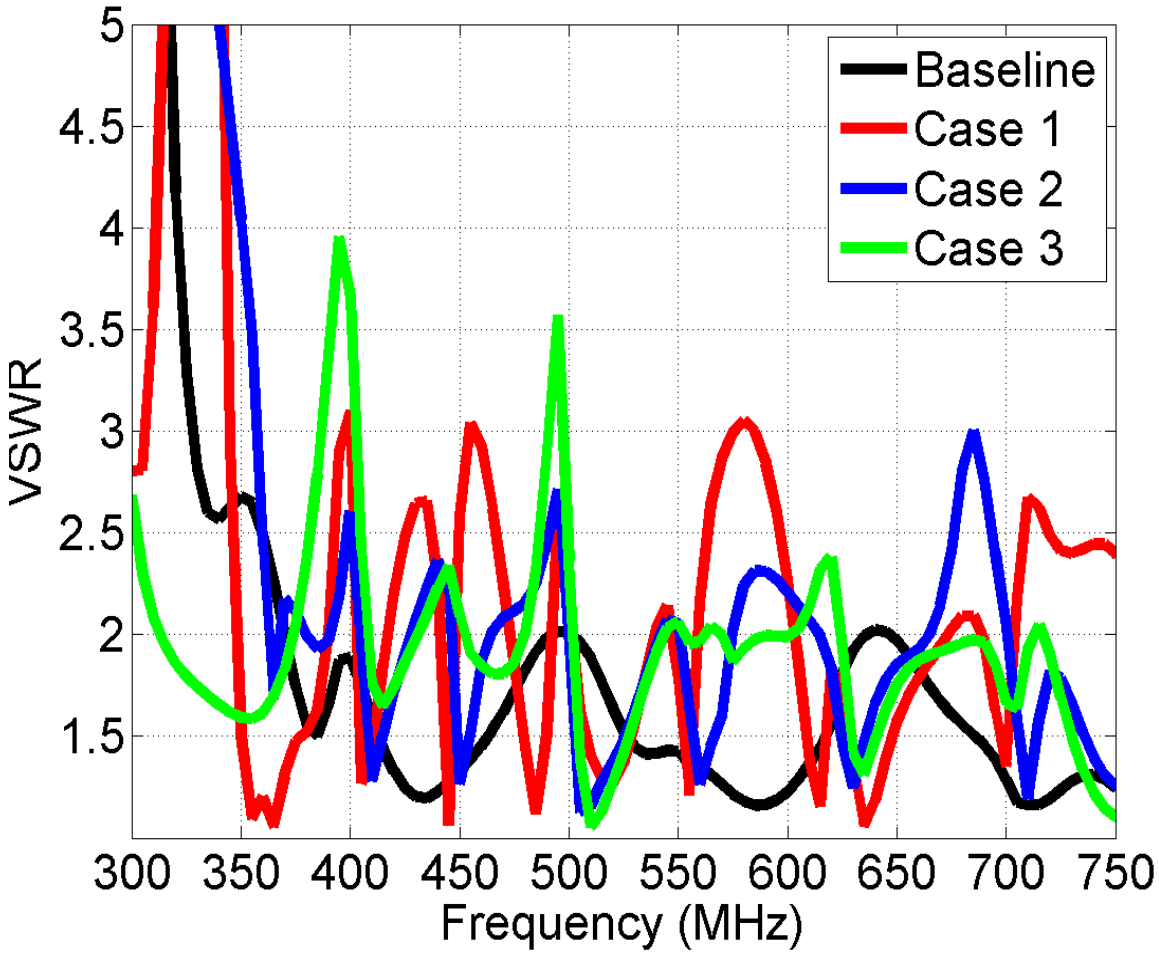

Figure 3.25 Simulated VSWR Vs frequency for various Test cases consisting of asymmetric cables and conducting tubes.

CHAPTER 4

MEMS RECONFIGURABLE APERTURE COUPLED PIXEL ANTENNA STRUCTURES

In the literature there has been considerable efforts placed on reconfigurable antennas. DARPA sponsored the RECAP program in the 1990s where researchers at the Gerogia Tech. Research Institute (GTRI) worked on reconfiguring elements of metal patches to form broadside and endfire patterns [41]. They used semiconductor switches to demonstrate their concepts. In [42]-[43] the authors used MEMs switches to reconfigure small spiral and microstrip patches. In [44] the authors have used PIN diode switches to reconfigure a stacked microstrip patch antenna for operation in two frequency bands resulting in broadside and endfire beams. Lately in [45] a vertical monopole antenna consisting of metal patch pixels were reconfigured using MEMs switches. In [46] the authors have demonstrated the use of PIN diode switches to reconfigure a Yagi-Uda antenna. A Sierpinski gasket antenna was reconfigured using switches by Anagnostou *et al.* [47]. Febo [48] has done studies on MEMs switch integration to reconfigure several antenna geometries.

The goal of our work is to integrate MEMs switches to develop state of the art reconfigurable pixel patch antenna structures. After reviewing the literature we came to the conclusions that the surface mountable MEMs switch offered by Omron Corporation in Japan is too expensive ($200/piece) and has a larger footprint.

In contrast, the Radant MEMs switch which has been used in [43]-[44] and [48] has a very small footprint (1.4 mm by 1.4 mm) and very low insertion loss (0.1 dB) and high isolation (20 dB or higher). The only disadvantage of the Radant MEMs switch is that it has to be wire bonded to the antenna and circuit layouts [49]. This calls for gold plating the antenna and the circuit.

4.1 ANTENNA CONFIGURATION

4.1.1 MEMs Reconfigured Probe-Fed Pixel Patch antenna

A four by four microstrip patch pixel antenna system was designed and fabricated as shown in Figure 4.1. The conductive pixels were etched on 1.5 mm thick RO4003 substrate. There were 4 MEMs switches (RMSW101) placed between the two top rows of pixels. Similarly there were four MEMS switches placed between the two bottom rows of pixels. Each pixel was a 7 mm by 7 mm square separated by a distance of 2 mm in order to place the MEMs switch. In between pixels, where there were no switches (those spaces were filled using conducting strips with dimension 2 mm by 2 mm). Thus most of the pixels were connected using a conducting strip representing an ideal short for a switch that is in the 'ON' state. There were 16 such connections as opposed 8 actual MEMs switches in the geometry shown in Figure 4.1.

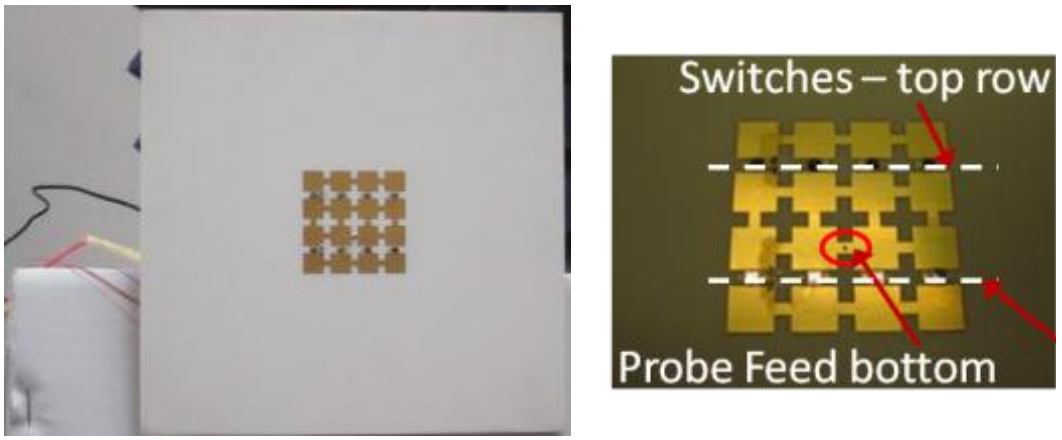

Figure 4.1 There are four switches on the top row and four on the bottom row. Each switch is wire bonded to two adjacent pixels. The gate of the switch is connected to a 90V DC supply through a plated thru hole and a thin wire.

The location of the probe feed is also shown in Figure 4.1. The switches were biased using 40 kΩ resistors. Three cases were studied:

- Case 1 – when all switches were 'on' - the patch antenna operated at the lowest frequency,
- Case 2 – when all switches were 'off' - the patch antenna operated at the highest frequency, and
- Case 3 – when only the top row of switches were 'on' and the bottom row switches were 'off' the antenna operated at an intermediate frequency.

Measured S11 (dB) results of the fabricated antenna are shown in Figure 4.2 As expected when all switches are 'on' the antenna resonates at around 1.5 GHz, when all switches are 'off' the antenna resonates at 3.1 GHz and when only the top row of switches are 'on' and bottom row of switches are 'off' the antenna resonates at an intermediate frequency of 2 GHz. There is a second resonance when all switches are 'on' but that is not of interest to us. It is clear that using MEMs switches a pixel based

microstrip patch antenna can be reconfigured to resonate at multiple frequencies simply by activating and deactivating a set of MEMs switches positioned in different locations of the pixelized geometry.

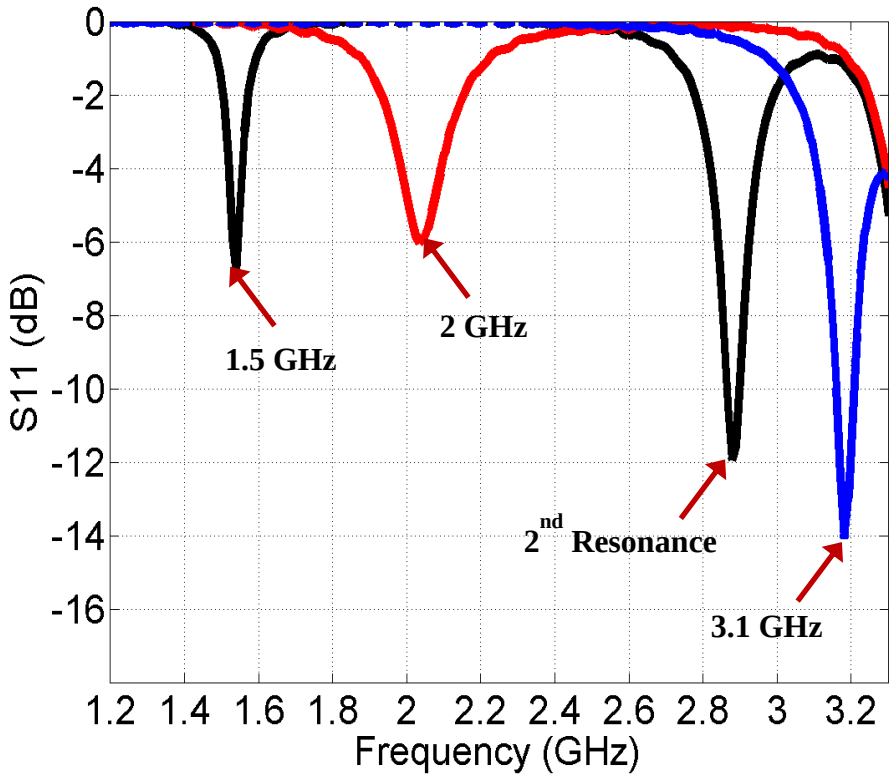

Case 1 - When all 8 switches are on the pixel patch antenna resonates at 1.5 GHz;
Case 2 - when all 8 switches are off it resonates at 3.1 GHz;
Case 3 - when the four top row switches are on and the four bottom row switches are off the antenna resonates at 2 GHz;
No impedance matching was attempted

Figure 4.2 Measured resonance response of the four by four pixel patch antenna.

4.1.2 MEMs Reconfigured Wideband Aperture-Coupled Pixel Patch Antenna

Although from the results shown in Figure 4.2 it is clear that frequency reconfiguration can be easily achieved by activating or deactivating a series of MEMs switches the resonance is rather sharp and the antenna bandwidth is rather narrow. Thus any slight change in the material properties or geometrical deformation will lead to

frequency shift which may render the design not very useful. These concerns led us to focus on investigating wideband aperture coupled pixel patch antennas.

The wideband operation is obtained with the help of increased height and low dielectric constant material. On a conceptual level a scheme shown in Figure 4.3 illustrates such a design. A rectangular grid geometry consisting of M by N pixels reside on a thin dielectric substrate the top and bottom layers of which are defined as Layers L-1 and L-2, respectively. The pixels reside on L-1 while some DC bias traces reside on L-2. A thick low dielectric constant foam material resides underneath substrate 1. The foam contains multiple holes through which the DC bias wires and the DC ground connections are routed. Underneath the foam there is a second dielectric substrate which contains a microstrip feed line on L-6 while its ground is on L-5. The ground contains a slot which couples the RF energy to the pixel patch on L-1. An optional third substrate is placed below substrate 2 which contains a ground plane on L-8. This grounded substrate will allow improved Forward to Backward (F/B) ratio for the pixel patch antenna. Finally, a fourth thin substrate should be considered to be placed on top of substrate 1. This fourth substrate will serve as the radome for the whole aperture.

4.2 APERTURE COUPLED PATCH ANTENNA

Before embarking on the pixel patch design and development using the aperture coupled concept simulations of an aperture coupled patch were performed using HFSS.

4.2.1 Aperture Slot Parameter Simulations

A non-pixelated aperture coupled patch geometry shown in Figure 4.4 was studied first. A microstrip patch with length, L = 51.7 mm and width, W = 73.7 mm was

placed on a 17 mm thick foam material (ε_r = 1.07, tanδ = 0.0009). Underneath the foam aperture coupling was implemented on a 1.58 mm thick RO4003 substrate (ε_r = 3.55 and tanδ = 0.0027). The RO4003 substrate was 201.7 mm long and 223.7 mm wide.

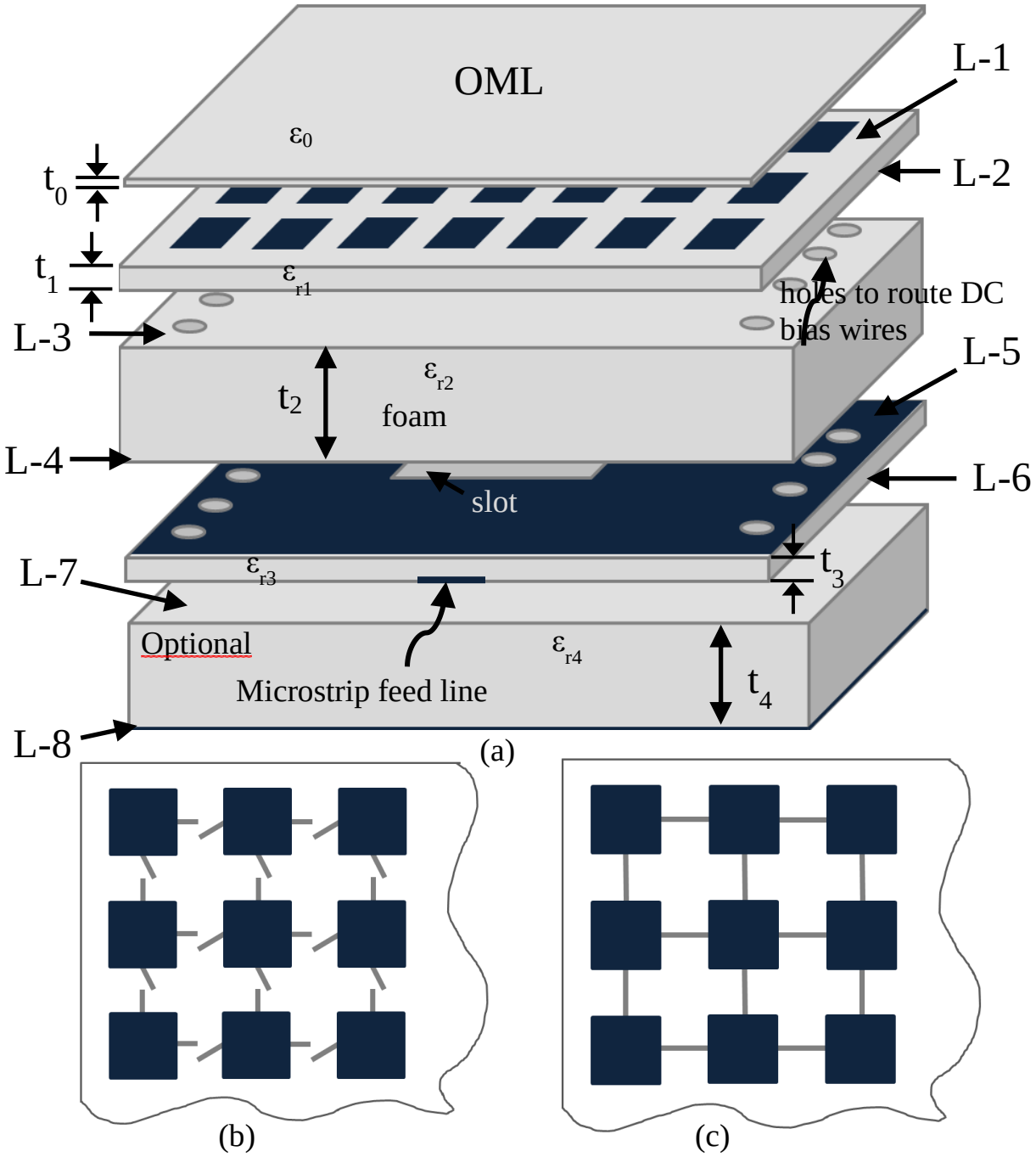

Figure 4.3 (a) Layer layout of pixel patch antenna. t_0 = 1.3mm; t_1 = 0.4mm; t_2 = 16.6mm; t_3 = 1.58mm; (b) open switches and (c) closed switches

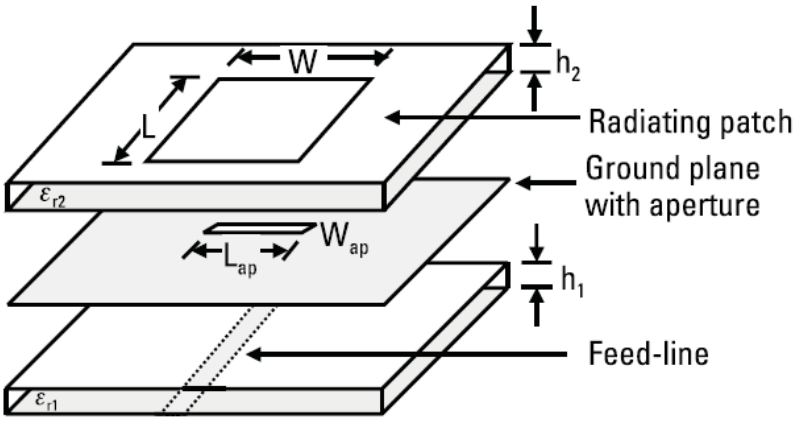

Figure 4.4 Aperture fed patch antenna with various slot lengths; slot widths; stub length [50].

With these dimensions the microstrip patch should resonate at around 2 GHz. The 3.6 mm wide 50Ω microstrip feed line lies on the bottom of the RO4003 substrate. A slot was cut on the substrate ground and its effects on the antenna resonance were studied as shown in Figure 4.5. The slot width, W_{ap} was 1.5 mm and the slot length, L_{ap} was varied from 40-95 mm.

In the S11 versus frequency plot we can clearly see that there are a number of resonances. It is obvious that as the slot length increases the resonant frequency decreases. As the resonant length of the slot deviates farther and farther from the patch resonant length the slot becomes the primary source of the resonance. The resonant frequencies range from 1.15 GHz to 2.05 GHz. The peak antenna gain ranges from 10.4 dBi to 5.9 dBi with the low gain occurring at the lower frequencies. The F/B ranges from 17.7 dB to 4.5 dB and follows the same trend as the gain. The -10 dB S11 bandwidth with a 45 mm long slot is 21.5%. These simulations show that the slot length has a major role in determining the antenna operating frequency. Wide bandwidth and gain are achieved when the patch and slot resonances complement each other.

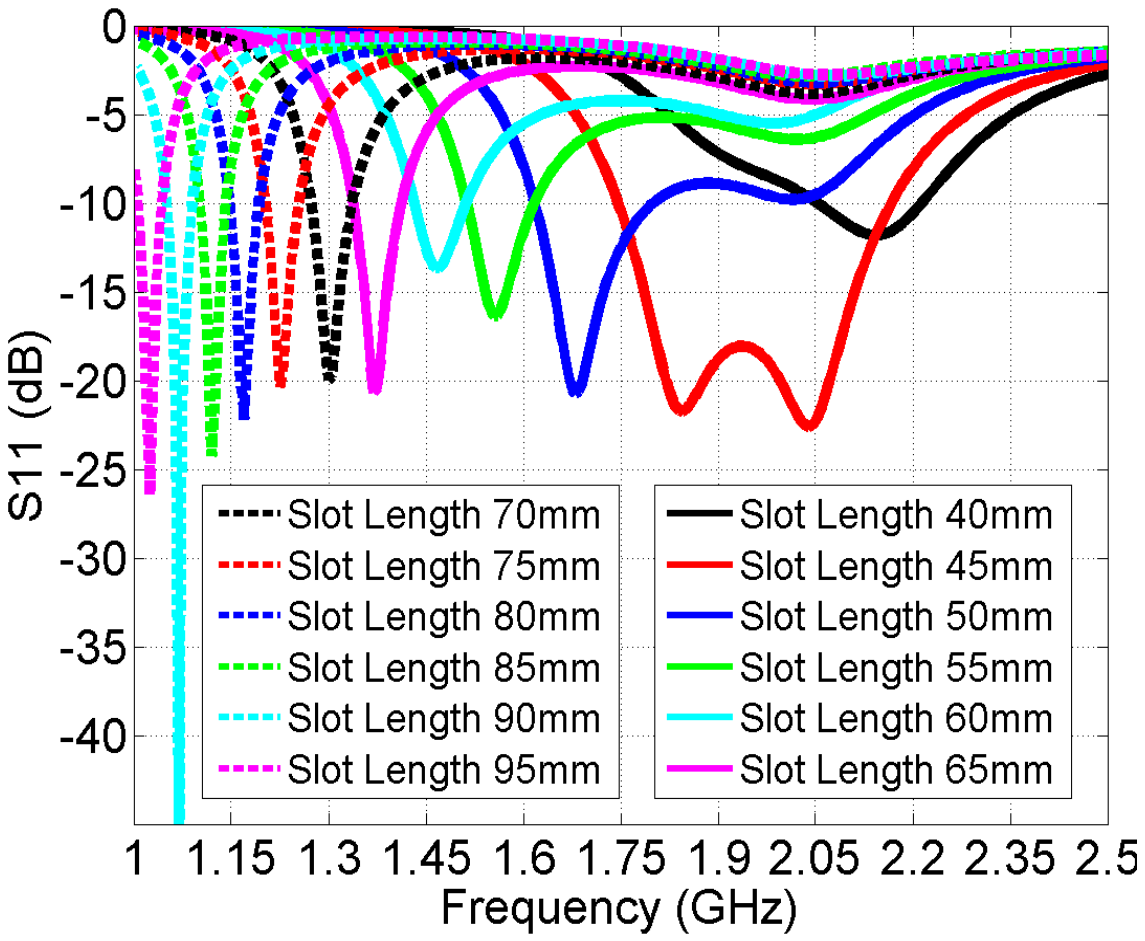

Figure 4.5 Simulated S11 (dB) of aperture coupled patch with slot length, L_p as the parameter.

Similarly, parametric simulations were done to observe the effects of the slot width (Figure 4.6). For a fixed slot length of 45 mm and a fixed stub length of 4.5 mm the slot width was varied from 1.5 mm to 6 mm. In general as the slot width increases the S11 magnitude also increases (slot width of 1.5 mm and 2 mm being exceptions). As seen, with a 2 mm wide slot there is a substantial increase in the depth of the resonance at 1.82 GHz compared to a 1.5 mm wide slot.

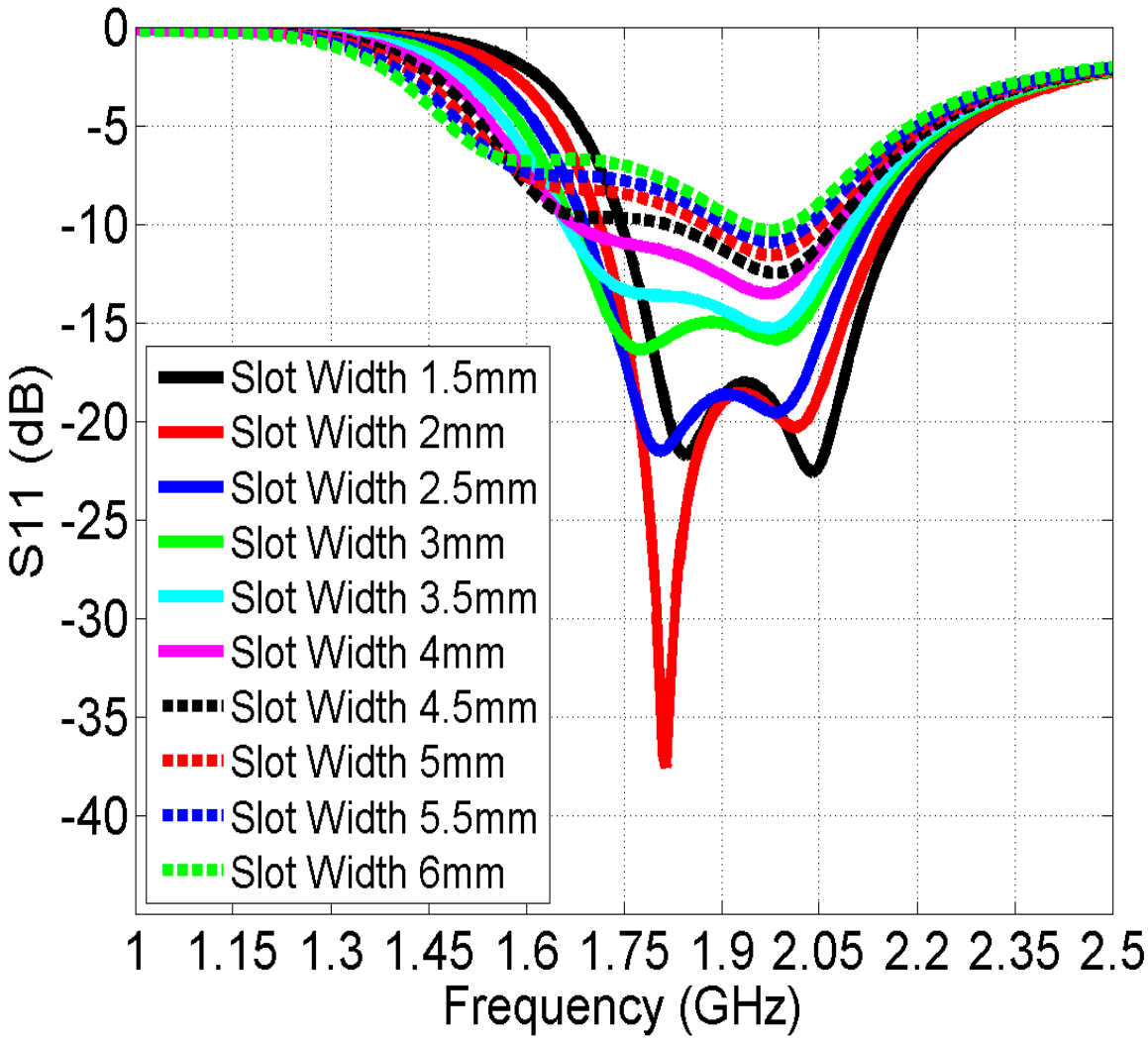

Figure 4.6 Simulated S11(dB) Vs. frequency with the coupling slot width, W_p as the parameter.

One more parametric simulation was performed to characterize the parameters of the slot and feed line coupling. The tuning stub length was changed from 0 mm to 12 mm. The same design shown above was used for these simulations with the slot length kept at 45 mm and the slot width kept fixed at 1.5 mm. The stub length was changed from 0 -12 mm. In the S11 plot shown in Figure 4.7 it seems that the resonance shifts up in frequency as the tuning stub is shortened. From this observation, we can assume that shorter stubs add capacitance to the coupling impedance. A reactance plot is provided

below to support this observation. It is obvious from the reactance plots of Figure 4.8 that shorter stubs can be used as capacitive tuners. It can also be seen that the reactance is nearly constant from 1.75 GHz to 2.28 GHz which explains the increased bandwidth with these parameters.

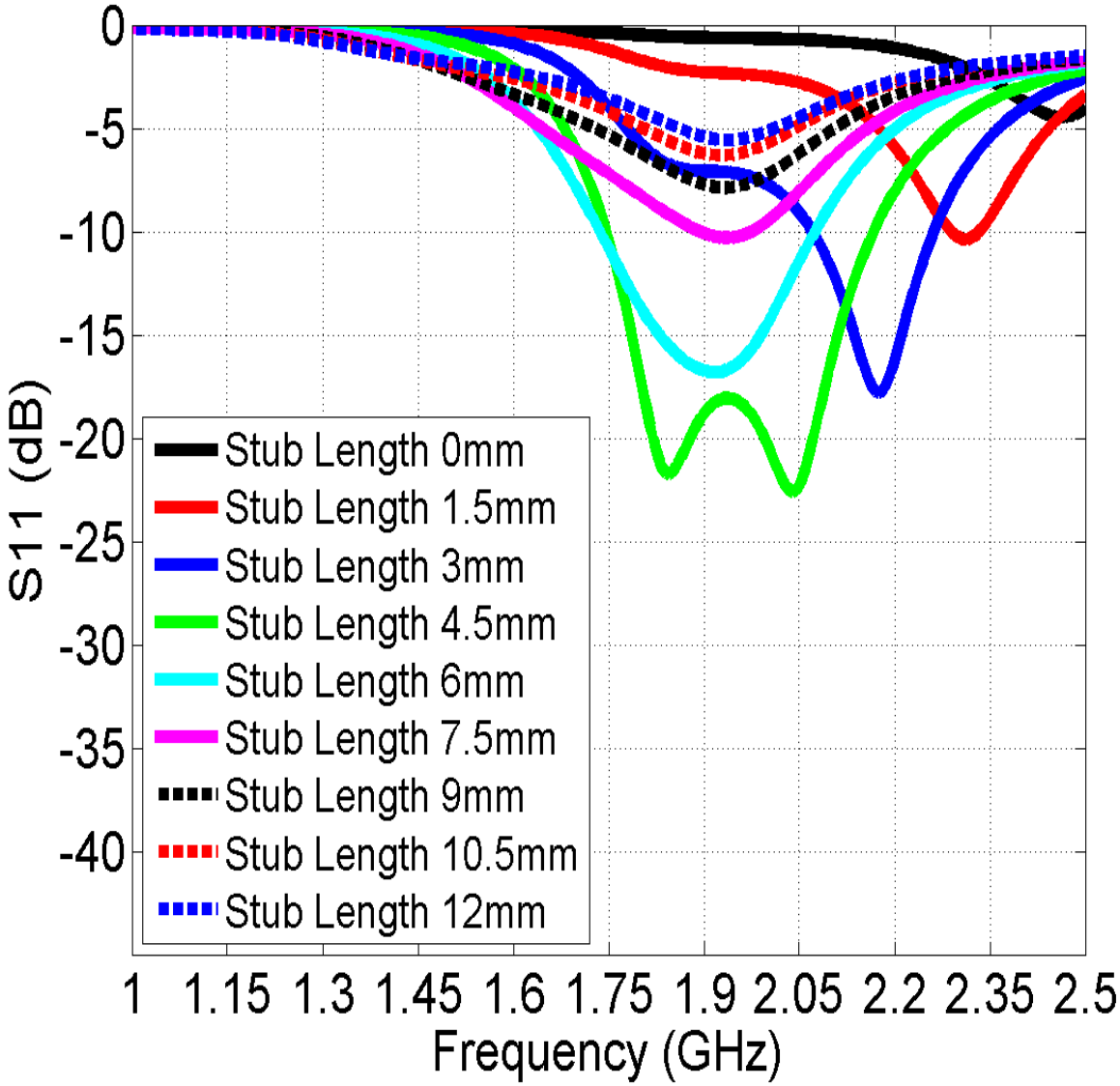

Figure 4.7 Simulated S11(dB) Vs. frequency with the stub length as the parameter.

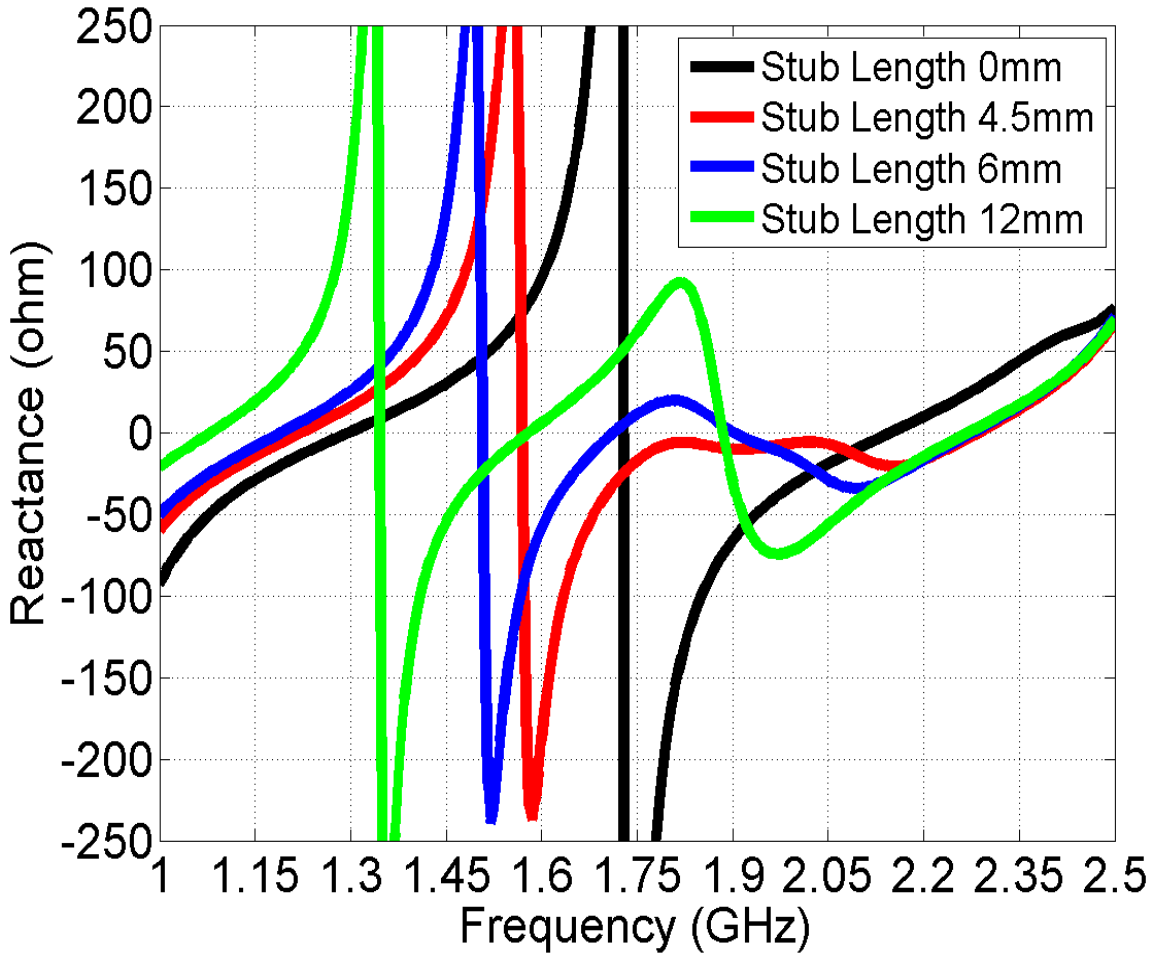

Figure 4.8 Input resistance and reactance Vs. frequency with the stub length as the parameter.

4.3 APERTURE COUPLED PIXEL PATCH ANTENNA

4.3.1 Frequency Reconfiguration with Different Aperture Slot Dimensions

An aperture coupled pixel patch antenna was designed as shown in Figure 4.9. As shown the pixel patch consists of an array of conducting pixels on a thick (17 mm) foam substrate. The shift in the operating frequency was achieved by changing the patch

dimensions and by adjusting the slot dimensions. The patch dimension (L) was changed by either joining or disconnecting the conductive pixels.

Two adjacent pixels were joined by adding a small narrow conducting trace between them that represented a short circuit. While disconnecting the pixels the conducting trace was removed. The conductive pixels were each 5 mm 5 mm squares making a 10 by 13 matrix (thus total number of pixels = 130). There was a separation of 2.5 mm between two adjacent pixels. When the pixels were connected to each other this separation space was shorted using a 1 mm wide conducting trace. The pixel area had a total length of 72.5 mm and a total width of 95 mm if all of them were connected to each other. The conductive pixels that made up the antenna were on top of a 17 mm thick foam ($\varepsilon_r = 1.07$ and $\tan\delta = 0.0009$) material.

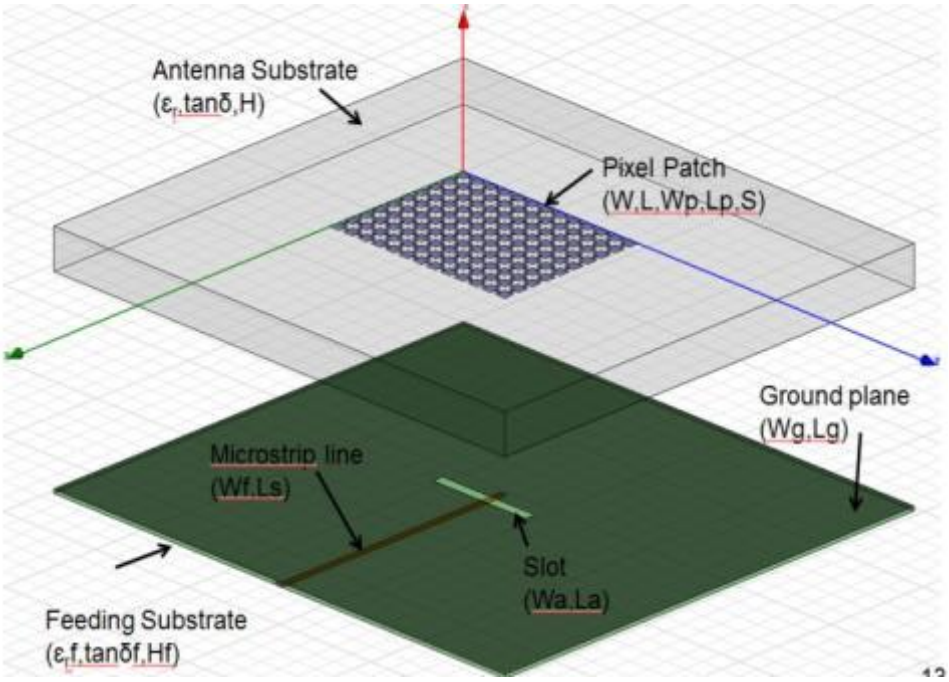

Figure 4.9 Initial aperture coupled pixel patch antenna.

There was a 1.58 mm thick dielectric cover ($\varepsilon_r = 2.5$ and $\tan\delta = 0.0023$) on the pixel patch. There was a ground plane below the foam 222.5 mm long (in the x direction) and

245 mm wide (in the y direction). There was a second substrate below the ground that had a 50 Ω microstrip feed line on it. The second substrate was 1.58 mm thick RO4003 (ε_r=3.55 and tanδ=0.0027). The slot on the ground plane was 5 mm wide (in the x direction) and 50 mm long (in the y direction).

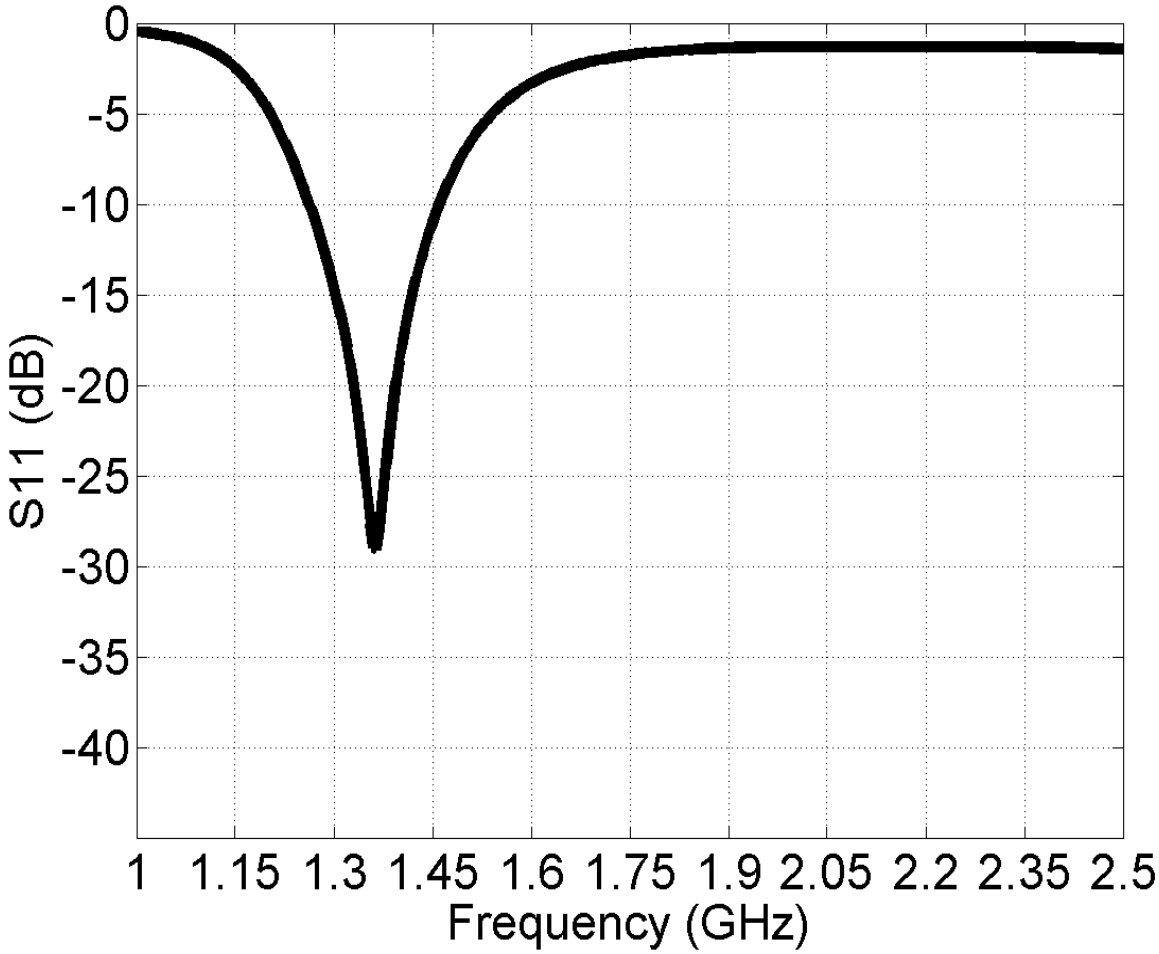

Figure 4.10 Simulated S11(dB) Vs. frequency of the aperture coupled pixel patch antenna for 13 by 10 pixels.

The first case simulated was when all the pixels were connected to each other. The S11 magnitude in dB Vs. freqeuncy for this case are shown in Figure 4.10. As seen, the operating frequency band extends from 1.26 to1.46 GHz giving a bandwidth of 14.3%. The peak realized gain at the center frequency of 1.365 GHz is 11 dBi and the

half power beamwidths in the E-Plane (phi = 0) and H-Plane(phi = 90) are 53^{o} and 66^{o}, respectively. The F/B is 11 dB.

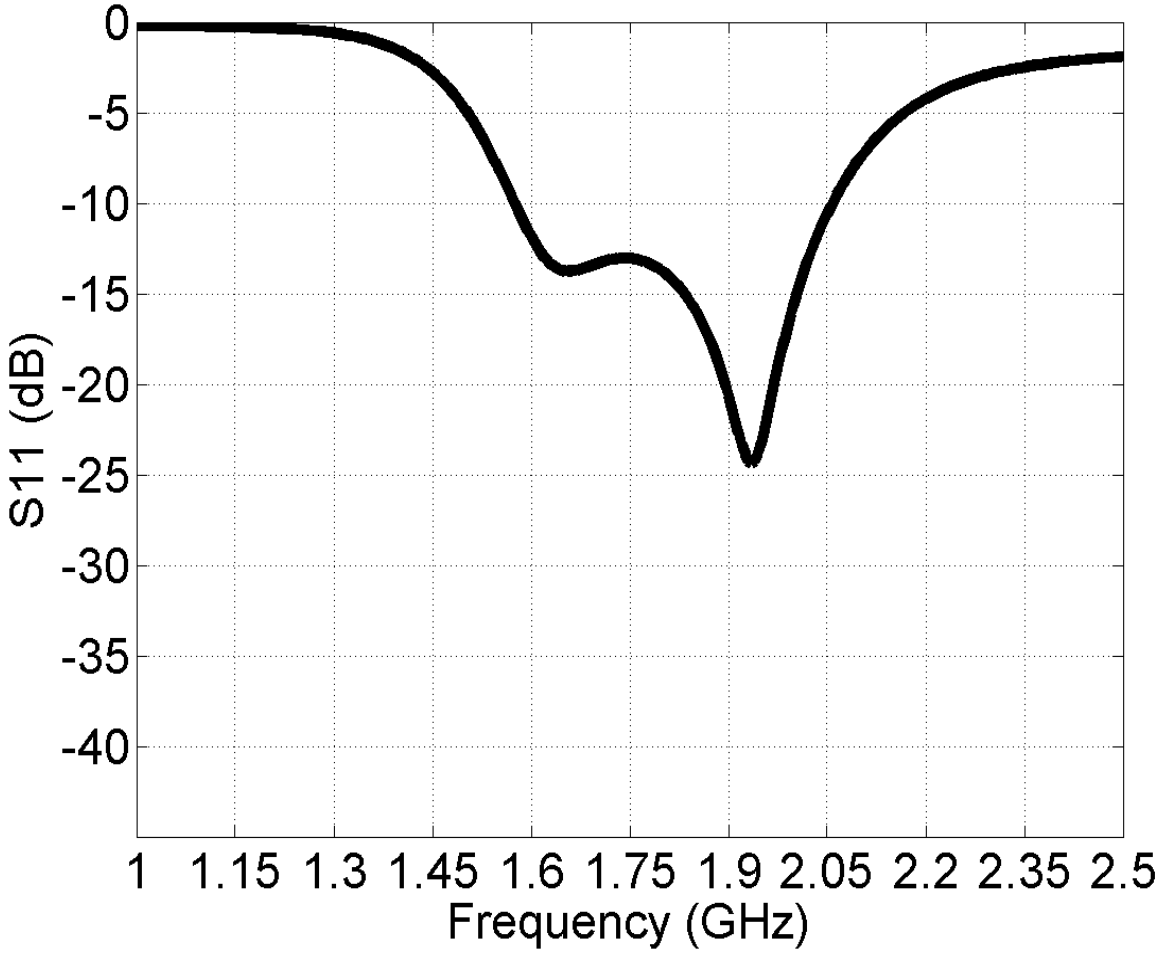

Figure 4.11 Simulated S11 (dB) Vs. frequency for the aperture coupled pixel patch antenna for 9 by 7 pixels.

The results of a second case simulated are shown in Figure 4.11 which represents 9 by 7 pixels (65 mm by 50 mm). The dielectric cover, the foam material, and the feed line substrate all remained unchanged. The slot on the ground was 45 mm long and 4.5 mm wide. As seen in Figure 4.11, the operating frequency band extends from 1.575 to 2.055 GHz. The peak realized gain at the center frequency of 1.815 GHz is 9.7 dBi and

the half power beamwidths in the E-Plane (phi = 0) and H-Plane(phi = 90) are 50^o and 66^o respectively The F/B is 10 dB. These properties are also listed in Table 4.1

Table 4.1: Characteristics of the aperture coupled pixel patch antenna; f_L represents the low frequency, f_0 represents the center frequency, and f_H represents the high frequency.

	Low Frequency	High Frequency
Center Frequency	1.3625 GHz	1.815 GHz
Bandwidth	14.3%	26.4%
Directivity at f_L	8.9	8.7
Directivity at f_o	9.7	9.9
Directivity at f_H	10.1	10.4
Realized Gain at f_L	8.3	8.1
Realized Gain at f_o	9.6	9.7
Realized Gain at f_H	9.7	9.8
F/B at f_L	9.8	7.2
F/B at f_o	10.9	10.7
F/B at f_H	10.9	13.5

4.3.2 Frequency Reconfiguration with Fixed Length Slot

Since it is impractical to actually change the slot length further simulations of antenna frequency reconfiguration were performed by using a fixed length slot. All substrate materials and their thicknesses remained unchanged. The length and width of the ground, and the dielectric materials were 215 mm by 215 mm. The patch active area consisted of a 3 by 7 matrix of conductive pixels giving a total length and width of 20 mm and 50 mm. The slot on the ground was 35 mm long and 4.5 mm wide. For this pixel patch with a fixed slot length the frequency bandwidth extends from 2.545-2.82 GHz (Figure 4.12). The peak realized gain at the center frequency is 7.5 dBi and the half power beamwidths in the E-Plane (phi =0) and H-Plane (phi=90) are 71^o and 74^o respectively The F/B is 9.1 dB.

The results above show that the sharpest resonance appears when the slot has a length of 50 mm. As the slot length increased so did the resonant frequency. The frequency bandwidth with a 50 mm long slot is from 1.66-1.79GHz with S_{11}< -10dB. The peak realized gain at the center frequency was 8.1 dBi with a half power beamwidth in the E-Plane (phi =0) and H-Plane (phi=90) of 66^o and 62^o. The front to back ratio (F/B) is 6 dB. The second pixel patch consists of a 9 by 5 matrix of pixels giving the patch a total length and width of 35 mm and 65 mm. The slot length on the ground was varied from 30 to 65 mm in 5 mm intervals with a constant width of 4.5 mm.

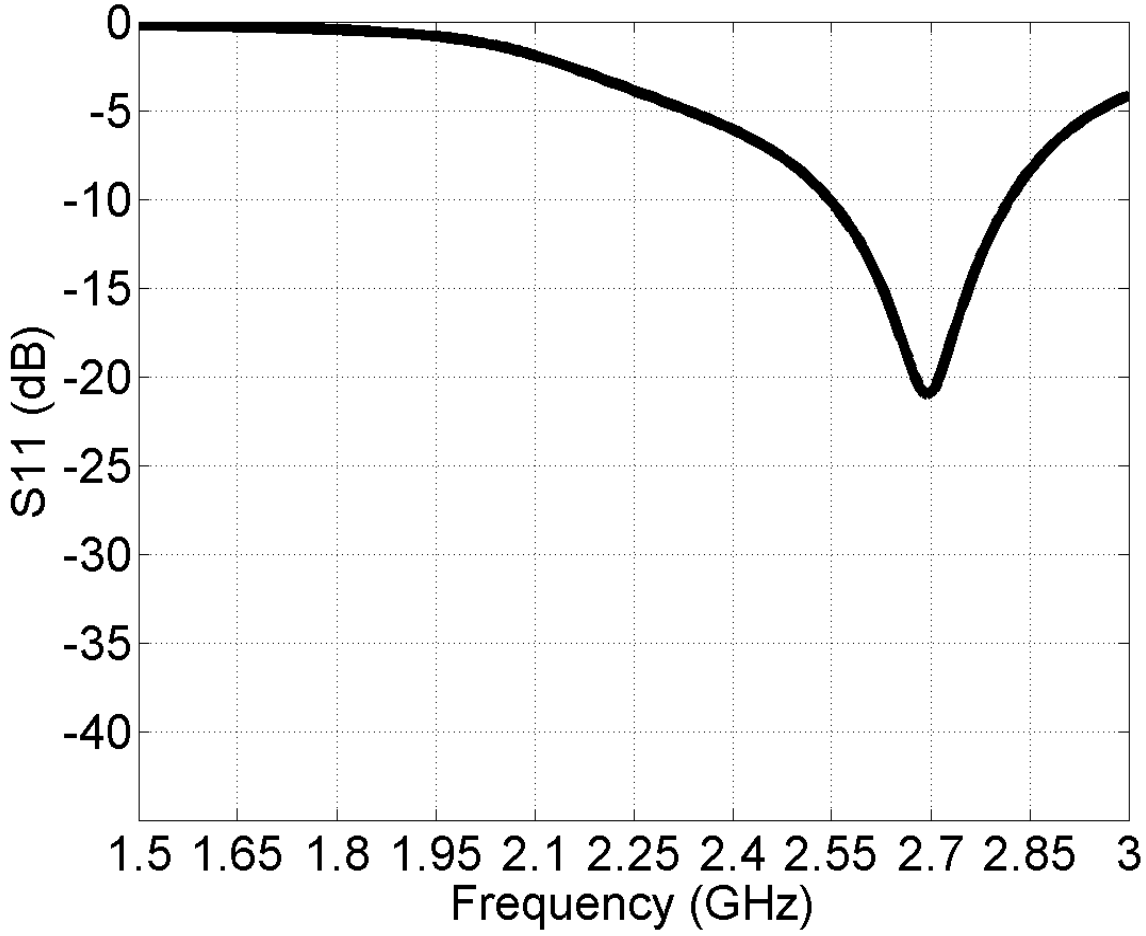

Figure 4.12 Simulated S11(dB) Vs. frequency of aperture coupled pixel patch antenna with a fixed slot length.

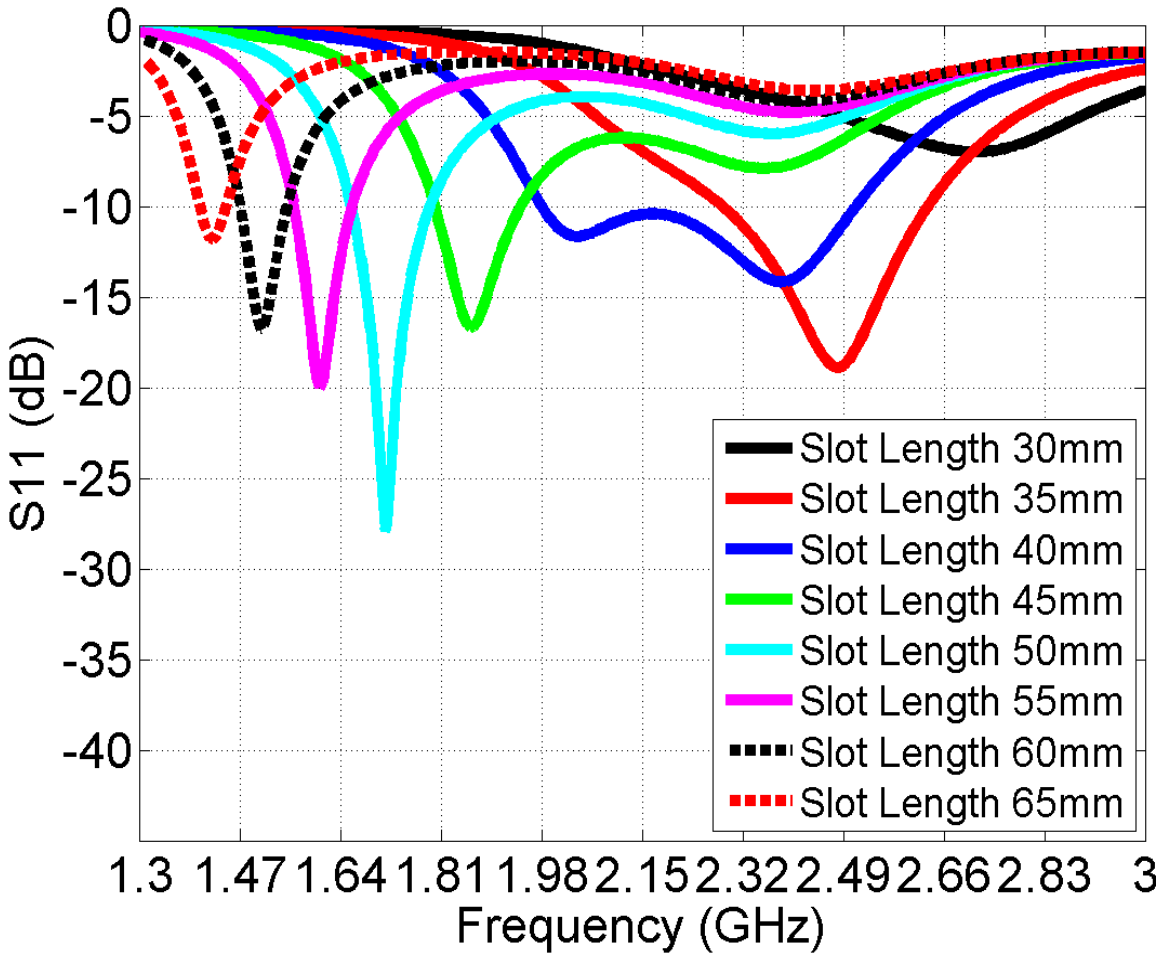

Figure 4.13 Simulated S11(dB) Vs. frequency of aperture coupled pixel patch antenna with a variable slot length.

4.3.3 Frequency Reconfiguration with a Fixed Length Slot

A reconfigurable aperture coupled pixel patch antenna for frequency reconfiguration is proposed below. The geometry of the patch will be increased or decreased by shorting a row of conductive pixels. The slot dimensions on the ground plane will remain fixed. But the length of the tuning stub, L_s over the slot area will be adjusted using switches.

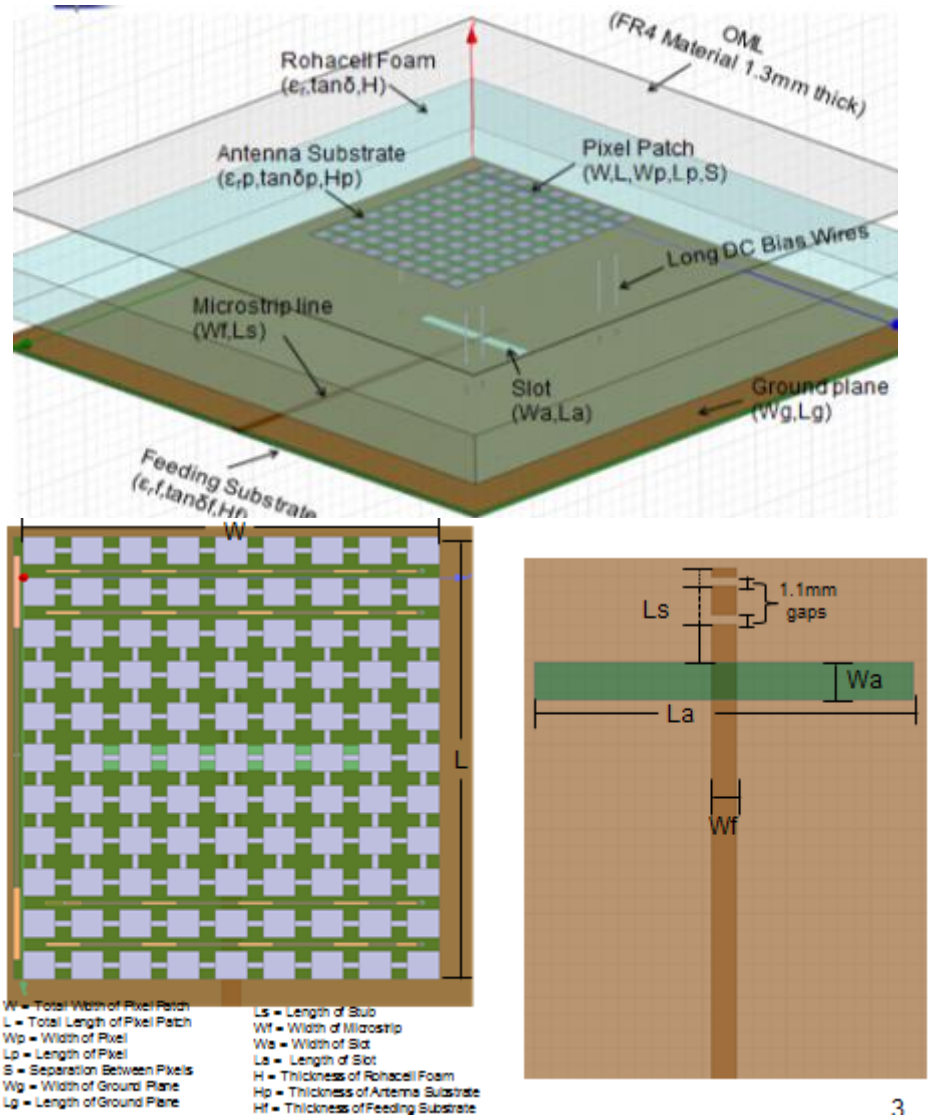

Figure 4.14 Reconfigurable pixel (11 by 9) patch antenna with fixed length slot. Each pixel is 5 mm by 5 mm and inter-pixel space is 2.5 mm.

The preliminary design did not contain any switch bias traces, switch/resistor pads, DC connection vias, and other layer to layer vias. This baseline design consisted of pixel patches that were joined using a conducting trace as before. When a shorter pixel patch was desired the connection was simply broken by removing the conducting trace in the simulation model. The pixel patches were placed directly on the thick foam material as before. The pixel patch was covered using a 1.58 mm thick dielectric cover. And the

feed transmission line and the slot were created on a 1.58 mm RO4003 substrate. Frequency reconfiguration was achieved by connecting or disconnecting the conductive pixels while the stub length, L_s was varied to improve the impedance matching at each frequency of operation. The S11 (dB) versus frequency for three cases of frequency reconfigurations are shown in Figure 4.15.

The black trace shows the S11 Vs. frequency response for the highest frequency of reconfiguration. Referring to Figure 4.14, in this configuration all ideal switches are open and thus the antenna has the smallest active length resulting in the highest frequency of operation. The tuning stub length, L_s is 4.5 mm which is the shortest among the three cases. This intuitively makes sense because the smaller patch should be more inductive and it was discussed earlier that a shorter tuning stub will move the impedance circle toward the capacitive part of the Smith chart. The red trace represents the reconfiguration at an intermediate frequency because the switches in rows 1 and 2 are now activated. The length of the tuning stub is now 7 mm. Note that the patch is still resonant for a 4.5 mm long tuning stub but the impedance matching provided was a bit worse. The blue trace represents the lowest frequency of reconfiguration in this sequence because it considers all switches activated and hence has the longest active length. The length of the tuning stub, L_s is 11 mm. It is clear that the widest bandwidth is obtained with the black trace. This occurs because the resonant frequencies due to the two cavities (slot and patch) are near each other. The patch active region has a length of 50 mm (7 pixels) and width of 65 mm (9 pixels) which has a resonance around 2 GHz while the slot resonant length is around 1.8 GHz. The $|S_{11}|$<-10 dB bandwidth for the high, center, and low frequency reconfiguration are 25.8%, 15%, and 7.5%, respectively. The peak realized gain at each

frequency shift at their respective center frequencies starting with the highest are 9.8 dBi, 9.7 dBi, and 9.3 dBi and the F/B are 11.8 dB, 11.7 dB, and 11.3 dB, respectively. The active areas for the middle and low frequencies are 65 mm by 65 mm and 80 mm by 65mm, respectively.

Systematic simulations were performed to observe and understand the losses that will occur if substrates like FR4 ($\tan\delta = 0.02$) are used to fabricate and assemble the antenna as opposed to RO4003 ($\tan\delta = 0.0023$). These simulations also considered a thin substrate for the pixel patches to be fabricated. Thus unlike all previous cases when the pixel patches were considered to be directly placed on the 17 mm thick foam material the next set of data represents pixel patches that were modeled on a 0.4 mm thick FR4 substrate. The pixels were then covered with a 1.3 mm thick FR4 dielectric layer. Similarly a 1.58 mm thick FR4 substrate was used to construct the microstrip feed line and the slot. The S11 (dB) versus frequency plot for these cases are shown in Figure 4.16.

Comparing Figure 4.15 and Figure 4.16, it is clear that the resonant frequencies did not decrease significantly. At the highest frequency of reconfiguration the center frequency shifted from 1.785 GHz to 1.647 GHz while at the intermediate frequency the shift was from 1.492 GHz to 1.377 GHz and at the lowest frequency the shift was from 1.272 GHz to 1.23 GHz. Thus the shifts were 138 MHz, 115 MHz and 42 MHz for each reconfiguration. The gain at these center frequencies were 8.9 dBi, 8.3 dBi, and 8.1 dBi which were 0.9 dB, 1.4 dB, and 1.2 dB lower than the gain with the RO4003 material.

In order to fabricate a reconfigurable aperture coupled pixel patch antenna, parasitic effects of switch biasing network, resistor and switch pads were investigated

next. Figure 4.17 shows the S11 (dB) Vs. frequency characteristic for the high frequency of reconfiguration. As seen, there are four cases illustrated:

- Case 1 (black trace) - Reconfigurable pixel patch using FR4 and foam that does not contain any DC bias traces, vias or bias and ground wires.
- Case 2 (red trace) - DC bias traces are added to Layers 1 and 2 as shown in Fig. 6.14.
- Case 3 (blue trace) - Vias are added to connect the DC traces on Layers 1 and 2 of the 0.4 mm thick FR4 substrate containing the pixels.
- Case 4 (green trace) Long DC bias wires are run from Layer 2 and then through the foam and then through the ground plane of substrate 2 (Final).

Figure 4.18 shows the S11 plot for the intermediate frequency shift. Figure 4.19 shows the S11 plot for the low frequency shift. The S11 versus frequency plot of the final frequency reconfigurable aperture coupled pixel patch antenna is shown on Figure 4.20. The final model has all FR4 substrates and all biasing traces and wires that are needed to bias the switches. The highest frequency shift has a center frequency of 1.542 GHz and a -10 dB bandwidth of 12.6%. The center frequency shift seems to have a dual resonance at 1.247 GHz and 1.325 GHz with a -10 dB bandwidth of 2.8% and 4.5% respectively. The lowest frequency shift has a center frequency of 1.185 GHz and a -10dB bandwidth 5%. It is apparent that the addition of the DC bias traces, bias pads, and DC signal and ground wires deteriorated the impedance match of the antenna which reduced its bandwidth in each of the frequencies of reconfiguration. It is clear that by adjusting a number of parameters including the thickness of the foam layer, the dimensions of the coupling slot,

the dimension of the tuning stub, and the diameters of the long bias wires as well the widths of the DC bias traces the bandwidths can be significantly improved.

Simulated radiation patterns in the E and H-plane for the different frequencies are shown in Figure 4.21. The broadside gain at each respective frequency shift starting with the highest is 8.1 dBi, 6.3 dBi, 7.2 dBi, and 7.1 dBi including the two resonances at the center frequency shift. The F/B ranges from 13.4 dB to 10.4 dB with the ratio decreasing as the frequency increases. The 3 dB beamwidths in the E and H-plane range from 60^{o} to 54^{o} and 72^{o} to 58^{o}.

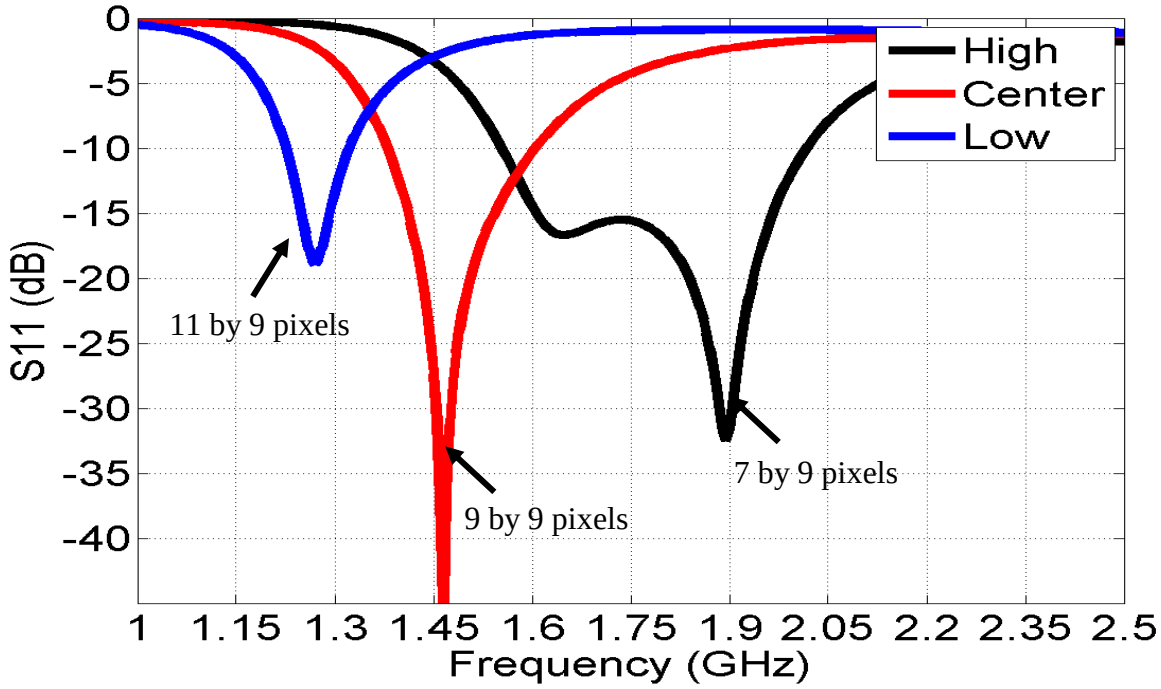

Figure 4.15 Frequency reconfiguration of aperture coupled pixel patch with fixed length
slot

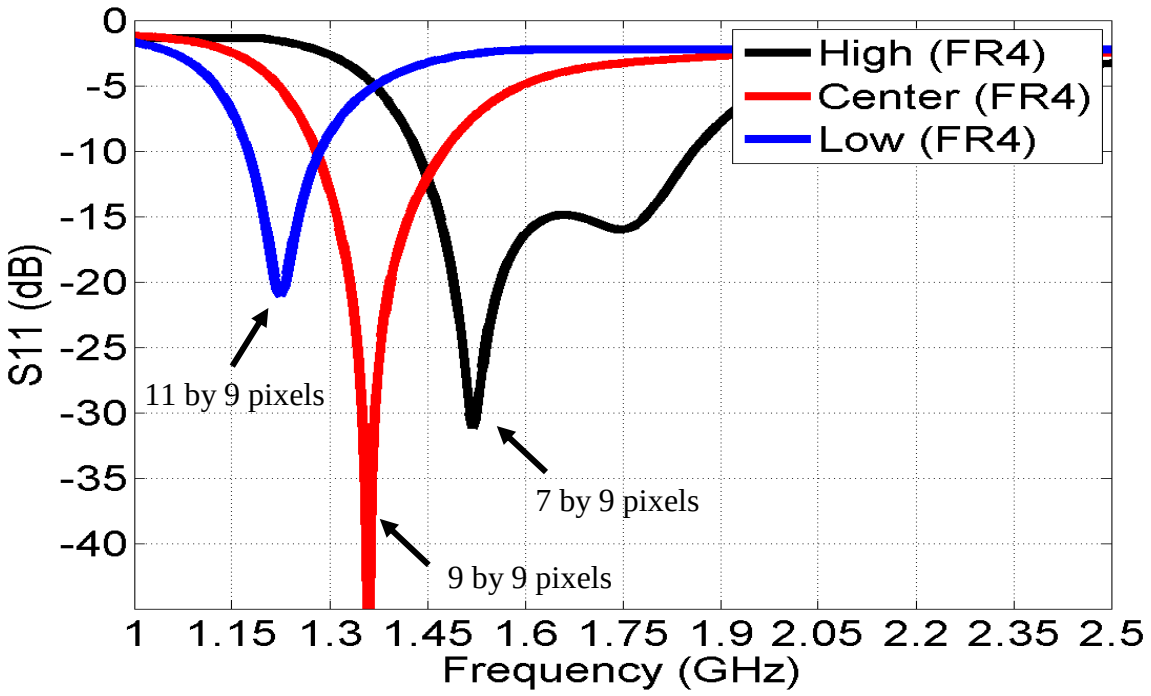

Figure 4.16 Frequency reconfiguration of aperture coupled pixel patch with fixed length slot with FR4 materials.

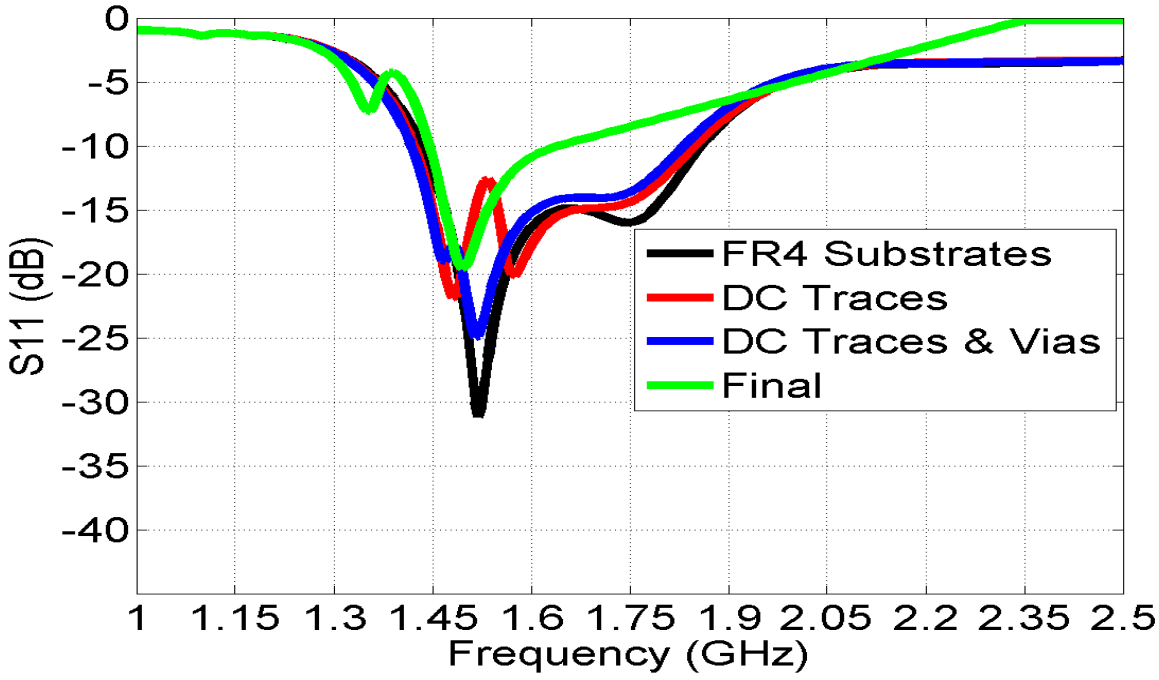

Figure 4.17 Frequency reconfiguration of aperture coupled pixel patch with fixed length slot with FR4 material and in the presence of switch bias networks and vias.

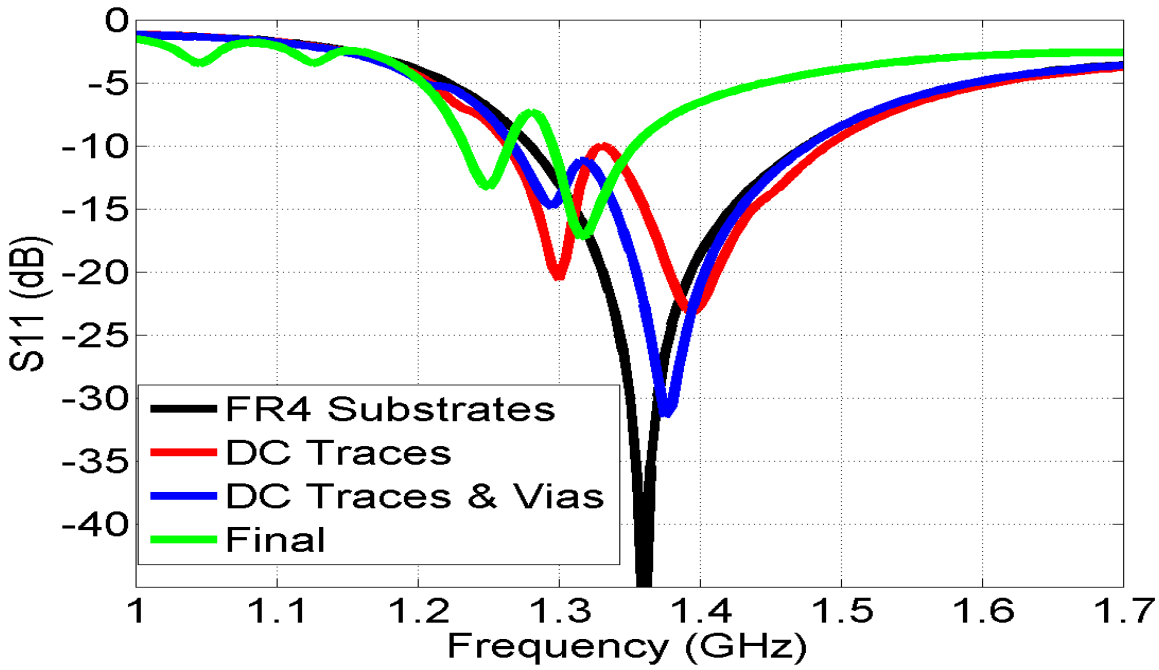

Figure 4.18 Frequency reconfiguration of aperture coupled pixel patch with fixed length slot with FR4 material and in the presence of switch bias networks and vias.

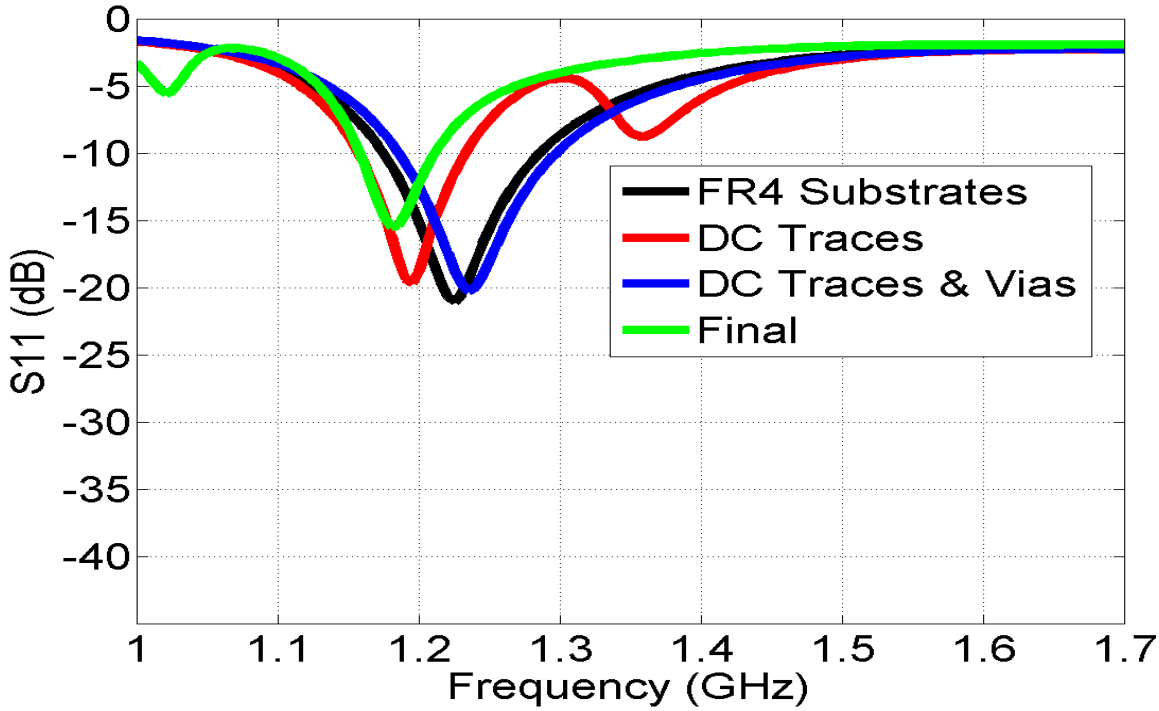

Figure 4.19 Frequency reconfiguration of aperture coupled pixel patch with fixed length slot with FR4 material and in the presence of switch bias networks and vias.

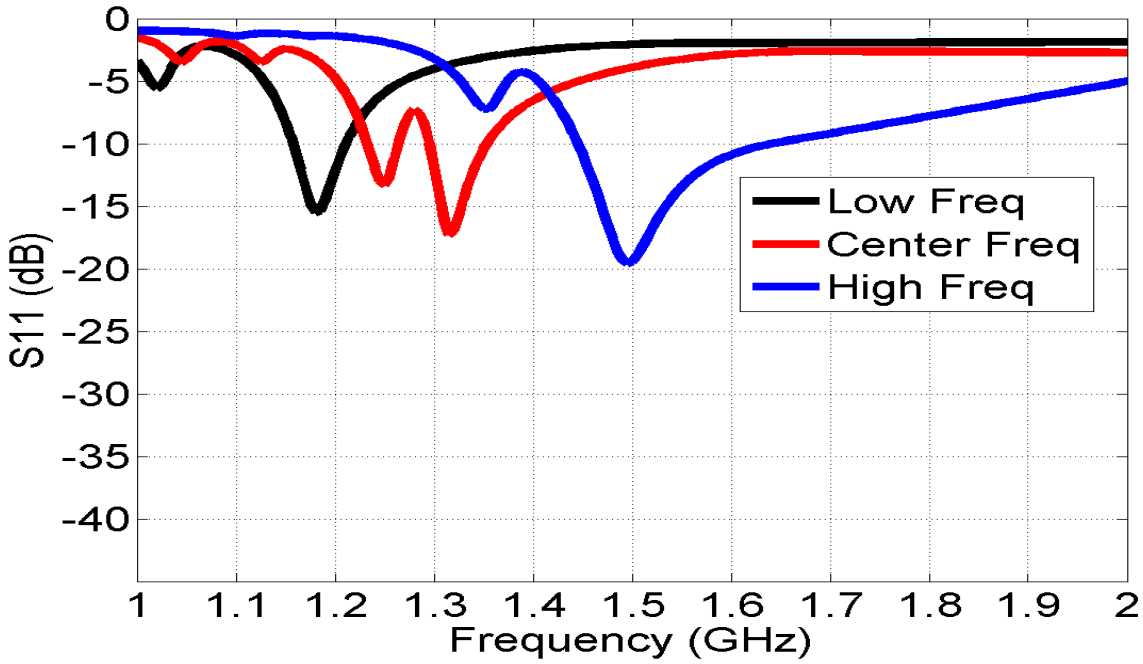

Figure 4.20 Frequency reconfiguration of aperture coupled pixel patch with fixed length slot with FR4 material and in the presence of switch bias networks and vias.

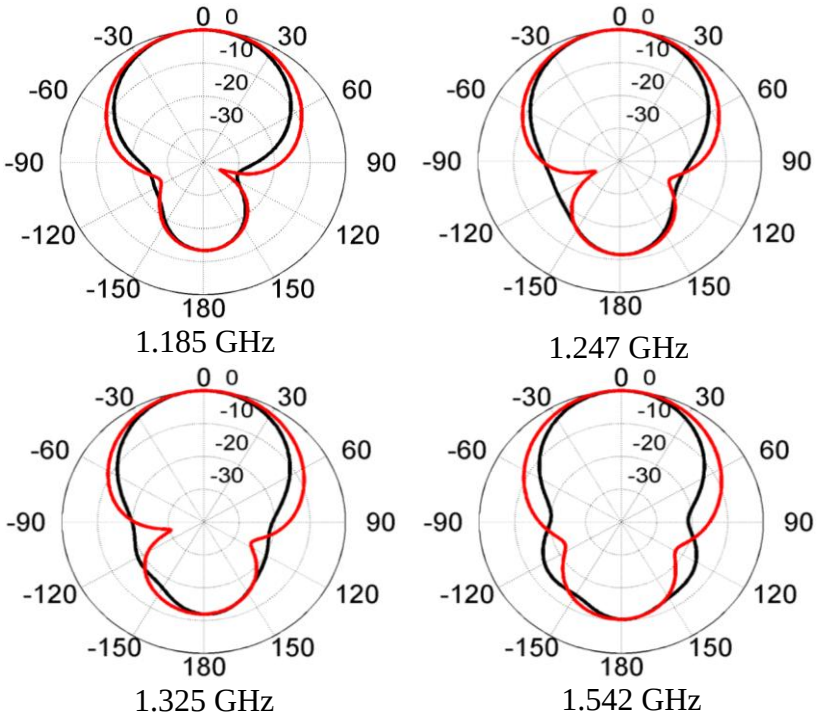

Figure 4.21 Simulated normalized radiation pattern plots. Black representing the pattern on the E-plane (phi = 0) and the red trace representing the pattern on the H-plane (phi =90).

CHAPTER 5

CONCLUSIONS AND FUTURE WORK

The study and design of a broadband VHF-UHF Yagi-Uda array are presented in Chapter 2. A sleeve dipole was used as the driven element to increase the VSWR bandwidth. The array with no dielectric material has nearly an octave of VSWR and gain bandwidths. Loading the array with 0.508 mm thick RO4003 substrate and superstrate decreases the VSWR bandwidth to a frequency ratio of 1.7 (240-410 MHz).

The analysis, design, fabrication and tests of a broadband size-reduced UHF bi-layer LPDA was presented in Chapter 3. The use of a double meander dipole as the building block allows a 30% reduction in the array width. Further reduction is still possible as long as inter-element coupling does not deteriorate the array performance. It is clearly demonstrated that the two layers of the LPDA can be sufficiently separated from each other (1 inch to 1.5 inch) for the 350-750 MHz operation. The sensitivity of the array VSWR and radiation properties in the presence of dielectric materials, on cable size, and cable orientation are studied. It is observed that a symmetric feeding arrangement consisting of same diameter cable and conducting tube with a small separation distance between them is preferred. The presence of thin FR4 dielectric materials has no significant detrimental effect on the array performance except for the gain loss due to the high loss tangent of the FR4 material. Thus other low loss materials such as RO4003 will be a better choice. The fabricated array shows a VSWR bandwidth

of 350-750 MHz. The gain of the fabricated array is above 7 dBi for most of the operating frequency band. Better control of the distance between the feed line and the conducting tube will reduce the VSWR and increase the array gain. The E and H-plane radiation patterns of the array show well defined directional beams with high F/B for most frequencies of operation. Further simulation studies of the array in the presence of dielectric support members delineate the sensitivity of the array performance to such members. Clearly a low dielectric constant support member such as that made from PTFE or foam will be a preferred choice. In case where needed a short dielectric support member and short foam support member could be used. The array performance in the presence of an external graphite support member shows slight more degradation in the VSWR results. Finally alternatives of using a small coaxial cable and a large diameter conducting tube are also investigated which show that this is a possible choice only if small distances can be maintained. Further work will be needed in order to design and tune the array to suit a specific platform geometry and material system.

In Chapter 4 a frequency reconfigurable aperture coupled pixel patch antenna was designed and simulated. Preliminary measured VSWR results of a 4 by 4 matrix of pixels using eight RMSW101 MEMs switches to increase the length of the radiating patch are introduced at the beginning of the chapter. The MEMs switches were connected using wire bond technology and the antenna was feed using a coaxial probe. Later the analyses of an aperture coupled reconfigurable pixel antenna were presented. Parametric studies were provided to better understand the antenna performance. Simulations were done to take into consideration of the parasitic effects of the biasing network needed to activate the MEMs switches during reconfiguration. The final frequency reconfigurable aperture

coupled antenna had three reconfigurable frequencies. The highest frequency shift has a center frequency of 1.542 GHz and a -10 dB bandwidth of 12.6%. The center frequency shift seems to have a dual resonance at 1.247 GHz and 1.325 GHz with a -10 dB bandwidth of 2.8% and 4.5% respectively. The lowest frequency shift has a center frequency of 1.185 GHz and a -10 dB bandwidth of 5%. The broadside gain at each respective frequency shift starting with the highest is 8.1 dBi, 6.3 dBi, 7.2 dBi, and 7.1 dBi including the two resonances at the center frequency shift. The F/B ranges from 13.4 dB to 10.4 dB with the ratio decreasing as the frequency increases. The 3 dB beamwidths in the E and H-plane range from 60^{o} to 54^{o} and 72^{o} to 58^{o}.

5.1 FUTURE WORKS

Limited studies were conducted on the end-fire arrays being fully integrated into an air vehicle platform because of geometry translation issues and lack of extensive computational resources. More simulations and fabrication of the end-fire arrays fully integrated considering structural elements like motor, wires, structural supports, and fuel should be conducted.

The reconfigurable aperture coupled pixel patch antenna is still in its preliminary stage of research. Simulations and modeling considering switch losses should be the next stage of the research. Finally, the reconfigurable aperture coupled pixel patch should be built and tested to validate performance.

REFERENCES

[1] P. J. Callus, *Novel Concept for Conformal Load-bearing Antenna Structure*, Air Vehicles Division, Defence Science and Technology Organisatio, *DSTO, 506 Lorimer St, Fishermans Bend, Victoria 3207 Australia*

[2] P. J. Callus, *Conformal Load-Bearing Antenna Structure for Australian Defence Force Aircraft*, Air Vehicles Division, Defence Science and Technology Organisatio, DSTO, *506 Lorimer St, Fishermans Bend, Victoria 3207 Australia*

[3] J.L. Wong and H.E. King, "An experimental study of a balun-fed open sleeve dipole in front of a metallic reflector,'' *IEEE Trans. Antennas Propagat.*, March 1972, pp. 201-204.

[4] M. Ali, M. Okoniewski, M.A. Stuchly, and S.S. Stuchly. "Dual-Frequency Strip-Sleeve Monopole for Laptop Computers," *IEEE Trans. Antennas Propagat.*, vol. 47, no. 2, Feb. 1999, pp. 317-323.

[5] M. Ali. "Analyses of Self-Resonant Bent Antennas," Ph.D. Dissertation, University of Victoria, BC, Canada.

[6] M. Ali, S.S. Stuchly, and K. Caputa. "A Wide-Band Dual Meander-Sleeve Antenna," *Journal of Electromagnetic Waves and Applications*, vol. 10, No. 9, 1996, pp. 1223-1236.

[7] M. Ali, G.J. Hayes, H.-S. Hwang and R.A. Sadler. "Design of a Multi--Band Internal Antenna for Third Generation Mobile Phone Handsets," *IEEE Trans. Antennas Propag.*, vol. 51, no. 7, July 2003, pp. 1452-1461.

[8] C. Yu, W. Hong, L. Chiu, G. Zhai, C. Yu, W. Qin, and Z. Kuai. "Ultrawideband printed log-periodic dipole antenna with multiple notched bands,'' *IEEE Trans. Antennas Propagat.*, vol. 59, March 2011, pp. 725-732.

[9] D.E. Anagnostou, J. Papapolymerou, M.M. Tentzeris, and C.G. Christodoulou. "A Log-Periodic Koch Dipole Array (LPKDA)," *IEEE Antennas Wireless Propagat. Lett.*, vol. 7, Dec. 2008, pp. 456-460.

[10] N. Kaneda, W.R. Deal, Y. Qian, R. Waterhouse, and T. Itoh,."A broadband planar quasi-Yagi Antenna,'' *IEEE Trans. Antennas Propagat.*, vol. 50, Aug. 2002, pp. 1158-1160.

[11] M.A. Ali and P. Wahid. "A reconfigurable Yagi array for wireless applications,'' *IEEE Antennas and Propagation Society Int. Symp. Dig.*, vol.1, pp. 466-468.

[12] R. Carrel. "The design of log-periodic dipole antennas," *IRE International Convention Record.*, 1961, vol. 9, pp. 61-75.

[13] R. L. Carrel. "Analysis and design of the log-periodic dipole antenna," University of Illinois Technical Report, No. 52, Urbana, 1961.

[14] V. H. Rumsey, Frequency Independent Antennas. New York: Academic Press, 1966.

[15] W.L. Stutzman and G.A. Thiele. *Antenna Theory and Design*. USA. John Wiley and Sons Inc., 1998.

[16] P. B. Green and P. E. Mayes. "50Ω log-periodic monopole array with modulated-impedance microstrip feeder," *IEEE Trans. Antennas Propag.*, vol. AP-22, pp. 332-334, March 1974.

[17] K. M. Keen. "A planar log-periodic antenna," *IEEE Trans. Antennas Propag.*, vol. AP-22, pp. 489-490, May 1974.

[18] C.K. Campbell, I. Traboulay, M.S. Suthers, and H. Kneve. "Design of a Stripline Log Periodic Dipole Antenna," *IEEE Trans. Antennas Propag.*, vol. AP-25, pp. 718-721, Sept. 1977.

[19] R. R. Pantoja, A. R. Sapienza, and F. C. Medeirosfilho. "A Microwave Printed Planar Log-Periodic Dipole Array Antenna,'' *IEEE Trans. Antennas Propag.*, vol. AP-35, pp. pp. 1176-1178, Oct. 1987.

[20] A. A. Gheethan and D. E. Anagnostou. "The Design and Optimization of Planar LPDAs,'' PIERS Proceedings, Cambridge, USA, July 2008, pp. 478-481.

[21] D. Anagnostou, J. Papapolymerou, M.M. Tentzeris, and C.G. Christodoulou. "A Printed Log-Periodic Koch-Dipole Array (LPKDA),'' *IEEE Antennas and Wireless Propagat. Lett.*, vol. 7, 2008, pp. 456-460.

[22] F. Merli, J.-F. Zürcher, A. Freni, and A.K. Skrivervik. "Analysis, design and realization of a novel directive ultrawideband antenna,'' *IEEE Trans. Antennas Propag.*, vol. 57, pp. 3458-3466, Nov. 2009.

[23] A. Calmon, G. Pacheco, M.A.B. Terada. "A novel reconfigurable UWB log-periodic antenna,'' *IEEE Antennas and Propagation Society Interntaional Symp. Dig.*, 2006, pp. 213-216.

[24] A. Khaleghi, H.S. Farahani, and I. Balasingham. "Impulse Radiating Log-Periodic Dipole ArrayAntenna Using Time-Reversal Technique,'' *IEEE Antennas and Wireless Propagat. Lett.*, vol. 10, 2011, pp. 967-970.

[25] C. Yu, W. Hong, L. Chiu, G. Zhai, C. Yu, W. Qin, and Z. Kuai. "Ultrawideband Printed Log-Periodic Dipole Antenna With Multiple Notched Bands,'' *IEEE Trans. Antennas Propag.*, vol. 59, pp. 725-732, Mar. 2011.

[26] G.A. Casula, P. Maxia, and G. Mazzarella. "A printed LPDA with UWB capability,' *2010 International Workshop on Antenna Technology (IWAT)*, pp. 1.4.

[27] L. Shan, L. Xiaofeng, Q. Jinghui. "A novel miniaturized ultra wideband log-periodic antenna,'' *2010 International Conference on Ultrawideband and Ultrashort Impulse Signals (UWBUSIS)*, pp. 246-248.

[28] B. Turetken. "Design and realization of printed LPDA in UHF band,'' *10th International Conference on Mathematical Methods in Electromagnetic Theory*, 2004., Sept. 14-17, 2004, pp. 295 – 297.

[29] M. N. A. Karim, M. K. A. Rahim, H. A. Majid, O. Ayop, M. Abu and F. Zubir. "Log periodic fractal Koch Antenna for UHF band applications," *Progress In Electromagnetics Research*, PIER 100, 201-218, 2010.

[30] P. Li, X. Jiang, X. Liu, H. Shi, X. Lu. "Research on the relation between Printed Log-Periodic Antenna's feed and bandwidth," *2010 International Symposium on Signals Systems and Electronics*, pp. 1-3.

[31] A. Moallemizadeh, H.R. Hassani, and S.M.A. Nezhad. "Wide bandwidth and small size LPDA antenna,'' *2012 6th European Conference on Antennas and Propagation (EUCAP)*, pp. 1-3.

[32] B. Gong, L.H. Su, Y.-Z. Yin, H. Ma, Q.-R. Zheng. "A novel log-periodic dipole antenna with distributed inductive load,'' *2012 2nd International Conference on Consumer Electronics, Communications and Networks (CECNet)*, pp. 61 – 63.

[33] X.L. Zhang and H.-T. Gao. “An optimum design of miniaturized high frequency inverted-V log-periodic dipole antenna,’’ *2011 IEEE CIE International Conference on Radar (Radar)*, pp. 1185 – 1188.

[34] Q. Zhao and Z. Yin. “The influence of feed tube changes on performance of log periodic dipole antenna,’’ *2012 International Conference on Microwave and Millimeter Wave Technology (ICMMT)*, pp. 1 – 4.

[35] H. Zhou, N.A. Sutton, and D.S. Filipovic. “W-band endfire log periodic dipole array,’’ *2011 IEEE International Symposium on Antennas and Propagation (APSURSI)*, pp. 1233 – 1236.

[36] J.-M. Lee, H.-J. Ham, H.-K. Ryu , J.-M. Woo, B.-J. Park, K.-S. Lee. “Miniaturization of log-periodic dipole array antenna using triangular meander structure,’’ *2012 IEEE International Conference on Wireless Information Technology and Systems (ICWITS)*, pp. 1 – 4.

[37] D.N. West and S.K. Sharma. “Frequency reconfigurable compact multiband quasi-log periodic dipole array (QLPDA) antenna for wireless communications,’’ *2010 IEEE Antennas and Propagation Society International Symposium (APSURSI)*, pp. 1 – 4.

[38] M. Hilbert, M.A. Tilston, and K.G. Balmain. “Resonance phenomena of log-periodic antennas: characteristic-mode analysis,” *IEEE Trans. Antennas Propag.*, vol. 37. pp. 1224-1234, 1989.

[39] Mesoscribe Technologies Inc. USA. online available: [http://www.mesoscribe.com/services/direct-write-fabrication/].

[40] Wireless Research Center of North Carolina (WRCNC); online available: [http://www.wirelesscenter-nc.org/].

[41] L.N. Pringle, P.H. Harms, S.P. Blalock, G.N. Kiesel, E.J. Kuster, P.G. Friederich, R.J. Prado, J.M. Morris, and G.S. Smith. “A Reconfigurable Aperture Antenna Based on Switched Links Between Electrically Small Metallic Patches,’’ *IEEE Transactions on Antennas and Propag.*, vol. 52, pp. 1434-1445, June 2004.

[42] G.H. Huff, and J.T. Bernhard. “Integration of Packaged RF MEMS Switches With Radiation Pattern Reconfigurable Square Spiral Microstrip Antennas,’’ *IEEE Transactions on Antennas and Propag.*, vol. 54, pp. 464-469, Feb 2006.

[43] M.P. Daly, and J.T. Bernhard. “Beamsteering in Pattern Reconfigurable Arrays using Directional Modulation,” *IEEE Transactions on Antennas and Propag.*, vol. 58, pp. 2259-2265, July 2010.

[44] M. Ali, A. T. M. Sayem and V. K. Kunda. “A Reconfigurable Stacked Microstrip Patch Antenna for Satellite and Terrestrial Links,’’ *IEEE Transactions on Vehicular Technology*, vol. 56, pp. 426-435, March 2007.

[45] Rodrigo, Y. Damgaci, N. Biyikli, B.A. Cetiner, J. Romeu, L. Jofre. “MEMS-Reconfigurable Antenna based on a Multi-Size Pixelled Geometry,’’ *EUCAP*, 2010.

[46] P. F. Wahid, M. A. Ali, and B. C. DeLoach, Jr.. “A reconfigurable Yagi Antenna for wireless communications,*’’ Microwave and Optical Technology Lett.*, vol. 38, No. 2, July 20 2003, pp. 140-141.

[47] D. E. Anagnostou, and A. A. Gheethan. “A Coplanar Reconfigurable Folded Slot Antenna without Bias Network for WLAN Applications,’’ *IEEE Antennas and Wireless Propag. Lett.*, vol. 8, pp. 1057-1060, 2009.

[48] Rey Febo, Design, Fabrication and Characterization of a RF MEMS Based Reconfigurable Antenna, M.S. Thesis, University of Puerto Rico, 2009.

[49] Radant MEMs, Application Note for Test and Handling of SPST RF MEMs Switches.

[50] S. Bhargava, Aperture Couple Wide-Band Microstrip Antenna Design, MTech. Thesis, CEDT, IISc. Bangalore, India, (4610-510-081-05891)